THE UNIVERSITY *of* EDINBURGH

Modelling the Psychophysics of Eye Movements in a Large Corpus of Binocular Reading Behaviours

Jun Bao

PhD.

The University of Edinburgh

2019

This thesis has been composed by myself and is my own work. The work has not been submitted for any other degree or professional qualification.

Jun Bao

Abstract

The position and shape of the pupil entrance of the eye plays a central role in video-based eye-tracking. As a result, any unexpected translation and deformation of the pupil image on camera may introduce systematic errors to eye-tracking. In this thesis we explored and corrected the spatial and temporal errors in the process of eye-tracking by means of various geometric models that involve the pupil. The main focus of this thesis is on how the properties of the pupil mediate the generation and correction of errors. There are two groups of experiments and simulations that emphasise the movement of the eyeball itself and the experiment setting, respectively. 1) For the movement of the eyeball, 1a) firstly we constructed a geometric model of the eyeball and deduced an analytical description for the eyeball, pupil, and pupil-CR trajectory during saccades and fixations. We used the model to explain the relationship between the properties of the Post Saccadic Oscillation (PSO) and other variables such as age, binocularity, saccade direction, pupil size deformation, and corneal bulge. We found that the abruptness of braking at the saccade end mediates the effects on PSO amplitude of age, binocularity, saccade size and direction. We also found that the effect of pupil-CR processing on the shape and size of PSO is big and highly dependent on the abruptness of saccade braking. 1b) Secondly, we constructed an event detection algorithm by incorporating our eye model into the Scaled Unscented Kalman filter. The algorithm can make an informed correction of the glissade artefact created by the default Eyelink event detection algorithm. Also, the algorithm is able to detect boundaries and different phases of PSO. We found that pupil size at the first peak of PSO is smaller than pupil size at the following first resting point of PSO. 2) For the experiment settings in eye-tracking, 2a) first, we used a geometric model and the differentiation among Pupil Foreshortening Error (PFE), saccadic non-PFE, and fixational non-PFE to improve the performance of pupil size correction across the page by a large margin. The performance of pupil size correction was improved by using the pupil size measured at the first resting point of PSO instead of those at the highest peak of PSO. The process of pupil size correction also produced estimates of the camera positions during eye tracking. 2b) Second, we constructed a geometric model to calculate the error in eye-tracking brought about by the movement of the head. A solution was offered to the

fixation disparity problem by analysing the effect of head movement during monocular calibration on the direction of fixation disparity, as opposed to the pupil artefact solution. 2c) Third, we used a ray traced simulation to differentiate between anatomical pupil artefact and refraction pupil artefact. The simulation results show that the size of the refraction pupil artefact is about one-third the size of the anatomical pupil artefact at a camera viewing angle of 30°. In conclusion, this thesis offers a model-based approach to explore and explain various effects and errors in eye-tracking by emphasizing the role of the pupil. This approach is ready to be generalized to other data sets and offers methods of post-hoc correction to errors in pupil size and gaze position.

Lay Summary

Eye-tracking involves recording precisely the movements of the eyes as someone views a scene or reads a screen of text. It is extensively employed in psychological research into reading, in psychophysical research on the visual system, and in many applied domains. The most widely used type of eye-tracker monitors each eye with a video camera as the viewer performs a task. A computer keeps a record of pupil position and infrared reflections from the outside of the eye (the cornea) for pupil-CR eye trackers or from the rear surface of the lens inside the eye for pupil-P4 eye trackeres. These measurements allow the computer to calculate exactly where the viewer is looking, given that the viewer has previously been *calibrated* by consciously looking at a grid of single points on the screen. Research into reading requires detailed data concerning exactly where in a word the viewer is fixating. Video-based eye-trackers have been widely available to the research community in recent decades as a single package of hardware and software that a researcher can easily learn to use to eye-track a volunteer carrying out a reading or viewing task.

However, certain inconsistencies have emerged between the data from different makes of eye-tracker and evidence has gradually accumulated concerning the complexities involved in recording the reflections from the cornea and the lens. These complexities stem from the fact that the eyes are physical systems composed of non-rigid material components that are in more or less constant motion in a task such as reading. The eyes move back and forth across the page. They stop for brief periods to fixate on the text and then move off. The structures within the eye—the iris and the lens—change shape. The iris expands and contracts in response to light levels. The lens expands and contracts to focus on the text. In addition, they are distorted by the eyes accelerating and decelerating rapidly between fixations on the text. Finally, there is substantial variation between individuals, and even between the two eyes of a single individual. All of these complexities interact. They affect the data from eye-tracking—the millisecond level record of exactly where on the screen the reader was fixating with each eye.

The research in this thesis starts with a very large volume of recorded eye-movements from representative numbers of readers of different languages, some of

which are read from left to right. The technology involved was the video-based Eyelink 2 eye-tracker. How trustworthy are the raw data? How trustworthy are the psychophysical phenomena that have been identified by researchers? Can we use mathematical models of different aspects of eye-movements to interrogate the data more closely and to begin to reveal their true meaning?

The research consists of a series of mathematical models of the best interpretation of what the psychophysical systems governing eye-movements in reading are doing, given their physical constraints. The models succeed in clarifying the data and they are made to interact so as to give the beginnings of a comprehensive understanding of the physical relations that constrain and empower the psychological processing in play in reading.

Table of Contents

Chapter 1. Literature review

All experimental paradigms in Psychology develop over time as their theoretical assumptions and implications become clearer in analysed studies. Reported behaviours come to be seen in terms of their relations with other behaviours, and their interpretation may become more and more hedged. The technologies for gathering empirical data develop, as do the statistical, mathematical and conceptual tools for understanding those data. Sometimes we revisit existing data and reinterpret them. Sometimes we abandon certain technologies, replacing them with better ones. Occasionally there are major shifts of philosophical or technological emphasis. In all these ways, Psychology and its ever diversifying subfields advances. Eye-tracking researchers find themselves in a very particular position. (For a comprehensive review, see Holmqvist, Nyström, Andersson, Dewhurst, Jarodzka and Van de Weijer, 2011.)

First, eye-tracking apparatus has a complex physical relation with the behaviours that it records. Those behaviours are at the very beginning of the visual pathways—the eyes themselves, but they also reflect the most sophisticated cognitive processing that people perform.

Second, the data are immensely rich, given that positional data can be gathered on a millisecond timescale. As in some electroneurophysiological techniques, researchers may only analyse a small fraction of the data gathered.

Third, over recent decades, small eye-tracking studies of the classic factorial type have been complemented by the gathering of large corpora of data. Such corpora can provide researchers with more representative numbers of participants and with much more data. Most natural reading happens with amounts of text that are substantially bigger than the single lines of texts that have constituted the stimulus materials of many eye-tracking experiments. Developments in regression-type statistics have allowed researchers to study the interaction of more variables in the same analysis and to obtain a more integrated picture of the cognitive processing in play. Open science has made some of these corpora accessible to the research community.

Fourth, reading is a recent cultural innovation in the emergence of human cognition. Researchers are not dealing with behaviours such as skilled reaching, face recognition or speech perception, where dedicated cognitive-neurophysiological architectures have evolved. Rather, reading is achieved by co-opting and repurposing existing cognitive-neurophysiological mechanisms. Researchers can expect to see more individual variation, the deeper they look. Radical variation is also available between orthographies such as English (very deep, phonologically), Spanish (very shallow), Arabic (right-to-left), Hebrew (regenerated from a 'language of praise'), and Chinese (pictographic).

Fifth, reading is a sophisticated cognitive process. The reader recreates the cognition of the writer concerning absent events of all kinds.

Sixth, measuring the movements of the eyes is an engineering problem. Much of the creation and marketing of eye-trackers for the study of reading has necessarily been at a distance from the psychological understanding of the processes.

Seventh, for much of the history of eye-tracking research in reading, the process has been expensive in terms of apparatus and conserving expertise, meaning that a relatively small constellation of laboratories have determined best practice.

These seven factors have conspired to put eye-tracking researchers in a special position. The research conducted has had a huge effect on our understanding of reading. Researchers have added to the basic technology a range of ingenious experimental manipulations that reflect the nature of the cognitive processing operating at any one moment. In more recent decades, researchers have 'doubled' the technology so as to be able to eye-track both the left and the right eye simultaneously, opening up new questions about binocularity in reading (Blythe,Liversedge, Joseph, White, Findlay, & Rayner, 2006, 2006; Jainta, Hoormann, Kloke, & Jaschinski, 2010; Juhasz, Liversedge, White, & Rayner, 2006; Liversedge, White, Findlay, & Rayner, 2006; Nuthmann & Kliegl, 2009; Shillcock, Roberts, Kreiner, & Obregon, 2010; Vernet & Kapoula, 2009). Many researchers have moved from the study of reading on to

‘scene’ perception (e.g., Gajewski & Henderson, 2005; Henderson & Hayes, 2018; Võ & Wolfe, 2013). This move allows researchers to involve different types of information in determining where people look when executing visual tasks in representations of the real world. The naturalism of the approach is taken even further with the use of portable eye-trackers. However, reading still represents the environment in which the viewer must negotiate very dense yet tractable information, at the level of letters, morphemes, words, phrases, sentences and discourses. Eye-tracking of reading is the interdisciplinary crossroads of Psychology, Linguistics, Psychophysics, Optometry, and Cognitive Science. At the same time it has proved to be a testbed for the development of the new regression statistics.

This thesis is concerned with a number of issues that emerge with regard to the accuracy and reliability of the data gathered in eye-tracking studies. It takes as its problem domain a large volume of eye-tracking data gathered with EyeLink-2 technology: The Edinburgh 5-Language Corpus. This corpus consists of binocular recordings of the eye-movements of native-speaker readers of English, Chinese, Spanish, Hebrew and Arabic, with additional sub-corpora of data from English-reading dyslexics and elderly readers. Participants read some 2000 words of contemporary newspaper stories written in the different languages. The analyses reported in this thesis are new analyses performed on these data, as tests of the new psychophysical models developed in the thesis. The field contains many eye-tracking studies of reading using this or similar technology. A wider goal of this thesis is to propose methods by which the interpretation of the data from such studies can be more reliably interpreted.

1.1. Eye tracking procedures

1.1.1 Different types of eye tracker

The study of reading behaviour has been dominated by the Dual Purkinje Image (DPI) eyetracker from FourwardTechnologies, which has been the gold standard for accuracy of measuring reading behaviours. Latterly, the cheaper video-based combined pupil and corneal reflection methodology used in Eyelink technology has supplemented

the use of DPI, and has been used in greater numbers (at the time of writing more than 7000 publications cite Eyelink technology). As we will see, special problems arise when the field relies on a particular technology and its algorithms (which may themselves be commercially protected) and is presented to researchers as a complete package. Other eye-tracking technologies includeelectro-oculography and the scleral contact lens/search coil; these technologies have been applied to reading far less, but still provide an important technical perspective on the Fourward and Eyelink technologies.

The Fourward DPI eyetracker relies on the fact that objects in the world are reflected back from the structures of the eye, in the form of Purkinje images. There are four such images that are typically visible, and the DPI uses the first Purkinje image (P1),the reflection from the outer surface of the cornea, and the fourth Purkinje image (P4), the inverted reflection from the inner (rearmost) surface of the lens. In DPI eye-tracking, the participant's head is immobilized using a bite-bar individual to each participant. The whole experiment necessarily takes place in a darkened room because infra-red is used to capture the reflections, meaning that the stimulus text needs to be light text on a dark background. This constraint frequently leads researchers to use green or red text to limit scatter. All of these technological constraints have psychophysical implications, which have not been immediately grasped by researchers.

1.1.2 Pupil-CR eye tracking

The data we are concerned with in this thesis were gathered using Eyelink-2 technology. It is video-based. The experimenter positions separate video cameras in front of each eye, providing the computer with a clear picture of each pupil. The cameras are attached to a headset that is securely attached to the participant's head, which is itself rested on a chinrest. Thus, a small degree of natural head movement is possible, compared with the more constrained DPI tracker. A third camera on the headset films the four infrared markers that are attached to the monitor. In this way the gaze coordinates can be transformed from a head-centered reference frame to a world-centered reference frame.

It is possible to use Eyelink technology in the full range of lighting conditions. The data with which we are concerned were gathered in normal-to-subdued room lighting indirectly supplied by a desklamp. In addition, Eyelink technology may be used in conjunction with any type of visual stimulus materials. The data with which we are concerned were dark text on a light background. Both of these contrasts with DPI technology are of psychophysical importance.

The Eyelink 2 eyetracker used to gather the current data is able to record data on the pupil size and on corneal reflection every 2 ms. The location of the centre of the pupil is assessed from the black image the pupil presents to the camera, for each eye. The corneal reflection (CR) is the reflection of a fixed infra-red light source. The centre of the pupil moves when the eyeball moves to a new position in the text. This technology essentially subtracts the change in the position of the corneal reflection from the change in the position of the centre of the pupil in order to distinguish between the effects of movement of the eyeball and slight movements of the head.

All eye-tracking participants need to be calibrated, to align the location of where the participant is intentionally fixating with the location of the technology's calculation of where the participant is looking. This is achieved by requiring the participant to fixate a grid of fixed points on the screen, as discussed below in 5.

As an illustration of the fact that the use of eye-tracking technology runs ahead of our thorough understanding of that technology, consider the report by Hooge, Holmqvist and Nyström (2016). They explored the performance an SMI Hi-Speed eye tracker, which uses the (pupil minus corneal reflection) algorithm of video-based eye trackers, as in Eyelink technology. They report differences between the pupil and the corneal reflectance signals, with regard to timing of the saccade onset, saccade peak velocity and PSO. They found higher pupil peak velocities compared with CR peak velocities. They concluded that the algorithm was exaggerating saccades based on the pupil signal and warned against using the pupil-minus-CR algorithm for studying the detailed dynamics of eye movements. Their study underlines the importance of research, such as

that presented here, which aims to model the relations between the different types of data in video-based eye tracking.

1.2. Post Saccadic Oscillation (PSO)

1.2.1. PSO properties

PSO is the wobbling of pupil and lens at the end of saccade (Nyström & Holmqvist, 2010); after temporal saccades, lens wobbling lasts for 30-100ms before it restores to 5% of its initial amplitude (Tabernero & Artal, 2014), which accounts for around 30% of the total fixation duration classified by the Eyelink algorithm. The duration of this wobbling varies greatly by individuals and direction of eye movement (adductive/abductive), as seen in our current research. Previous algorithms often split postsaccadic oscillation and classify the beginning of PSO as part of the previous saccade and the majority of PSO as part of the following fixation, or even identify the first half period of oscillation as another independent saccade if it has an amplitude big enough. The worry is that previous event detection algorithms for video-based eye-trackers produce eye movement events that do not coincide well with the cognitive processes they should support, and therefore the results of studies using these event detection algorithms should be amended.

Since the position of the eyeball (and the fovea) and the oscillation of the lens dictate how the image is projected on the retina, the image projected on the retina during PSO is blurry (see simulation by Tabernero & Artal, 2014) as opposed to the relative stationary image projection during fixation. Importantly, PSO should also be differentiated from post saccadic suppression, a 50ms break of image processing right after the saccade. Evidence suggests that postsaccadic suppression has a neural origin rather than a physical one (Burr, Morrone, & Ross, 1994; Diamond, Ross, & Morrone, 2000). Though PSO happens in the similar time period as postsaccadic suppression does, it has more variation in duration (30 – 100ms after temporal saccades) and varies dramatically by the direction of eye movement (as in our data). We should view PSO as an eye event independent of saccade and fixation.

This said, it is hard to separate PSO from the following fixation and the preceding saccade. Currently the only algorithm available to detect PSO is the All-pole model to capture PSO (Larsson, Nyström, & Stridh, 2013). This treatment is not satisfactory because the All-pole model is purely a mathematical summary of wave-like trajectories and it does not give a good explanation of how the separation of saccade, PSO, and fixation coincides with the different phases of image projection onto the retina. An ideal event detection algorithm should be able to recognize both the movement of the eyeball and the movement of the lens in order to know how the image is projected on the retina, and then use this information to decide the boundaries of the PSO and when the image on the retina is stable enough to process. For Dual Purkinje eye-trackers, whose output eye position data is calculated from P1 (corneal reflection) and P4 (posterior lens reflection), a reconstruction of movements of the eyeball and the lens should be possible; for Eyelink eye-trackers, whose output eye position data is calculated from P1 and pupil position, a reconstruction of the movements of the eyeball and the pupil can be carried out, but the oscillation of the lens can only be estimated from the oscillation of the pupil.

Research on the properties of PSO is needed for detecting it reliably. The PSO of the lens in Dual Purkinje data is partly captured by the term dynamic overshoot (the first half period of PSO), but the whole PSO is yet to be analyzed (as stated in Nyström, Hooge, & Holmqvist, 2013). Several recent studies of PSO focus on the PSO of the pupil in Eyelink data. The PSO of the pupil was first identified to be the cause of the instability of eye position after saccade in Eyelink data by Nyström, Hooge, and Holmqvist (2013); that research team went on to find that the PSO of the pupil is not entirely accounted for by the PSO of the lens (Nyström, Andersson, Magnusson, Pansell, & Hooge, 2015); they also found that the shape of PSO varies according to the length of the preceding saccade and by individuals, which causes problems for event detection algorithms (Hooge, Nyström, Cornelissen, & Holmqvist, 2015). The pupil-based Eyelink eye-tracker produces gaze position data that is inferred from P1 and pupil position; a more direct way of studying PSO is to get rid of the inference of gaze position onto the screen and study

the position of P1, P4, and pupil from videos of the eye in movement. In an insightful paper Tabernero and Artal (2014) did this by building new equipment to record eye videos during saccades. Tabernero and Artal extracted the trajectories of the center of P1 (eyeball movement trajectory), P4 (lens movement trajectory) and pupil (pupil movement trajectory), and compared these three trajectories during one saccade. The video and figures the authors produced show clearly how the trajectory of the eyeball differs qualitatively from the trajectory of the lens and the pupil (Tabernero and Artal, 2014).Tabernero and Artal fitted a damped harmonic oscillation model to the PSO of the lens and derived the damping ratio and oscillation frequency of the PSO for eight subjects. In the current study, we also simulated damped harmonic oscillation of pupil position relative to the eyeball, as a component to capture the properties of the PSO of the pupil.

To study the cognitive implications of PSO, we need to have the eyeball and lens trajectory while subjects are doing tasks (e.g., reading text, viewing scenes). Though Tabernero and Artal (2014) have a camera to record high definition eye movement videos, it is hard for them, if indeed it is possible at all, to incorporate a reading task and infer the gaze position on the text. On the other hand, the other research group (Nyström, Hooge, & Holmqvist, 2013; Hooge, Nyström, Cornelissen, & Holmqvist, 2015; Nyström, Andersson, Magnusson, Pansell, & Hooge, 2015) record the data of gaze position on the screen while subjects are carrying out tasks, but the trajectory they obtained is a composition of eyeball movement and pupil movement relative to the eyeball. Though in some PSO phase, the eyeball movement is negligible and the data can be viewed as only pupil movement relative to the eyeball, some PSO is tangled with the damping phase of the eyeball and the separation of eyeball movement and pupil movement is not trivial. Further, these researchers use point stimuli on the screen to induce point-to-point saccades of the subjects and they obtain well clustered saccade trajectory data to analyse; though it is easy to change the stimuli to text for a reading task, the data

obtained will be a mass of saccades of different lengths, direction, shape, and position on screen, which make it hard for researchers to extract a clean PSO shape and analyse it.

1.2.2 PSO and age

The age of the participant in a psychology experiment is a major variable. It is often incidentally controlled by the fact that many researchers exclusively recruit students to take part in experiments. Aging can be expected to affect eye-movements in reading, as the physical shape of the face changes (Camp, Wong, Filip, Carter, & Gupta, 2011; Friedman, 2005; Sveikata, Balciuniene, &Tutkuviene, 2011). At the level of the muscles controlling saccades and fixations, increasing facial symmetry (Linden, Kit He, Morrison, Sullivan, & Taylor, 2018) may play a role. At the level of the higher-level cognition involved in reading, we expect to see age-related decline of different types (Salthouse, 2009). We may also expect to see an interaction between these two factors (Penke et al. 2009).

Mardanbegi, Killick, Xia, Wilcockson, Gellersen, Sawyer & Crawford (2018) report eye-movement data from a pro-saccade task (participants saw targets appear to the left and the right of the initial fixation point at the middle of the screen) and from a number of visual search tasks (participants watched short videos). They compared older and younger participants and reported significantly larger post-saccadic oscillations in the older group, which they attributed to changes in the muscle strength with aging.

1.2.3. PSO, pupil-CR eye tracking and simulation

Robinson (1964) provides an early, rigorous analysis of the mechanics of saccades, based on work by Westheimer (1954), Yarbus (1956) and Mackensen (1958), who each used different technologies. Robinson used a scleral search coil in a magnetic field, together with the subject wearing a suction scleral contact lens that allowed known forces to be applied to the eyeball. His conclusion was that the eyeball makes quick saccadic movements by means of a large, briefly applied, excess force delivered by the extraocular muscles: “For example, in maintaining the eye 10 degrees horizontally from the primary position the horizontal recti need apply a net force of only 15 g but during the

saccade to reach that position they apply about 43 g during the first 40 msec of movement" (p. 245). In addition, he states "The mechanical events in the muscles and orbital tissues are not complete until about 250 msec after the completion of the saccade." (p. 264). Finally, from Robinson's study we take the key role of the lateral rectus muscle and the fact that the complex left-right activity of the eye can begin to be understood in terms of a precisely stated mechanical model.

Robinson, O'meara, Scott & Collins (1969) followed up this work by experimenting on the detached lateral rectus muscle in three strabismus patients. They extended their previous conclusions with quantitative data again stressing the crucial role of the lateral rectus muscle, its "pulsatile nature", the viscoelasticity of the fibres involved, and the non-immediacy of the recovery of the muscle after the saccade. The detailed investigation of the anatomy suggests the main elements of a successful implemented model of saccade generation.

As well as the information gained from studies of the lateral rectus muscle itself, we may assume that there are general principles that apply across different anatomical situations in which muscles act antagonistically. Suzuki, Shiller, Gribble, andOstry (2001) test the hypothesis that the coactivation of such muscles varies with movement speed; i.e. coactivation and movement control are related. They measured muscle coactivation after movement, looking at single-joint shoulder and single-joint elbow movements. They showed that muscle coactivation varies with movement velocity and that co-contraction of muscles is related in a simple way to phasic muscle activity. These simple principles may be applied to the case of eye-movement control.

Calculating the location and dimensions of the pupil is central to video-based eye-tracking methodology, as used in Eyelink eye-trackers. But the pupil is inner iris border, being simply the aperture defined by the iris, and has been shown to 'move' within the iris as a result of deformations of the iris, particularly at the end of the saccade (Hooge, Holmqvist & Nyström, 2016; Hooge, Nyström, Cornelissen & Holmqvist, 2015; Kimmel, Mammo & Newsome, 2012; Nyström, Hooge & Holmqvist,2013). Bouzat, Freije,

Frapiccini and Gasaneo (2018) show that this movement may be the result of inertia in the iris during the rotation of the eyeball. They describe a Newtonian model that correctly predicts the dependence of the amplitude and period of the post-saccadic oscillations of the pupil on saccade size. Del Punta, Rodriguez, Gasaneo and Bouzat (2019) extend this modelling of PSO, varying parameters such as elasticity of the iris, global eyeball velocity, and saccade size.

In summary, research such as that discussed above demonstrates the centrality of the lateral rectus muscle in orienting the eyes horizontally, and provides a foundation for modelling the PSO. It should be noted that the research to date has not been on the reading of extensive text, but on tasks chosen to be simpler or more representative of normal vision. Reading of text typically involves the great majority of saccades being in the same consecutive direction, with the potential involvement of higher cognition, and with the additional issue (see below) of fixation disparity (the distance between the simultaneous fixation points of the two eyes) having real processing consequences. PSO has consequences for when the take-up of visual information can begin after a saccade. PSO in reading deserves special attention.

1.3. Event detection algorithms

The increasingly widespread use of eye-trackers that can record events on a millsecond basis has raised the issue of how to detect the events associated with visual inspection. Qualitatively defined events such as ‘fixation’ and ‘saccade’ have given way to the question of the transition between such events and to their internal content. Hooge, Niehorster, Nyström, Andersson and Hessels (2018) underline this issue by studying the agreement between human classifiers of eye-movement events. They find excellent agreement at the level at which small events are consolidated into larger events. The differences between judges was in how the judges assigned the ends of fixations and the status of independent fixations. They conclude that even experienced human judges are not the ‘gold standard’ against which automated algorithms should be judged. It should be noted that a large proportion of the psychological experiments in which eye-tracking is

used do not require closely motivated definitions of fixations, so long as the same criteria are applied across different conditions in the experiment. In addition, the small size of the datasets from traditional factorial experiments has typically allowed human judges to 'clean up' the data manually and assign events in the same way.

Detailed studies of saccades and fixations have revealed complex internal activity in each, with different types of movement having different processing implications. For instance, supposedly static fixations contain drift, microsaccades, and ocular microtremor (see, e.g., Ryle, Vohnsen & Sheridan, 2015). When exactly does a fixation start and end? What are the criteria? Can we understand more about how one event transitions into a qualitatively different type of event? Can we obtain insights into how these changes affect visual perception? These research questions are necessarily ahead of the understanding of eye movements that have underwritten the development of the technology itself. They raise the issue of the algorithms that are indigenous to the commercial technology such Eyelink eye-trackers. Are such algorithms in need of revision? What assumptions are implicitly being made by researchers who use commercial eye-trackers as a package and accept the definitions of the events on face value? Indeed, is it possible to return to the data gathered by such eye-trackers and reinterpret them in the light of new understanding of the definition of eye-movement events? This is the key question at the heart of this thesis.

Nyström and Holmqvist (2010) present a velocity-based algorithm that led them to recognize *glissades*, a 24 ms (mean)back-and-forth wobble they observed at the end of some 50% of saccades, as a separate category of eye movements. They argued that their algorithm made event detection less sensitive to variations in noise level and they demonstrated its robustness in detecting fixations, saccades, and glissades in eye-movement data from reading and scene perception. Nyström and Holmqvist argue that researchers have the choice as to whether to assign glissades to fixations or to saccades, but this is perhaps to miss the point that the categorization of eye-movement

events is best carried out from the perspective of what they mean for higher, cognitive processing.

Andersson, Larsson, Holmqvist, Stridh and Nyström (2017) compared the output of ten different eye-movement event detection algorithms with manual judgments from two human experts. The authors report fair agreement on data from static stimuli, but very poor agreement when the data were from dynamic stimuli. The main variation was in terms of the durations assigned to fixations, saccades, and post-saccadic oscillations. Their study underlines the fact that eye-movement events vary over participants, over tasks, and over the technologies used to gather the data. This means that the most insightful way to understand and to categorize eye-movement events is to model their *generation* from the essential elements of the domain. Fuhl, Santini, Kuebler, Castner, Rosenstiel and Kasneci (2018) illustrate this approach of simulating the eye-movement data and using machine learning techniques to create detectors for events.

1.4. Pupil size correction

Viewing a disc from an increasingly oblique angle progressively reduces its apparent area; it becomes more and more elliptical, through foreshortening. This process applies to the camera's view of the pupil, in a video-based eye-tracker. Hayes and Petrov (2001) refer to this as the pupil foreshortening error (PFE).

Video-based eye-trackers record the dimensions of the pupil during viewing and use the position of the pupil centre (usually relative to the corneal reflection) to infer the fixation point. In the Eyelink 2 eye-tracker, the cameras fitted individually in front of each eye are liable to give a *foreshortened* image of the pupil when the eyeball rotates to the right or left. Such foreshortening means that the pixel mass of the pupil is reduced and leads to systematic error in the fixation location data. Hayes and Petrov (2016) illustrate ways to model this error geometrically, partly using artificial eyes. Gagl, Hawelka and Hutzler (2011) similarly model this error, specifically for a reading task. Brisson, Mainville, Mailloux, Beaulieu, Serres and Sirois (2013) compared three different eye-tracking

technologies in a task requiring object pursuit. All three systems yielded systematic errors.

The problem of foreshortening can be appreciated from a purely geometrical perspective, but this is to assume that the thickness of the iris is zero and that the passage of light through the iris happens all in one plane. This is not the case. Mathur,Gehrmann and Atchison (2013) show that there is a complex process of refraction taking place as the angle through the eyeball increases away from the optic axis of the eyeball in either direction. The shape of the pupil does not simply become predictably more elliptical. The thickness of the cornea and of the iris have to be taken into account.

In summary, the shape of the pupil and the location of the pupil centre are not simple issues. There is scope for considerable error.

1.5. The fixation disparity problem

When we read, we use both eyes to fixate on the text. The disparity between the fixation positions of two eyes is referred to as fixation disparity (FD). FD is characterized as aligned, uncrossed, or crossed (Liversedge, White, Findlay, & Rayner, 2006). In their terms, binocular fixations are uncrossed when the left eye fixation is more than one character away to the left of the right eye fixation, and crossed when the left eye fixation is more than one character away to the right of the right eye fixation. They found that the average disparity was 1.1 characters.

There is a critical debate about the direction of fixation disparity and within-fixation movement in the eye tracking literature concerning reading. Studies using the DPI eye tracker report the majority of unaligned fixations to be uncrossed (Blythe,Liversedge, Joseph, White, Findlay, & Rayner, 2006, 2006; Juhasz, Liversedge, White, & Rayner, 2006; Liversedge et al., 2006). In these studies, the two eyes typically converge within fixation so that disparity reduces during the fixation period (see, also, Hendriks, 1996). The DPI eye-tracker uses reflection points on the lens instead of the pupil image for the calculation of relative eye movement.

On the other hand, most studies using pupil-based eye-trackers report the majority of unaligned fixations to be crossed (Jainta, Hoormann, Kloke, & Jaschinski, 2010; Vernet & Kapoula, 2009; Nuthmann & Kliegl, 2009; Shillcock, Roberts, Kreiner, & Obregon, 2010). In these studies, the two eyes typically diverge within fixation so that, again, disparity reduces during the fixation period.

There have been a number of attempts to find the reason for the discrepancy in the direction of fixation disparity in the literature (Huckauf, 2018; Kirkby, Blythe, Drieghe, Benson, & Liversedge, 2013; Köpsel & Huckauf, 2017). Kirkby et al. (2013) tested whether the discrepancy is caused by the use of different types of eye trackers. They conducted reading experiments using both DPI and pupil-based eye trackers (Eyelink 1000) and found a majority of uncrossed fixation disparity among unaligned fixations for both types of eye trackers. Due to experiment setting limitations for the DPI eye tracker, their experiments were conducted in a dark room and with low luminance stimuli (white text and black background) for both eye tracker types. For experiments using the DPI, their results of uncrossed fixation disparity coincided with previous studies; for experiments using pupil-based eye trackers, the results created a contrast: uncrossed disparities tended to be found for experiments in dark room using low luminance stimuli whereas crossed disparities tended to be found for experiments in normal-lit room using high luminance stimuli.

To investigate the effect of luminance change on fixation disparity, Köpsel and Huckauf (2017) used a pupil-based eye tracker to measure fixation disparity when participants read texts on dark or bright background, both after calibration on grey background. The results showed uncrossed disparities for medium-to-dark (calibration luminance to reading text luminance) setting and crossed disparities for medium-to-bright setting. In a further study using pupil-based eye tracker, Huckauf (2018) obtained uncrossed disparities for bright-to-dark setting, crossed disparities for dark-to-bright setting, and aligned fixations for both dark-to-dark and bright-to-bright settings. For pupil-based eye trackers, such shifts of fixation disparity direction caused by luminance

change can be real vergence movement coupled with accommodation and pupil size change, or they can be artifacts caused by shifts of pupil center when pupil size changes (Huckauf, 2018). Hooge, Hessels, and Nyström (2019) answered this question by recording both binocular fixation position and corneal reflection when participants fixated a target with luminance change. They found that recorded fixation disparity changes with luminance change but corneal reflection does not, which suggests that there is no eyeball rotation during luminance change and the changes in fixation disparity are only artefacts accompanied by pupil size change. In the full range of pupil size, the magnitude of this artefact varies from near zero to 5°across participants and the binocular difference of this artefact magnitude varies from near zero to 3° across participants (Drewes, Zhu, Hu, & Hu, 2014; Hooge, Hessels, & Nyström, 2019). Given the constant change of pupil size during reading experiments, the magnitude and idiosyncrasy of this pupil-size dependent artefact questions the integrity of eye tracking researches using pupil-based eye trackers, especially when fixation disparity is the research target.

A further complication has been that, prior to the emergence of fixation disparity as a topic in the eye-tracking of normal reading behaviours, researchers adopted *binocular calibration* as the most effective means of calibrating a participant in eye-tracking experiments: the participant responded to the calibration screen (e.g. a grid of nine dots in the indigenous Eyelinksoftware) with both eyes open and obeyed the instruction to simply fixate on the different locations in turn in the normal way. This procedure had the effect of zeroing any real pre-existing fixation disparity and/or arbitrarily prioritizing one or other eye. Furthermore, reading researchers typically allowed participants to read relatively naturalistically with both eyes open, but only recorded the movements of the right eye, or only used data from that eye, assuming that the left eye's information was simply a duplication of the right eye.

So what explains the crossed fixation disparities in reading data using pupil-based eye trackers? The pupil artefact explanation is that that all research groups using pupil-based eye trackers (Jainta, Hoormann, Kloke, & Jaschinski, 2010;Nuthmann &

Kliegl, 2009; Shillcock, Roberts, Kreiner, & Obregon, 2010; Vernet & Kapoula, 2009) somehow calibrated participants with low luminance and bigger pupil size and then let participants read with high luminance and smaller pupil size. This decrease of pupil size results in a pupil-size dependent artefact that generates crossed fixation disparities, while the real fixation positions remain aligned between the two eyes. We think this is not probable. In Chapter 4, we will introduce a head movement explanation to the crossed fixation disparities.

1.6. Pupil artefact

The pupil artefact is the fixation position error induced by pupil size change. As pupil size changes, the centre of the pupil changes, resulting in a change in recorded gaze fixation position while the actual gaze fixation position stays still.

For instance, Drewes, Zhu, Hu and Hu (2014) report binocular pupil-size dependent pupil drift measurements from 39 subjects, varying both between subjects (mean 2.6 deg) and between the eyes of individual subjects (mean 1.0 deg). Drift direction was mostly downward and nasal. They discuss methods that researchers might use to compensate for the pupil-based shift.

Hooge, Hessels and Nystrom (2019) quantify the fixation error in terms of degrees per mm of pupil size change at−0.40°/mm vergence change (i.e. −0.20°/mm for one eye) for the EyeLink 1000 plus, and −0.72°/mm vergence change (i.e. one eye is −0.36°/mm) for the SMI iView X hi-speed 1250.

Jaschinski (2016) measures the vergence change at -27 min arc/mm, or about 0.05mm/1mm pupil change for EyeLink II. Other researchers have used a variety of methodological and technological approaches and have arrived at a mean shift in the reported centre of the pupil of about 0.05 mm per 1 mm change in pupil size, but individuals differ (see Choe, Blake, Lee, 2014;Wilson, Campbell, Simonet, 1988, Wyatt, 2010; Yang, Thompson, & Burns, 2002).

In summary, the pupil artefact is an established qualitative phenomenon with considerable agreement on its quantitative aspects.

1.7. Methodology

1.7.1. Modelling

Computationally implemented cognitive modelling is arguably the key paradigm in Cognitive Science (McClelland, 2009). Researchers have identified several advantages of computational modelling. First, a computationally implemented model of some aspect of cognition is able to rigorously test a theory, revealing an y flaws not noticed by the researcher. Second, the ability of computers to operate over very large numbers of entities and to perform very large numbers of calculations very quickly takes the theorizing beyond what has previously been possible and reveals new concepts in process and representation. Third, computational modelling can contribute to the metatheoretical and philosophical understanding of cognition, suggesting new perspectives on topics such as innateness, learning, development, emergence and inference (e.g.Clark, 1991; Dennett, 1995; Elman, Bates and Johnson, 1998). Fourth, the results of an implemented model may interact with laboratory research in a virtuous spiral, each challenging the other to capture further behaviours. Part of this interaction is that the model allows quantitative predictions to be made about the real world.

However, although prediction is a proper part of empirical research, the most important role of a computational model is as a potential *explanation* of particular behaviours. For McClelland, the fact that the behavioural domain is *simplified* in the model is the central contribution to explanation. Modellers seek to reduce the number of parameters in a model and the number of different entities, adhering to Ockham's Razor. If the model produces behaviours analogous to those seen in the real-world domain of cognition, then it allows the latter domain to be understood to a greater extent than previously.

Nothing can be modelled without abstraction having taken place. We cannot manipulate or test the real world withoutidentifying certain aspects of that world and placing other aspects of that world in the background. The models we will explore below are the result of abstracting away from the higher cognition involved in reading (the

source of the data). The models involve some of the structures associated with the eye, such as the eyeball, lens, cornea, iris and the lateral and medial rectus muscles, and some of the properties associated with those structures, such as elasticity, angle of incidence, and physical size.Their interaction is modelled by parameterizing the relations between these structures and allowing them to interact. Successful modelling means graphs of model behaviour that qualitatively resemble the graphs of real behaviours. They are anapproximation in the direction of understanding the psychophysics of eye-movements.

Some of these relations may be treated analytically as purely mathematical relations, in the way that Steven's Law (cf.Krueger, 1989) approximates the subjective matching of perceptual continua to target intensities. Mathematical relations in modelling are important generalizations, but even the very simple Steven's Law only approximates behaviours across participants and across dimensions.

The alternative approach to explaining behaviour in a domain is to identify a material entity within the domain that 'speaks to' every other entity in the domain and itself embodies the characteristic activity of the domain (Shillcock, *in press*). Such an entity can be a complex thing itself, as opposed to being some simple element. In the modelling presented below, the lateral rectus muscle presents itself as the entity that has a central role in orienting to the outside world, affecting the status of every other entity in the domain. The implication is that the proper domain of study is everything that is affected by the lateral rectus muscle, itself a proxy for the more basic orienting response.

1.7.2. Kalman filter

The data we are dealing with consist of measurements of gaze positions across time. They are inherently noisy. They are intimately related to each other, but are mediated in ways that we do not yet fully understand. One way of approaching such data has been by means of a Kalman Filter (see, e.g. Komogortsev & Khan, 2008; Maybeck, 1982). The Kalman filter has been enormously influential in the modelling of biological and artificial motion (see, e.g. Wolpert & Ghahramani, 2000). The filter operates optimally to take

account of all the available information, as well as prior knowledge about the system and any measuring devices, so as to make predictions about future states of the system. It also operates recursively, so that it does not need access to all of the past data. Below we use this information processing approach to predict psychophysical quantities in eye-movement behaviours. Developments of the basic Kalman Filter have included the Unscented Kalman Filter (Julier, 2002; Valverde & Terzija, 2011; Wan & Van Der Merwe, 2000), which was developed to cope with highly nonlinear models.

Chapter 2. Experiment Procedure and Data Manipulation

This chapter describes how eye movement data were collected and processed for further analysis in the following chapters. The chapter consists of 5 sections: Section 2.1 describes from raw eye the experiment procedure of recording eye movements; Section 2.2 describes the conversion tracker output to Python DataFrame for each trial and calibration; Section 2.3 describes the event detection process; Section 2.4 describes the collection of saccade-to-fixation trajectories; Section 2.5 describes the clustering of saccade-to-fixation trajectories that enables the calculation of mean saccade-to-fixation trajectories for certain saccade length.

The data flow of this thesis is as follows: after running experiments (Section 2.1), from the eye tracker output files we extracted calibration information and streams of binocular eye positions in pixels on the screen and pupil size for every 2ms (Section 2.2); these raw trajectory data were processed by an adaptive event detection algorithm following Nyström and Holmqvist (2010); then raw trajectories were sliced into saccade-to-fixation trajectories based on event detection results (Section 2.3); saccade-to-fixation were further processed to produce mean saccade-to-fixation trajectories (Section 2.4). Mean saccade-to-fixation trajectories will be used in Chapter 4 for the modelling of PSO. The raw trajectory data, together with fitted parameters of the post-saccadic model in Chapter 3.2, will be used to create a new event detection algorithm based on a Kalman filter in Chapter 3.3. The detected eye events (fixations, saccades, PSOs, blinks) will be used in Chapter 4.1 for pupil size correction across the screen, in Chapter 4.2 for fixation disparity correction, and in Chapter 4.3 for pupil artefact estimation.

2.1 Experiment Procedure

Only the experiment settings of English and Chinese passage reading data are provided here[3]. The binocular eye movements of 25 Arabic, 46 Chinese, 45 English, 15 Hebrew, and 31 Spanish native speakers reading their respective native language were recorded. The text consists of 21 newspaper stories for each language. Stories were

presented by pages with each page consisting of up to 5 lines. The stories added up to about 500 lines and about 5000 words.

An SR Research EyeLink II head-mounted eyetracker was used to record eye movements. The eyetracker uses the relative position of corneal reflection (P1) and pupil position to infer gaze position on screen. A chin rest was used to limit the head movement of subjects. The display screen was a 22" Iiyama VisionMaster Pro 514 display (1024 x 768 pixels). Text was presented in black and background in white. The font used for English characters was 24 pt monospaced Monaco font. Each line had a maximum of 64 English characters with the width of an English letter averaged at 14.4 pixels (the visual angle subtended 0.33 degrees at the centre of the screen at 75cm distance). The average character widths of other languages are similar to that of English except each Chinese character had a width of 28 pixels (0.64 degrees).

Eyes were calibrated independently (one eye was calibrated with the other eye covered by a black eye patch). Subjects first read a two-page instruction on screen, then a four-page practice story before they read the experiment stories. At the beginning of each page before text was displayed, a black rectangle with the width of 23 pixels (0.53 degrees) showed at the left end of the first line; subjects had to fixate at this black rectangle to trigger the display of text. Having read the text in the page, subjects needed to fixate an 11 by 19 pixels (0.25 by 0.44 degrees) black rectangle near the bottom right corner of the screen, then they pressed a button to continue to the next page. After reading each story, subjects needed to answer a yes-or-no comprehension question on screen. Before the start of the next story, subjects needed to fixate at each point in a nine-point grid for the experimenter to check if recalibration was needed. The reading was divided into three blocks and lasted about 90 minutes in total.

2.2 Extract Data from Eyetracker output

2.2.1 EDF file to ASC file

A Windows version of EDF2ACS was used to convert the EDF files produced by EyeLink II to ASC files. In the conversion settings, select 'output samples and events' for

‘Sample/Events’; select ‘output binocular data’ for ‘binocular recording’; tick ‘output resolution data’, ‘output velocity data’, and ‘output input values’; do not tick ‘output float time’; select ‘Gaze’ for ‘eye position type’. Each EDF file contains the data of one block for one subject. The name of an EDF file consists of subject number, block number, and language label. For example, file ‘SUB09B1E’ is the data for subject 9, block 1 in English dataset. For some sessions data for one block was split in two and the resulting file names have ‘(part1)’ and ‘(part2)’ appended at the end (e.g., ‘SUB43B1C(par1)’); after being converted to ASC file, these parts were merged by pasting texts in one file into the other one. The files with names that do not comply to these naming conventions were deleted (very rare).

Here is a summary of the EDF files in our corpus. The Arabic dataset has 29 subjects (SUB01 - SUB29). The data of block 3 is missing for subject 28; both block 2 and block 3 are missing for subjects 8, 10, 21, 23, 24, 27, 29. The Chinese dataset has 47 subjects (SUB01 – SUB50 with 13, 47, 49 missing). Block 3 is missing for subject 10; both block 2 and block 3 are missing for subjects 8, 23, 25, 33, 26, 40, 44, 48, 50). The English dataset has 47 subjects (SUB01 – SUB44 and SUB80, 81, 91). Block 1 for subjects 31, 80, 81 is missing; block 3 for subject 21 is missing; both block 2 and block 3 for subjects 31, 36, 40, and 91 are missing. The Hebrew dataset has 16 subjects (SUB01 – SUB16). Block 3 for subjects 10, 11 is missing; both block 2 and block 3 are missing for subject 16. The Spanish dataset has 33 subjects (SUB01 – SUB34 with SUB14 having no data available). Block 3 is missing for subject 31; both block 2 and block 3 are missing for subjects 14 and 34. The English Dyslexia dataset has 6 subjects (SUB80 – SUB85). Block 3 is missing for subject 84; both block 2 and block 3 are missing for subjects 80 and 81. The EDF file ‘SUB43B2C’, ‘SUB12B1H’, ‘SUB12B2H’ and ‘SUB14B1S’ cannot be converted to asc file for some unknown reason so they are not available for later analysis; these EDF files cannot be opened directly in Eyelink data viewer, but can be opened in failsafe mode. About half of the English EDF files only have eye events without sampling points (SUB01 ~ SUB17) due to experimenter error; these files cannot be

further analyzed.

2.2.2 ASC file to DataFrame of Trials and Calibrations

For each language, gaze position data from all ASC files were arranged into one Python DataFrame (in library *pandas*). Each row in the DataFrame contains information for one sample point of gaze position for left and right eye, pupil size, and many other types of information at this time point. The main algorithm is shown in Figure 1. One challenge is to make every sample point indexable: for example, researchers should be able to easily select all the sample points of subject 17, block 1, the 5th trial. One way to do this is to use the hierarchical indexing of *pandas* DataFrame, however, introducing hierarchical indexing will create obstacles for the transfer between DataFrame in Python and DataFrame in other programming languages such as R. In our research we used a string ID that contains all the registration information for each sample point. The ID is of the form ‘filename.trialCount.trialID’ (e.g., ‘SUB18B1E.1.0-1PAGE1’) and researchers need to parse the ID string for information. Another challenge is to handle the peculiarities in file reading. Due to manual interruptions during eye tracking and sometimes recording errors by the machine itself, the resulting ASC files have unexpected lines that are not explained in the Eyelink User Manual. One last caution, this algorithm only read binocular EDF with the sample lines of the format {'time', 'x_l', 'y_l', 'pupilSize_l', 'x_r', 'y_r', 'pupilSize_r', 'x_velocity_l', 'y_velocity_l', 'x_velocity_r', 'y_velocity_r', 'x_resolution', 'y_resolution', 'unknown1', 'unknown2'}. The algorithm can be modified to read binocular EDF of another format or monocular EDF by changing the columns of DataFrame accordingly.

Algorithm: getSampleDfFromAsc

Input: A set of all the lines in one ASC file. AscLines = {line1, line2, line3…}
Output: a Dataframe of sample points

Algorithm:
# 1. get indices of trial start and end
Starts = {indices of line in AscLines that contains 'TRIALID'}
Ends = {indices of line in AscLines that contains 'TRIAL_RESULT'}

# 2. prune errant items in Starts to make sure items in Starts and Ends are one-to-one paired
# (assumes there is no errant items in Ends)
Starts = { the latest start index in Starts for each end index in Ends}

3. Extract sample points trial by trial
Collect and concatenate all the Samples in the loop below:
for each pair of index (S, E) in Starts and Ends:
Skip this trial if the start line of this trial is empty (this happens for some unknown reason)
TrialLines = {lines in AscLines between index S and E}
TrialTokenLists = {for each line in TrialLines, separate it into a list of token by white space}
Samples = {all the lists of token in TrialTokenLists that has a digit as its first token}
add two items add the head of each list in Samples:
1. A composed ID for this trial of the form: filename.trialCount.trialID
2. A flag to indicate whether this sample is recorded before or after the text is displayed on the screen.
Convert the concatenated Samples to SamplesDataframe by adding column names:
{'oneID', 'displayOn', 'time', 'x_l', 'y_l', 'pupilSize_l', 'x_r', 'y_r', 'pupilSize_r', 'x_velocity_l', 'y_velocity_l', 'x_velocity_r', 'y_velocity_r', 'x_resolution', 'y_resolution', 'unknown1', 'unknown2'}

return SamplesDataframe

Fig. 1. The algorithm to extract sample point DataFrame from ASC files.

For each pair of left and right eye calibrations, we can identify which trials were run under this calibration pair. Later in Chapter 4.2, it is necessary that the models be fitted to trials grouped by calibration pairs. In Chapter 4.1, pupil size across the screen will be corrected by a geometric model of eyeball, camera, and screen positions. If the model were to be fitted to fixations of each trial (each page), there would be an overfitting problem because too many parameters (4 to 8 parameters depending on the types of model) would be estimated from few samples (20 – 40 fixations per trial). If the model were to be fitted to the fixations of each subject, the results would not respect the fact,

while participants are instructed to keep their head steady after each calibration, the relative positions of eyeball, camera, and screen positions are likely to change between calibrations. In Chapter 4.2, fixation disparity will be corrected by a head movement model that incorporates calibration procedure, so calibration information has to be extracted for this modelling. The algorithm to extract calibration information for ASC file is shown in Figure 2.

Algorithm: getCalibrationDfFrom Asc

Input: A set of all the lines in one ASC file. AscLines = {line1, line2, line3…}
Output: a Dataframe of calibration data
Algorithm:
# 1. get indices of trial start and end for each eye
LeftCalStarts = {indices of line in AscLines that contains 'FOR LEFT'}
LeftCalEnds = {indices of line in AscLines that contains '!CAL VALIDATION HV9 L LEFT'}
RightCalStarts = {indices of line in AscLines that contains 'FOR RIGHT'}
RightCalEnds = {indices of line in AscLines that contains '!CAL VALIDATION HV9 R RIGHT'}

# 2.1 prune errant items in Starts to make sure items in Starts and Ends are one-to-one paired
LeftCalStarts = {the latest start index in LeftCalStarts for each end index in LeftCalEnds}
same for RightCalStarts
2.2 prune duplicate items
    Separately for left and right eye calibration, find the start and end index pairs that share the same start index, keep only the pair with the latest start.

3. Extract information for each calibration
Collect and concatenate all the CalInfo in the loop below:
for each pair of index (S, E) in Left(Right)CalStarts and Left(Right)CalEnds:
    CalLines = {lines in AscLines between index S and E}
    CalInfo = {examine each line of CalLines for calibration information (95 items in total)}
    Convert the concatenated CalInfo to CalibrationDf by adding column names listed
return CalibrationDf

Fig. 2. The algorithm to extract calibration DataFrame from ASC files.

2.3 event detection and saccade-to-fixation composites

This section identifies all saccade-to-fixation composites from the sample points

Dataframe. Since we do not have a satisfactory algorithm to identify the boundaries of PSO, we cannot separate saccade and fixation with confidence. For the data flow of each trial, it turns out the only type of cutting point we can make with certain confidence is the onset of saccade (or the offset of fixation). These cut points group the sample points into a set of saccade-to-fixation composites. The collection of saccade-to-fixation composites provides data for studying the transition from saccade to fixation, where oscillation of the pupil happens. Section 2.3.1 describes the application of an adaptive event detection algorithm (Nyström & Holmqvist, 2010) that marks saccade onset, tentative saccade offset, and blinks; Section 2.3.2 describes the process of extracting saccade-to-fixation composites based on these initial event detection outputs.

2.3.1 detect saccade onset, tentative saccade offset, and blinks

At this stage, though we only need to identify the saccade onset, identifying a tentative saccade offset in tandem with saccade onset helps to rule out false saccade onsets and makes the cutting more reliable. Following Nyström and Holmqvist (2010), we used their adaptive algorithm for identifying saccade onset and offset. This is a velocity-based event detection algorithm that adapts its threshold of saccade peak velocity, saccade offset velocity to the overall velocity noise in data, and adapts its threshold of saccade onset velocity to the local noise preceding that onset and the overall noise. We replicated their algorithm in Python and modified it to detect both forward saccades and backward saccades. Also we used this adaptive algorithm for backward saccades to detect blinks (a dip in pupil size) by applying it on the derivative of pupil size across time. This algorithm is shown in Figure 3.

Algorithm: markBlinkAndRawSaccade

Input: sampleDf (a Dataframe of samples), initial threshold of saccade peak (initialSaccadePeakThreshold) and blink valley (initialBlinkValleyThreshold),
Output: new samplesDf with mark columns added

Algorithm:
For each trial in sampleDf:

1. calculate velocity (pixels per millisecond)
Derive the velocity by pixel (column 'x_pixelVelocity_l'): the difference of x location between two adjacent sample points divided by time resolution (2 millisecond).

2. mark saccade peak and valley using adaptive threshold (Nyström & Holmqvist, 2010)
2.1 initiation
Add to trialDf a mark column to mark saccade events (column 'saccade_l', initiated to 'no'), and a count column to number each saccade in order to distinct saccades from each other (column 'saccade_l_count', intiated to 'no').
Set saccadePeakThreshold to initialSaccadePeakThreshold and saccadeValleyThreshold to the negative of initialSaccadePeakThreshold.
2.2 mark iteratively
If a sample point's pixel velocity is above saccadePeakThreshold, mark it as 'peak'; if it is below saccadeValleyThreshold, mark it as 'valley'.
Calculate the mean and standard deviation of the pixel velocity of the rest sample points, update saccadePeakThreshold and saccadeValleyThreshold:
saccadePeakThreshold = restMean + 6 * restStd
saccadeValleyThreshold = restMean - 6 * restStd
mark peak and valley again using the updated thresholds, then calculate new thresholds; keep iterating until the updated value of saccadePeakThreshold is within 1 pixel smaller than the previous value

# 3. mark saccade onset and offset
# 3.1 initiation
saccadePeakOnsetThreshold = restMean + 3 * restStd
saccadeValleyOnsetThreshold = restMean – 3 * restStd
# 3.2 mark onset
for each marked saccade peak (a segment of sample points), walk leftwards from the left end of peak sample points till the first local minimum below saccadePeakOnsetThreshold is reached, mark this point as 'peakOnset' and the path walked as 'peakLeftSide' and proliferate the saccade count of peak sample points to the newly marked sample points. Do the same for saccade valleys.

3.3 mark offset
Set saccadePeakOffsetThreshold and saccadeValleyOffsetThreshold to be the same as their onset compartments. Mark ‘peakOffset’ and ‘peakRightSide’, and proliferate the saccade count of peak
sample points to the newly marked sample points.
Do the same for saccade valleys.
Note: In the paper by Nyström & Holmqvist (2010), the offset threshold is calculate from onset threshold and a factor that captures the noise level of pixel velocity within a 40 ms window before onset threshold. Because this treatment is ignorant of post saccade oscillation which they corrected in later paper (Larsson, Nyström, & Stridh, 2013), it should be just as bad to use onset threshold as offset threshold. Thought in the actual algorithm we use the Nyström and Holmqvist’s (2010) treatment of offset thresholds, here we skip explaining it for simplicity.

4. mark blinks
Similar procedure to marking saccade valleys except it operates on pupil size instead of pixel velocity. The correspond mark column and count columns is named as ‘blink_l’ and ‘blink_l_count’.

return sampleDf

Fig. 3. The algorithm to mark blinks and tentative saccade onset and offset

One issue needs to be addressed before the discussion of the result of saccade detection: the calculation of velocity. The Eyelink eyetracker provides velocity data along with gaze position data, but this velocity data measures degree per second and the gaze position data measures pixel coordinates on screen. In our analysis, we should translate their measurement into both in pixels or both in visual angle, otherwise the result of the analysis will be hard to explain; considering the later convenience for registering gaze position onto the text, we choose to use pixels on screen as the measurement of both gaze position and velocity. There are two ways to obtain the velocity measured in pixels per second. The first way, the one we used in this research, is to take the first derivative of gaze position by time and divide it by 2ms. Also, importantly, after dividing by 2, the difference between two time points with an interval of 2ms should be assigned as the velocity at the averaged time point of the two time points. I made an approximation by assigning this velocity to the time point on the right, resulting in a 1ms shift of pixel velocity to the right. Since the later analysis of saccade-to-fixation composite locked the

time to the onset of saccade, this shift did not affect later analysis, but this approximation should be revisited in future research. The second way is to take the velocity data (degree per second) offered by the Eyelink eyetracker and multiply it by the instant gaze resolution data (pixel per degree) in order to obtain pixel velocity (pixels per second). The difference between the pixel velocity obtained in these two ways is showed in Figure 4, with the time shift approximation in the first way corrected. In Figure 4, it seems that the visual angle velocity data produced by Eyelink II is the derivative of gaze position adjusted by gaze resolution and then applied by a low-pass filter. The exact calculation process and which filter is used is unknown. Because the filter used in the second way of calculating pixel velocity is unknown, we should not choose this method. In hindsight, we should have filtered the pixel velocity calculated in the first way (i.e., from gaze position) in order to obtain more reliable detection of saccades, but we did not apply any filter in this dissertation. Again, this mistake did not affect the later analysis of saccade-to-fixation composite because the possible unsatisfactory detection of saccade onset was entirely amended by a later algorithm (shiftTime) to align the saccade onsets of a cluster of saccade-to-fixation composites.

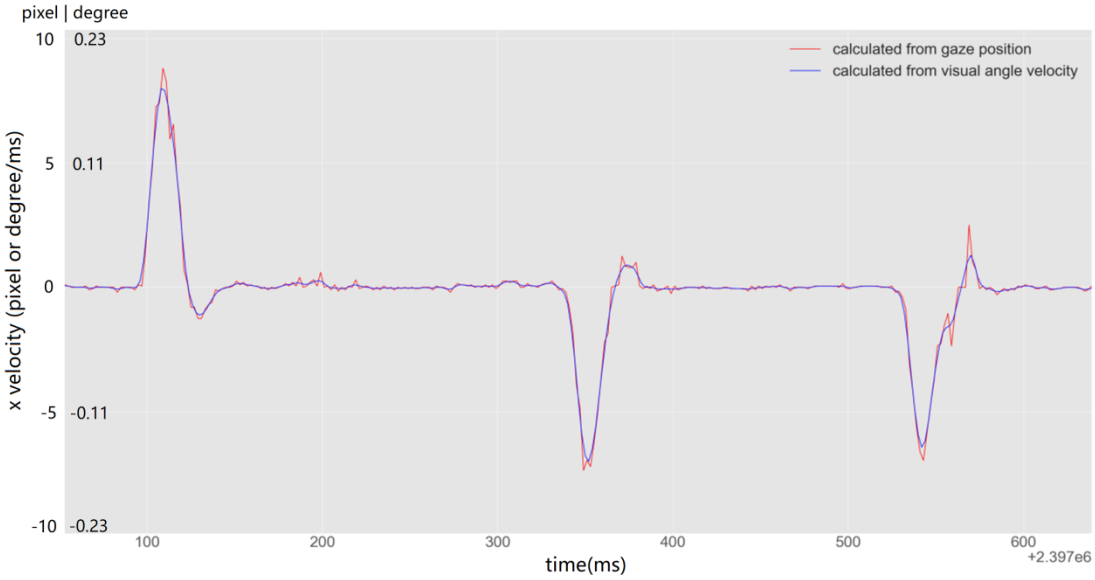

Fig. 4. Horizontal pixel velocity across time, calculated from gaze position and from visual angle velocity..

An example of the result of saccade marking for one eye is shown in Figure 5. Since a

filter was not applied to pixel velocity, the detection of saccade offset was poor when the deceleration phase of the saccade is too bumpy (the first backward saccade in Figure 5); this early stopping of the marked saccade also suggests that the velocity threshold for saccade offset (restMean +/- 3 * restStd) is too high. The adjustment of the saccade offset velocity threshold is not important because the marking of saccade offset is only tentative and will be replaced by the left boundary of PSO. Another problem that showed up is that small saccades were not detected (the third backward saccade in Figure 5). This suggests that the velocity threshold for peak/valley (restMean +/- 6 * restStd) is also too high. These two adaptive values of thresholds were set by Nyström and Holmqvist (2010) in their original paper; they probably also missed the detection of small saccades in their data. This problem did not affect later analysis of the saccade-to-fixation composite because we only selected medium-length saccades to analyse.

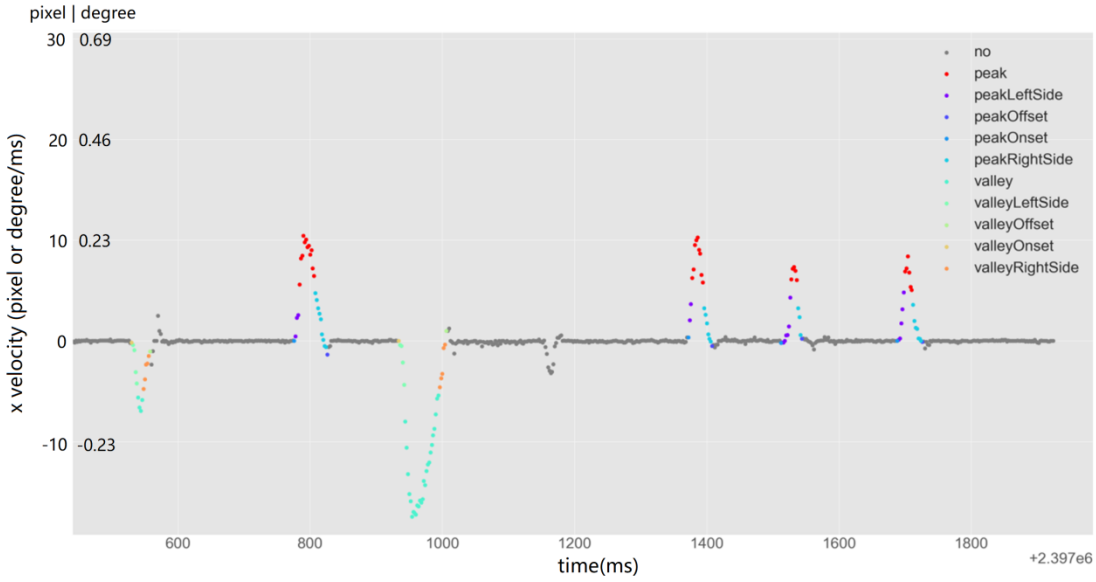

Fig. 5. Horizontal pixel velocity across time, with different phases of saccade marked.

Several words on the phenomenon of glissades are necessary: our data show that there is no such thing as a glissade during reading. One goal of the event detection algorithm Nyström and Holmqvist (2010) wrote is to detect glissades. They made a crucial assumption when they calculated the visual angle velocity from gaze position: the resulting visual angle velocities were all positive, with the negative velocity (when eye

move backwards) flipped to be positive. The result of this move is that the first backward wave in PSO was flipped to be positive and was classified as a forward glissade if its amplitude was big enough. Though the authors corrected this and studied PSO instead of glissades in later research (Nyström, Hooge, & Holmqvist, 2013; Hooge, Nyström, Cornelissen, & Holmqvist, 2015; Nyström, Andersson, Magnusson, Pansell, & Hooge, 2015), it remains to be answered whether there exist any glissades independent of PSO in normal reading (all their research on PSO is based on saccades induced by point stimuli). Figure 6 shows the trajectories of horizontal gaze position locked by their respective tentative saccade offset for all the saccades for two subjects in the English reading dataset; in addition to the trajectories, any onset of a new saccade within 200ms after the saccade offset is marked; any trajectory with new saccade onsets within 50ms after saccade offset is marked black. We only show the resulting plot for two subjects (SUB18 and SUB26). The figure shows that, except for one new saccade onset appearing right after saccade offset (which might be caused by a mistaken saccade offset marking, as shown by the first backward saccade in Figure 5), all new saccades initiate 30ms after the tentatively marked saccade offset. In addition, all these new early saccades initiated before 50ms are saccades that have normal saccade length of more than 100 pixels (2.29 degrees). Either a glissade is defined as a small corrective saccade-like movement that happens after half of the saccade (Nyström & Holmqvist, 2010), or defined as the latter of two saccades divided by a tiny fixation with a duration typically below 5ms (Holmqvist et al., 2011). Glissades (also known as ‘dynamic overshoots’ or ‘glissadic overshoots’ as cited in Nyström & Holmqvist, 2010) probably did not exist in our reading data. The glissades identified in previous literatures might be no more than a part of PSO falsely singled out as an eye event. After an inspection of the eye events marked by Eyelink eyetracker for the same English data, we did find glissades defined by (Holmqvist et al., 2011). The eye event detection algorithm

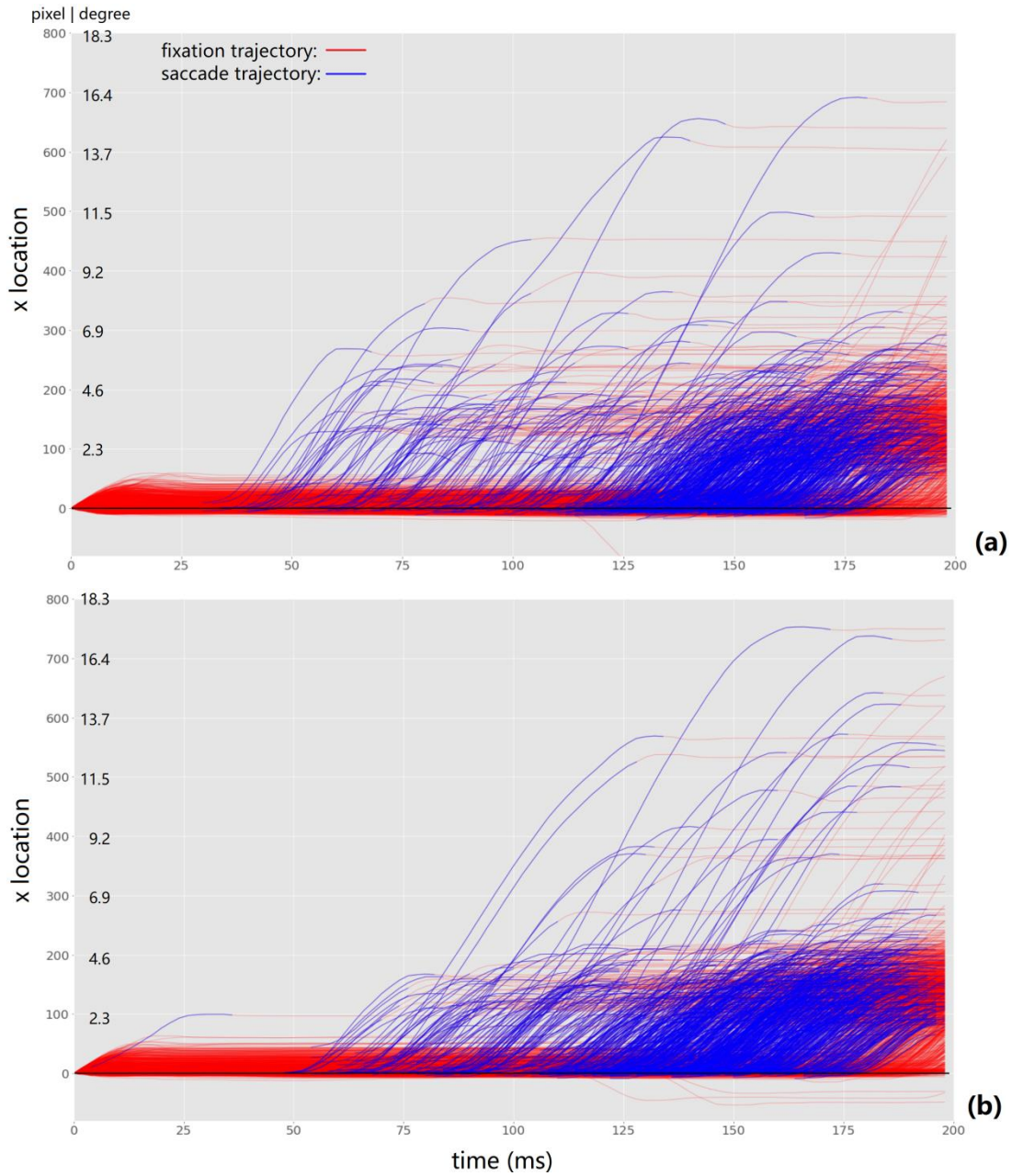

Fig. 6. Gaze trajectory within 200ms after saccade offset. Next saccade trajectories are marked. (a) Subject 18; (b) Subject 26.

indigenous to the Eyelink eyetracker might be the source of glissades in much of the relevant literature.

The marking of blinks is more reliable because change in recorded pupil size is more constrained compared to that of gaze position data. After analysing the blinks of subject SUB26, we found that the blink of the left eye constantly starts earlier and ends later than

the right eye blink by around 10ms. This observation might be useful because if the leading eye for blinks is predictive of the preferred eye for reading for the subjects, we will not have to carry out another test for preferred eye: the information already exists in reading data.

2.3.2 mark saccade-to-fixation composite

Given that saccades have been marked, this algorithm marks each saccade-to-fixation composite: a group of sample points from saccade onset to the end of the following fixation (as shown in Fig. 8 below). Saccade length was calculated if the saccade-to-fixation composite satisfies two prerequisites: 1) the composite is long enough to cover 90ms after saccade offset. This requirement makes sure the composite has at least 17ms to evaluate average fixation location, after leaving out PSO (set to be 65ms) and the section at the end of the composite (set to be 8 ms) that might be noisy because it is near the onset of the next saccade; 2) the section to evaluate average fixation location should be stable. The pixel velocity of every point in the piece should be below 2 pixel/ms (0.046 degree/ms).

The obtained saccade-to-fixation composites were then subject to the following cleaning up. A saccade-to-fixation composite was excluded from later analysis if any of its sample point 1) is of null value for gaze position or pupil size, 2) is before text is displayed on screen, 3) is in a blink, 4) is outside the boundaries of the screen, or 5) is in the nine-point-grid page for calibration checking (page named '0-1PAGE1'). Figure 7 shows the distribution of saccade length for all valid saccade-to-fixation composites in the English dataset (a) in comparison with all valid saccades detected by the default Eyelink eye event detector (b). We can see the distribution of three types of saccades from left to right: return sweep, small regressive saccade, and normal saccade. (b) has more small saccades (previously thought to be glissades) in the middle which do not exist in (a) when the saccade-to-fixation composite is the unit of measurment; this indicates glissades are not small saccades but part of PSOs. Data in (b) had been though the same clean-up process as data in (a),

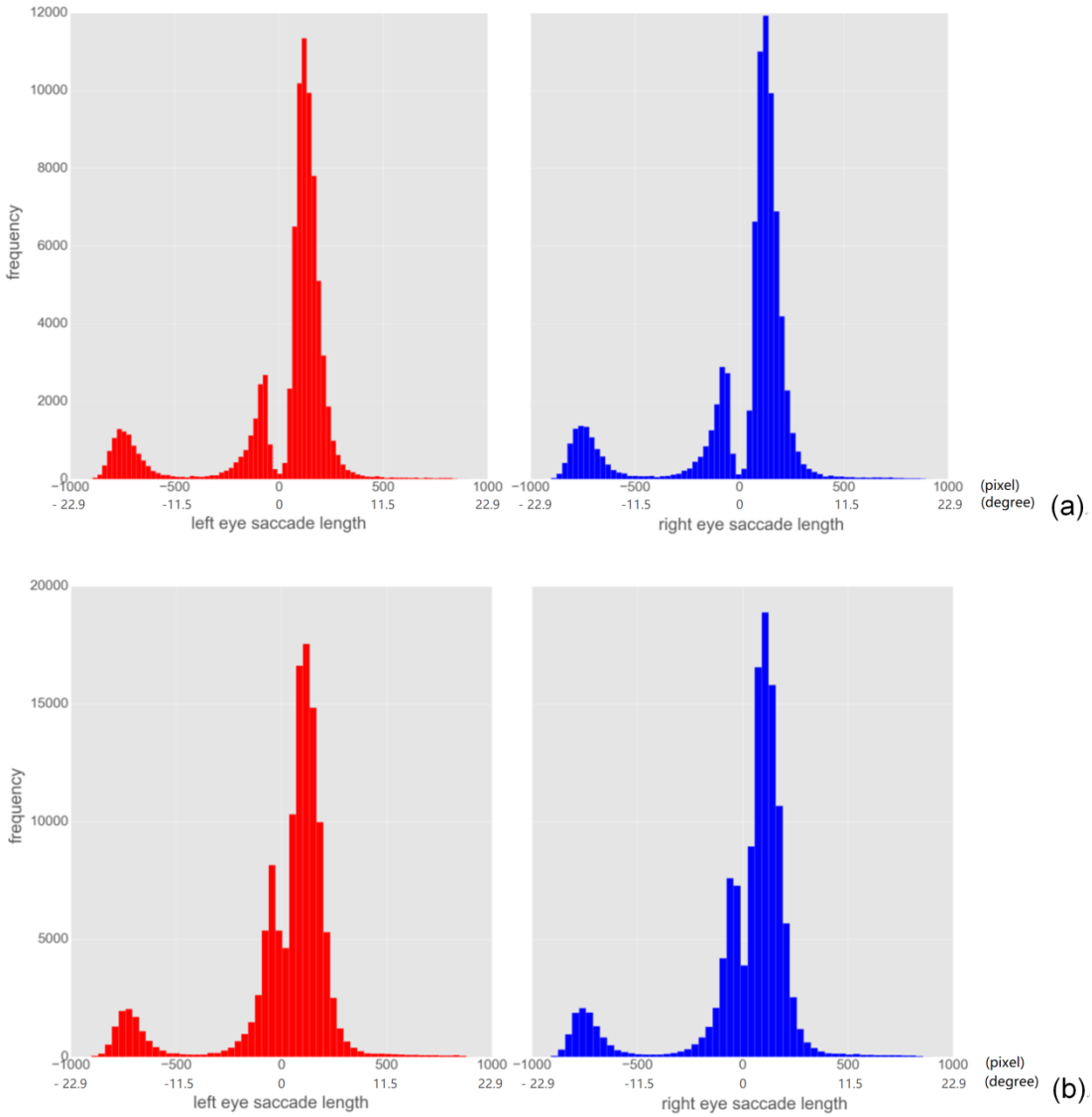

Fig. 7. (a) Distribution of horizontal saccade length of all saccade-to-fixation composites in English data. (b) Distribution of horizontal saccade length of all saccades detected by the default Eyelink eye event detector.

but (b) has larger dataset than (a). The reason is as follows: in the clean-up process a saccade or saccade-to-fixation composite has any bad sample point it is removed; saccade-to-fixation composite has much larger duration than saccade so more of them were removed (basically bad sample point at any time point would cause a removal of saccade-to-fixation composite).

Algorithm: markSaccadeAndFixtaion

Input: a Dataframe of samples for one trial(trialDf), the maximum pixel velocity that a fixation is allow to have to calculate saccade length(fixationVelocityThreshold).
Output: new samplesDf with mark columns added ('saccadeAndFixation_l', 'xSaccadeLength_l')

Algorithm: (this algorithm operates on one eye at one time, below is an example for the left eye)
1. Initiation
Add to trialDf a mark column to mark saccadeAndFixation with saccade count number ('saccadeAndFixation_l', values initiated to 'no') and a column to record saccade length ('xSaccadeLength_l', values initiated to np.nan).

# 2. mark saccade-to-fixation composite
for each saccade in trialDf:
select a set of all the sample points within the saccade by its count number.
If this set of sample points do not have either both peak onset and offset or both valley onset and offset, skip marking this saccade-to-fixation composite. # This happens when saccade is not complete due to various reasons.
Set the 'saccadeAndFixation_l' value of this saccade to its saccade count number in column 'saccade_l'. Then proliferate the 'saccadeAndFixation_l' value of this saccade rightwards to the sample points that follows it until a sample point marked with another saccade event occurred (a sample point with a 'saccade_l' value that is not 'no')

3. calculate saccade length in x coordinate for saccade-to-fixation composite
for each saccade-to-fixation:
if the sample points following the saccade offset covers no less than 90ms:
select fixation piece (sample points 65ms after saccade ending to 8ms before saccade-to-fixation ending)
if all the pixel velocity in this fixation piece is less than fixationVelocityThreshold:
saccade length = mean x location in selected fixation piece – x location at saccade onset
record saccade length into column 'xSaccadeLength_l' for each sample point in this saccade-to-fixation composite

Fig. 8. The algorithm to mark saccade-to-fixation composite.

2.4 Mean saccade-to-fixation trajectories

The aim of this stage was to produce mean saccade-to-fixation trajectories of a certain saccade length range for each eye of each participant. We selected a set of saccade-to-fixation composites with saccade length of 129-130 pixels (2.96-2.98 degrees) for both eyes of one subject (SUB18) for illustration. Three steps were taken: in Section 2.4.1 we regularized this set of saccade-to-fixation composites to a uniform format for trajectory outlier detection; in Section 2.4.2 we adjusted the time axis of saccade-to-fixation composites to limit the variance within the set caused by onset time detection variance; in Section 2.4.3 we modified and applied a trajectory outlier detection algorithm to remove outlier trajectories from the set. The mean saccade-to-fixation trajectory for each eye was calculated by taking the mean (x, y) position of all remaining trajectories at each time point.

2.4.1 regularize saccade-to-fixation composites

The algorithm is shown is Figure 9. Later analysis requires the saccade-to-fixation composite to be in uniform format for calculating the distance between trajectories. In our study, all left eye saccade-to-fixation composites were trimmed to 100ms and interpolated linearly to a time resolution of 1ms (from 2ms) in order to be fed as input to eye models in later sections; the same time region was used for right eye movement trajectory. Note that the extraction, trimming, and time shifting (in section 2.4) of the saccade-to-fixation composite were based only on the event detection markings and time axis of the left eye, the right eye movement during the extracted period was extracted to pair with the left eye movement; this makes sure that any difference in saccade movement between the two eyes was not contaminated. For those left eye saccade-to-fixations originally shorter than 100ms, we appended filler sample points (copies of the end sample point of the composite) to the tail of the composite. Though most saccade-to-fixation composites exceed 100ms, the filler sample points at the tail of some composites makes mean trajectory less interpretable near the ending. Our later analysis focused on PSO which will not be affected by the fillers, but any future claim

based on the whole mean trajectory should discard any saccade-to-fixation composite shorter than 100ms rather than append fillers to it.

Algorithm: getUniformSaccadeAndFixations

Input: a Dataframe of samples containing marking columns ‘saccadeAndFixation_l’, ‘saccadeAndFixation_r’ and ‘xSaccadeLength_l’ (sampleDf), the duration that each saccade-to-fixation composite will be trimmed to (targetDuration).
Output: uniform saccade-to-fixation composites of the form xs (a 2D array with each row represents the time axis), ys_l (a 2D array with each row represents the x coordinate of the left eye) and ys_r (for the right eye).

```
Algorithm:
for each trialDf in sampleDf:
    for each saccade-to-fixation composite Dataframe in trialDf:
        interpolate the composite to every milliseconds
        if the duration of this saccade-to-fixation composite is shorter than targetDuration:
                extend this saccade-to-fixation Dataframe by proliferating the last row till the
                Dataframe reach targetDuration.
        If the duration of this saccade-to-fixation composite is longer than targetDuration:
            Truncate the tail of this saccade-to-fixation Dataframe to fit the targetDuration.
                Collect x (time column), y_l (x location for the left eye), and y_r (x location for the
                right eye) from the resulted saccade-to-fixation composite Datarame.
        # Here we can easily extract more information of this saccade-to-fixation composite (e.g.,
        saccade lengths, fixation disparity at different time point, pupil size, etc.)
Return xs (a 2D array collects each x), ys_l, and ys_r
```

Fig. 9. The algorithm to extract regularized saccade-to-fixation composites from sample points Dataframe.

2.4.2 adjust the time axis of saccade-to-fixation composites

This algorithm (Figure 11) takes a set of saccade-to-fixation composites with similar left eye saccade length and adjusts the onset time of each trajectory to minimize its Euclidean distance to a typical trajectory in the set. A typical trajectory is set to the trajectory in the set with the smallest Euclidean distance to the mean of the trajectory set. In the search for the optimal time shift, the amount of time shift changes 1ms each loop until the Euclidean distance between the current trajectory and the typical trajectory hits its first local minimum. The optimal time shift for each trajectory was evaluated for each

left eye trajectory, then the same time shift was applied to the corresponding right eye trajectory; as a result, the trajectories of the two eye remained on the same time axis after time shifting.

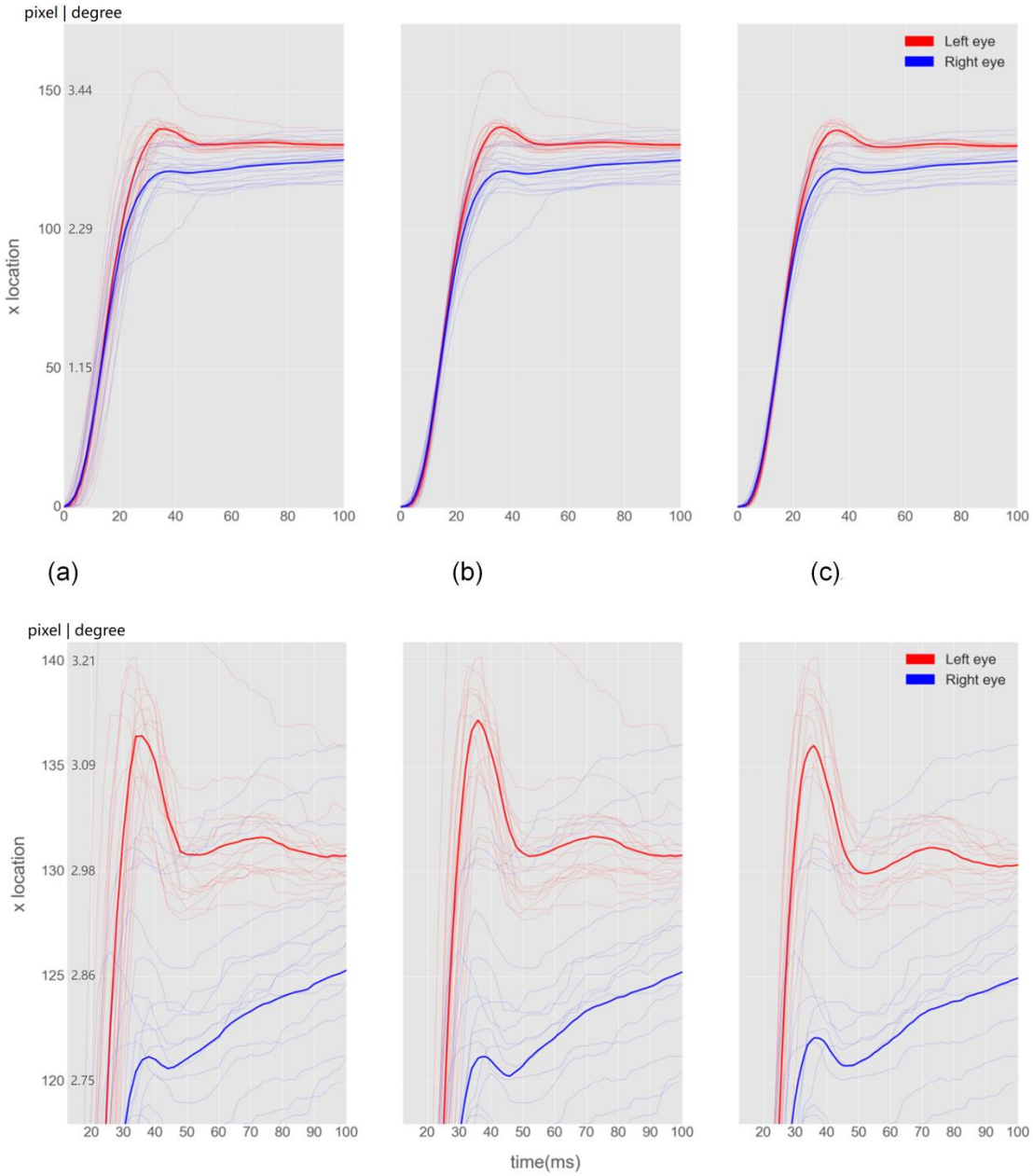

Fig. 10. Individual and mean saccade-to-fixation composite trajectories with saccade length of 129~130 pixels (2.96-2.98 degrees) for SUB18. (a) raw saccade-to-fixation composites; (b) saccade-to-fixation composites after time aligned; (c) after time aligned and outliers removed. The lower row is a zoom-in of the PSO part for each of the three.

Since the detection saccade onset suffers inaccuracy due to noise in recording, this

adjustment of time axis is necessary for obtaining a mean trajectory with well shaped PSO. Here is an example. We selected a set of saccade-to-fixation composite with saccade length of 129-130 pixels (2.96-2.98 degrees) for one subject (SUB18). The trajectories with their mean are showed in Figure 10a, and the trajectories after time shifting showed in Figure 10b; below each figure is the same plot with the PSO part zoomed in. Compare between Figure 10a and 10b, we can see left eye saccade-to-fixation composites are aligned well after time shifting; this improvement shows that there is considerable variation in the detection of saccade onset. A closer look at the PSO parts shows that the adjustment of saccade onset makes the mean PSO more prominent and wave-like. Caution should be exercised here to interpret the mean PSO for the right eye. Since the right eye saccade-to-fixation composites were not directly selected by saccade length, they have considerable variation in PSO trajectory; as result, the mean right eye PSO is not representative of the individual right eye PSOs. So the difference in mean PSO trajectory between two eyes is not entirely true. To fix this, we may separately select the same range of saccade length for both eye and derive mean PSO for two eyes separately (if the change in fixation disparity across saccade-to-fixation composites in this saccade length range averaged at 0; put in other words, if left eye saccade-to-fixation composites in this saccade length range tend to have its right eye compartment with the same saccade length).

Algorithm: shiftTime

Input: uniform saccade-to-fixation composites of the form xs, ys.
Output: time aligned ys (ys_shifted) with xs

Algorithm:
find typical trajectory among the trajectories in set
mean_x, mean_y = the mean of all rows in xs and ys respectively
for each trajectory:
    for each (x, y) point in this trajectory, calculate its Euclidean distance between its corresponding point (the point at the same place in array, i.e., at the same time point) in the mean trajectory.
    Calculate the mean of these Euclidean distances, name it as the Euclidean distance between this trajectory and the mean trajectory
The trajectory with the smallest Euclidean distance to the trajectory mean is selected as the typical trajectory

find the optimal amount of time to shift for each trajectory (the time shift that results in the first local minimum Euclidean distance between target trajectory and the typical trajectory).
For each trajectory:
    Increase the time to shift by 1ms each iteration, till the next increase of time to shift will increase the Euclidean distance between the shifted trajectory and the typical trajectory; then decrease the time to shift by 1ms till the next decrease of time to shift will increase the Euclidean distance; thus the local optimal time shift is obtained.

method to shift time for one trajectory
    The x array (time axis) keeps the same.
    The y array (x location) shift in the time frame. If shifting rightwards, fill the blank at the head with zeros; if shifting leftwards, fill the blank at the tail by the ending value in the original y array.

Fig.11. The algorithm to adjust saccade onset time of a set of saccade-to-fixation components.

2.4.3 detect trajectory outlier

To automatically exclude outliers in trajectory data, we replicated a widely cited trajectory outlier detection algorithm called TROAD (Lee, Han, & Li, 2008). In their paper, TROAD was used to detect outliers in trajectories of hurricanes and the migration of elks as examples. Two modifications were made to TROAD to suit our purposes. 1) I discarded the use of the minimum description length principle (MDL, Lee, Han, & Li, 2008,

page 6) for the setting of intermediate partition size, because in their paper the formulation of the two components of MDL (conciseness and preciseness) seems arbitrary. Instead of using MDL, I manually set the size of intermediate partition. 2) I reduced the range of searching in the search for close partitions by exploiting the fact that we are detecting outliers for time series data (explained in Figure 13). This modification makes the algorithm 10 times quicker for our data without any cost in accuracy.

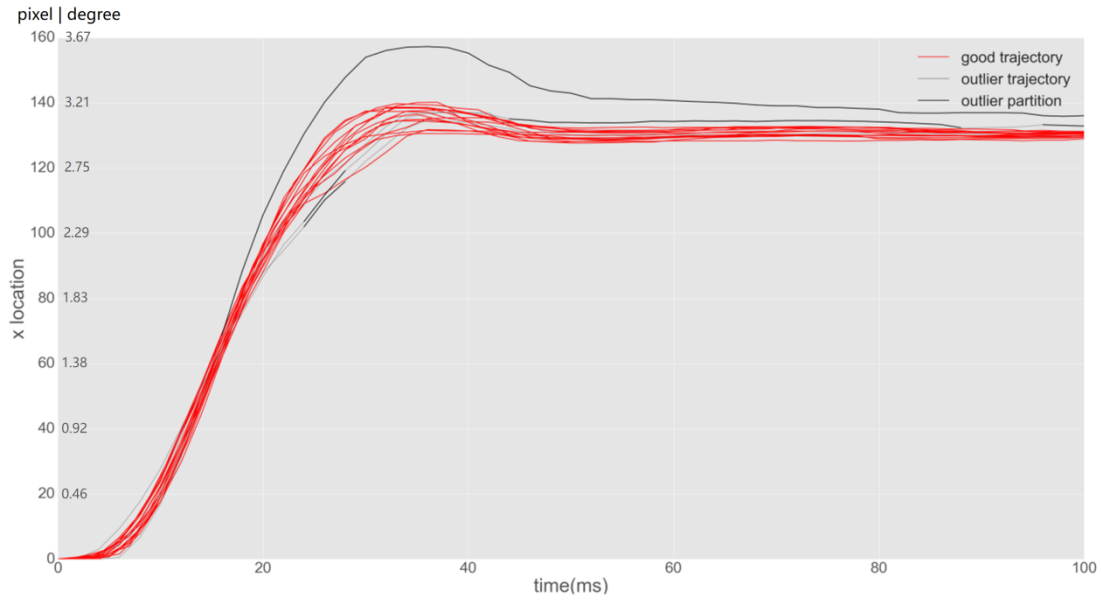

Fig.12. Result of modified TROAD: a set of saccade-to-fixation composite with outlier partitions and outlier trajectories marked.

TROAD was applied separately to left and right eye saccade-to-fixation composites. For the left eye, the parameter settings for TROAD is as follows: D = 0.5; w_perpendicular, w_parallel, and w_angular were all set to 1/3; p = 0.95; F = 0.05; partitionSize = 4. For the right eye, because the trajectories were less clustered, I changed distance threshold D to 1. The outliers were excluded pair-wise: if any one of a pair of left and right eye trajectories is an outlier in their respective trajectory set, this pair will be excluded. The resulting mean trajectories after outliers are removed are shown in Figure 10c. In addition, Figure 12 shows more detailed results of TROAD on our data,

with outlier partitions marked.

At this stage, we obtained the mean eye movement trajectories during the transition between saccade end to fixation start, where PSO happens. In the next chapter, we will use an eye movement model to model PSO for each eye of each subject, then use the estimated parameters to build a Kalman filter that can detect the boundaries among saccade, PSO, and fixation.

Algorithm: detectTrajectoryOutlier_timeSerires

Input: a set of trajectories with each trajectory contains a ordered list of data points and the data point can be of any dimension (typically two (x, y) or tree dimensions (x, y , z)); the size of intermediate partition used for the acceleration in computing speed (partitionSize); the weight for perpendicular, parallel and angular distances (w_perpendicular, w_parallel, and w_angular); the distance threshold to classify two partitions as 'close' (D); the proportion threshold to decide how much proportion of trajectories a partition should be close to be not outlying (p); the proportion threshold to decide how much proportion of outlier partition a trajectory should have to be classified as outlier trajectory (F).
Output: outlier trajectories marked, outlier trajectory partitions marked for each trajectory.

Algorithm:
The algorithm is a python copy of the entire pseudo-code provided by Lee, Han and Li (2008) with two modifications:
1. The automatic data-based derivation of intermediate partition size is set manually.
2. In the outlier detection algorithm TRAOD (Fig 6 in Lee, Han, & Li, 2008), line 04, a trajectory partition is compared to all partitions in each other partition (Lj $\in$ L and TR(Li) _= TR(Lj). This is not necessary in our time series data that has the same time axis for all trajectories, where a partition (Lj) in trajectory that is a certain distance away from the target partition (Li) on time axis will be guaranteed to be not close to Li. So we only have to search within a certain time range around Li for possible Lj that is close to Li. After translated in to index, the range is calculated to be the integer part of (((D / (timeResolution*partitionSize)) / w_parallel) + 1) left and right to the index of partition Li in TR(Li).

Fig. 13. The modification made to TROAD for time series data.

Chapter 3. Post Saccadic Oscillation (PSO) modelling and event detection

The main aim of this chapter is to develop an event detection algorithm that can identify PSO based on its oscillation cycle. Based on the oscillation trajectory of PSO, we are able to measure pupil size when pupil/iris is not deformed by force right after saccade end. The main hypothesis of this chapter is that pupil size at the first peak of PSO is smaller than the pupil size at the following first resting point of PSO.

This chapter begins with fitting an eye movement model to an exemplary saccade-to-fixation trajectory (Section 3.1). The model explains saccade-to-fixation trajectory as a compound trajectory of eyeball and pupil within the iris. Secondly, based on the mean eye movement trajectories of PSO obtained in the last chapter, we fit the PSO model to decompose the eyeball and pupil movement within PSO (Section 3.2). We found the elastic factor of the pupil decreases with age, and the viscosity of the eyeball also decreases with age. Lastly, we use the estimated parameters from Section 3.2 to construct a Kalman filter that detects the boundaries among saccade, PSO, and fixation (Section 3.3). The eye events detected by the Kalman filter shows that glissades are artifacts of the Eyelink II event detection algorithm that mistakes big PSO as new saccades. For the main hypothesis, we found that the pupil size at the first peak of PSO is smaller than the pupil size at the following first resting point of PSO. This confirms our assumption that the pupil is deformed by force at the highest peak of PSO and that the

pupil size measured at the first resting point of PSO is a more accurate pupil size measurement for the end of the saccade than that measured at the highest peak of PSO.

3.1 Eye movement model

Our aim is to build an eye movement model based on the physiology and physics of eyeball and pupil movement. However, if the model is too detailed in terms of the physiology and physics of eye movement and too complicated (i.e. too many parameters), it will be hard to fit the model to data and obtain the right values of parameters. An initial model was created basing the parameters on physiological studies of eye movement mechanics (Robinson, 1964; Robinson, 1969), cf. Komogortsev and Khan (2008), but a good saccadic trajectory failed to emerge.

In the research reported below, I chose a more abstract way to simulate eyeball movement as illustrated in figure 14. Saccadic movement is a type of point-to-point movement. Since it is hard to measure the activation of the medial and lateral rectus muscles during a saccade, and the relevant literature is limited, let us look at other instances of human point-to-point movement. During a fast elbow flexion, for example, flexor muscles contract first, later the extensor muscles starts to contract, then after

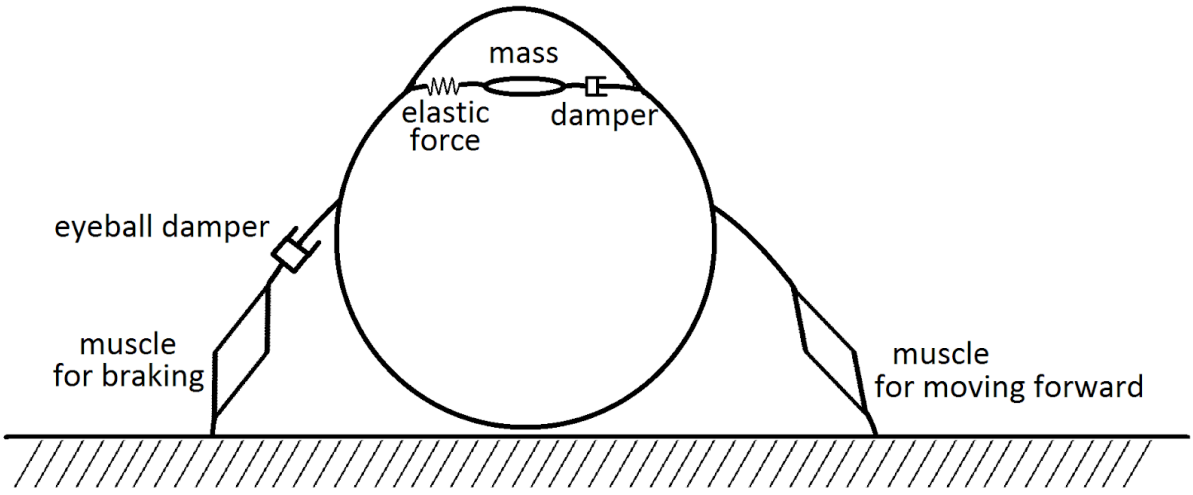

Fig.14. Eye movement model.

an additional transient activation of both muscle groups, a new elbow angle is obtained, then the co-activation fades gradually (Ostry & Feldman, 2003; Suzuki, Shiller, Gribble, &

Ostry, 2001); the medial and lateral rectus should operates in a similar way during horizontal saccadic movement (see Robinson, 1964, 1969 for an indirect measuring of medial and lateral rectus muscles). Instead of trying to incorporate all the anatomical and physiological components of muscle and eyeball, I try to simulate the saccadic eyeball movement by three hypothetical forces: the force for move and the force for break, plus a damping force. The forces for move and break each have three parameters: start time, speed and duration of increase; each force starts to increase from zero at the start time, increases gradually at the speed of increase for the specified duration of increase, then decreases gradually at the same speed of increase until it restores to zero. The damping force has one parameter dictating how big the force is in proportion to velocity. To model PSO, two parameters are chosen for pupil movement relative to the eyeball: elastic force and damping force. Elastic force is proportional to the displacement of pupil relative to eyeball, and damping force is proportional to the relative velocity of pupil in the eyeball. In the initial state the eyeball keeps still at one location and the pupil keeps still in the centre of the eyeball. After the system starts at the start time of the force of move, the system of eyeball and pupil moves by the law of physics and eventually restores to stillness with the eyeball having moved to another location. The code updates the forces and movements by the specified time interval (0.1ms in our settings) and produces the trajectory of eyeball and pupil movement during the saccade. (Instead of simulating the trajectory by code, we could have derived discrete functions for the parameters—because move and break forces are discrete—and calculated the trajectory, which would be much less computationally costly than simulating the trajectory time point by time point.)

Having obtained the model, the next stage is to fit the model to the data. It is difficult and unreliable to fit all 9 parameters at the same time. To reduce the difficulties, we extracted the PSO part from the left eye trajectory and used PSO to fit the two parameters of the pupil (elastic force and damping force). Following Tabernero and Artal (2014), we set the time point where the amplitude of PSO is maximum as the left boundary of PSO; the right boundary is set to be 70ms after the left boundary. Given the

elastic force factor k_p, the viscosity b_p, the initial position A_0, and the initial phase ($\pi/2$), the formula for damped harmonic oscillation is as follows:

$$F(t) = A_0 * e^{(-\frac{b_p}{2}*t)} * \sin\left(\sqrt{k_p - \frac{b_p^2}{4}} * t + \frac{\pi}{2}\right) \quad \ldots. (1)$$

Since the oscillation happens approximately on a tilted straight baseline, we added line with slope d_{slope} and intercept $d_{intercept}$ to the oscillation formula. So, overall the formula to fit is:

$$F(t) = A_0 * e^{(-\frac{b_p}{2}*t)} * \sin\left(\sqrt{k_p - \frac{b_p^2}{4}} * t + \frac{\pi}{2}\right) + d_{slope} * t + d_{intercept} \quad \ldots. (2)$$

We used Least Squares Fitting in the scipy library of python (scipy.optimize.leastsq). To fit formula 2 to the left eye PSO we selected, with the initial value of parameters set to: k_p = 0.2, b_p=0.5,

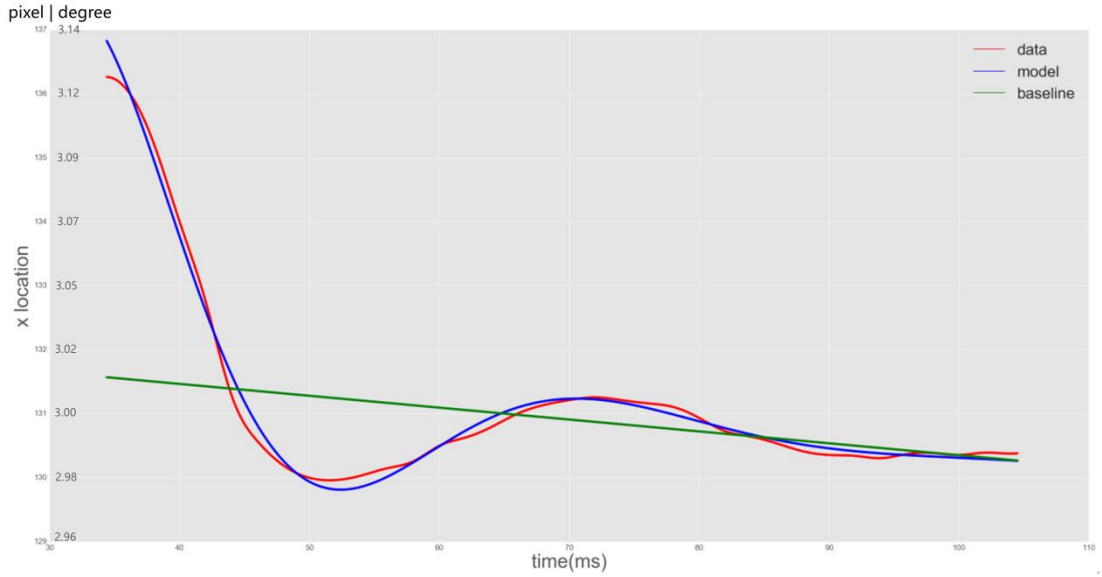

Fig.15. Result of model fitting for mean PSO.

A_0=10, d_{slope}= 0, $d_{intercept}$=135. The result shows a good match between PSO data and formula 2 (as shown in Figure 15). The fitted values of the parameters are: k_p = 0.029, b_p=0.14, A_0=5.3, d_{slope}= -0.019, $d_{intercept}$=131.5. These results yield a damping ratio ($\frac{b_p}{2\sqrt{k_p}}$) of 0.40 and a natural frequency ($1000/\frac{2\pi}{\sqrt{k_p}}$) of 27.0 Hz for pupil PSO. The damping ratio of lens PSO in Tabernero and Artal (2014) is calculated to be between 0.3 and 0.7, and natural frequency to be 15 ~ 20 Hz. It is reasonable that pupil oscillation is quicker

than lens oscillation because the lens is a relatively big mass suspended and looks less rigidly locked to its place than does the iris muscles (and thus the pupil), hence a smaller frequency in harmonic oscillation.

There is one drawback to this calculation: the mean PSO may not be a good representative of the individual PSOs. Just like the mean saccadic movement trajectory does not represent well the set of trajectories if the trajectories are not aligned well; as the onset of PSOs (when the maximum oscillation amplitude appears) is not perfectly aligned even after the alignment of whole saccade trajectories, the PSO trajectories here should be aligned by their onset to yield a more representative mean PSO. Surprisingly, the mean PSO did not change much after alignment of PSO onset (as showed in Figure 16). It seems that PSOs are already well aligned. We went on to exclude outliers in PSO using modified TROAD, but it did not make much difference either. Finally, we fitted formula 2 to the cleaned-up mean PSO (time aligned and outlier detected) and the result is as follows: $k_p = 0.028$, $b_p = 0.14$, $A_0 = 5.1$, $d_{slope} = -0.014$, $d_{intercept} = 131.3$, damping ratio = 0.41, natural frequency = 26.6Hz. The cleaning-up does not make much difference for this subject in the saccade length range, but it could have made a considerable difference if the outlier PSOs were not distributed evenly on both sides of mean PSO.

Having obtained the elastic factor k_p and viscosity b_p of pupil, we went on to fit the rest of the seven parameters for the eyeball to complete the eye movement model. We used gradient descent to find the optimal value of the seven parameters which minimize the Euclidean distance between the model and the interpolated mean eye movement trajectory of the left eye. We used ‘bold drive’ to regulate the learning rate. Since it was hard to fit seven parameters at the same time, we used the trajectory before gaze position reaches 60% of its full saccade to train the three parameters of move force and viscosity of eyeball in order to give a good starting estimation, then used the full trajectory to fit all seven parameters. The discreteness of time parameters (start time and duration for the two forces) made it difficult to calculate partial derivatives of these parameters for gradient calculation. The current solution is to make the simulation more fine-grained to

make the time parameters less discrete, but this is computationally expensive. Future research should employ the mathematical formulas for the model instead of the current simulation on each time

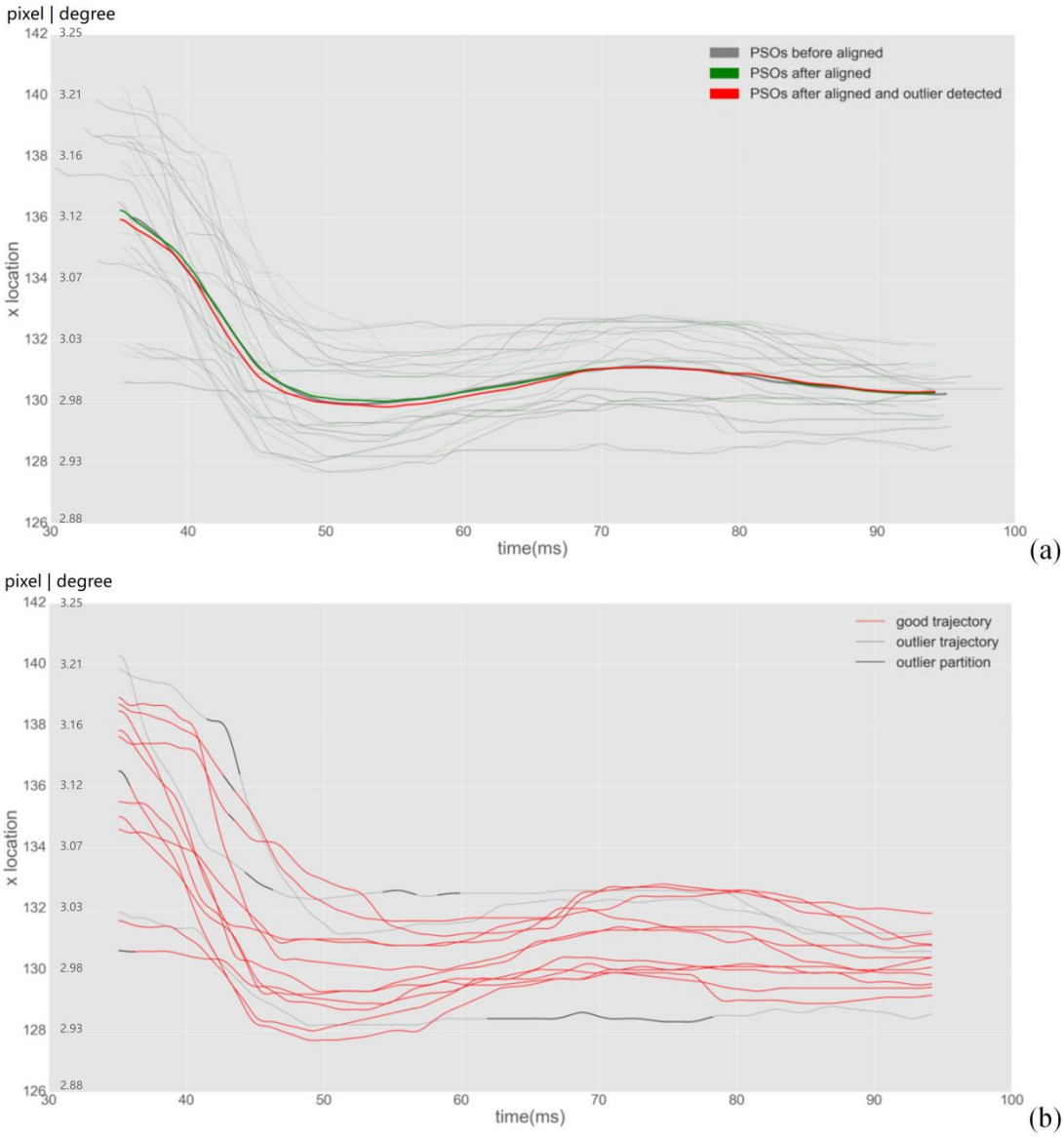

Fig. 16. (a) clean-up process for the set of PSO. (b) detailed results of modified TROAD applied on the set of PSO.

point. Another problem is that, during gradient descent, the speed of increase for the move and break force (c_move and c_break) were not updated in tandem; often the shape of the trajectory can be improved by increasing or decreasing the two at the same time, but gradient descent will not do that because the partial derivatives only take into

account one parameter at a time and will not point the updating to the right direction. My solution was to c_break with a difference factor that represents the difference of speed of increase between the two forces (c_diff = c_break – c_move); in this way, the updating of c_move will update the speed of increase for both forces. The results of fitting are: startTime_move = -5.5, c_move = 0.25, duration of increase for the move force (tc_move) = 7.3, startTime_break = 10.5, c_diff = 0.030, tc_break = 2.7, $b_{eyeball}$ = 0.087. The outcome trajectories of eyeball, pupil, and the compound of the two are shown in Figure 17. We can see that the model is of limited success. The end of

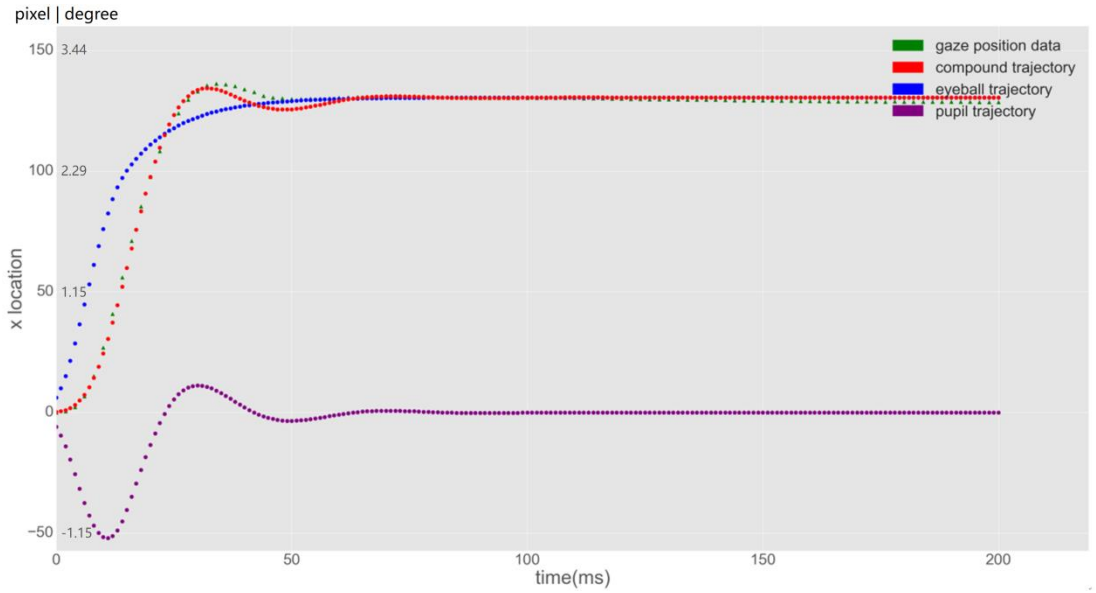

Fig. 17. The simulated trajectories of eyeball, pupil, and the compound of the two.

saccade of the eyeball trajectory does not resemble that in previous research (Tabernero & Artal, 2014), and the pupil displacement is too large during saccade. In future research, we need to introduce active state tension to sharpen the eyeball trajectory at the end of saccade; this will also reduce the maximum amplitude of PSO (part of the first overshooting will be assigned to the eyeball caused by the elasticity brought by active state tension), consequently increasing the estimated elastic force of pupil k_p, and hence reducing the displacement of pupil location during the saccade in our model. One

problem in fitting our model is that with seven free parameters the model has too many choices of combinations of parameter values to match the gaze position trajectory in data.

3.2. Experiment 1: Estimation of Pupil Elastic Factor, Pupil Viscosity, and PSO Amplitude

The last section demonstrated how eye movement recorded by video eye-tracker can be decomposed into eyeball and pupil movement with an eye model. In this section we fit the eye model to all PSO trajectories in our data to estimate the pupil elastic factor (k_p), pupil viscosity (b_p), and the maximum PSO amplitude (A_0) for all available saccade length for both eyes of all subjects. We aim to check if our results confirm the findings of Mardanbegi et al. (2018) that oscillation amplitude increases with age, for which we hypothesise that the maximum PSO amplitude (A_0) is higher in elder people for both left and right eyes. The parameter k_p and b_p for each subject obtained here will be used in the next section for implementing the Kalman filter in order to estimate eyeball viscosity and the first resting point of PSO at saccade end.

3.2.1. Method

Based on the saccade-to-fixation trajectory extraction method in Chapter 3, we obtained the mean saccade-to-fixation trajectories for all available saccade size bins with a bin size of 2 pixels ([i, i+1] for i = -200, -198, -196, …, 198; i.e., -4.58 to 4.54 degrees with an interval of 0.045 degrees) for both eyes of each subject. For each mean saccade-to-fixation trajectory we sliced out the mean PSO trajectory: following Tabernero and Artal (2014), we set the time point where the amplitude of PSO is maximum as the left boundary of mean PSO trajectory; the right boundary was set to be 70ms after the left boundary. Based on equation (2) in section 3.1, we used least square optimization to estimate the pupil elastic factor (k_p) and pupil viscosity (b_p), and the maximum PSO amplitude (A_0).

The data were split into leftward reading language data (Arabic and Hebrew; dataset AH) and rightward reading language data (Chinese, English, and Spanish; dataset CES).

Backward reading saccades (rightward saccades in leftward reading data and leftward saccades in rightward reading data) were removed from dataset AH and CEC. The eye may have different A_0 in PSO when it moves in nasal and temporal directions, so we removed the saccades with the smaller proportion (backward reading saccades compared with forward reading saccades) to obtain an average A_0 for forward reading saccades only. For each eye of each subject, average k_p , k_p and A_0 were calculated after outliers were removed for the fitting error, k_p, k_p and A_0 among different forward saccade lengths. We used lme4 package (Bates, Maechler & Bolker, 2012) with R (Bates, Maechler & Bolker, 2012) to conduct a linear mixed effects analysis of the relationship between A_0 and age of subjects. For fixed effects, we added age and eye (left or right) into the model; for random effects, we added intercepts for subjects. Likelihood ratio tests were conducted between full model with the target effect and null model without the target effect to calculate p-values.

3.2.2. Results and Discussion

3.2.2.1. Mean saccade-to-fixation trajectories

The mean saccade-to-fixation trajectories for both eyes of two example subjects (SUB19, SUB20) are shown in Figure 18. The oscillations at the end of saccades resemble those in previous work (Nyström, Hooge, & Holmqvist, 2013; Larsson, Nyström, & Stridh, 2013; Tabernero & Artal, 2014; Hooge, Nyström, Cornelissen, & Holmqvist, 2015; Nyström, Andersson, Magnusson, Pansell, & Hooge, 2015; Bouzat, Freije, Frapiccini, & Gasaneo, 2018; Mardanbegi et al., 2018; Punta, Rodriguez, Gasaneo, & Bouzat, 2019).

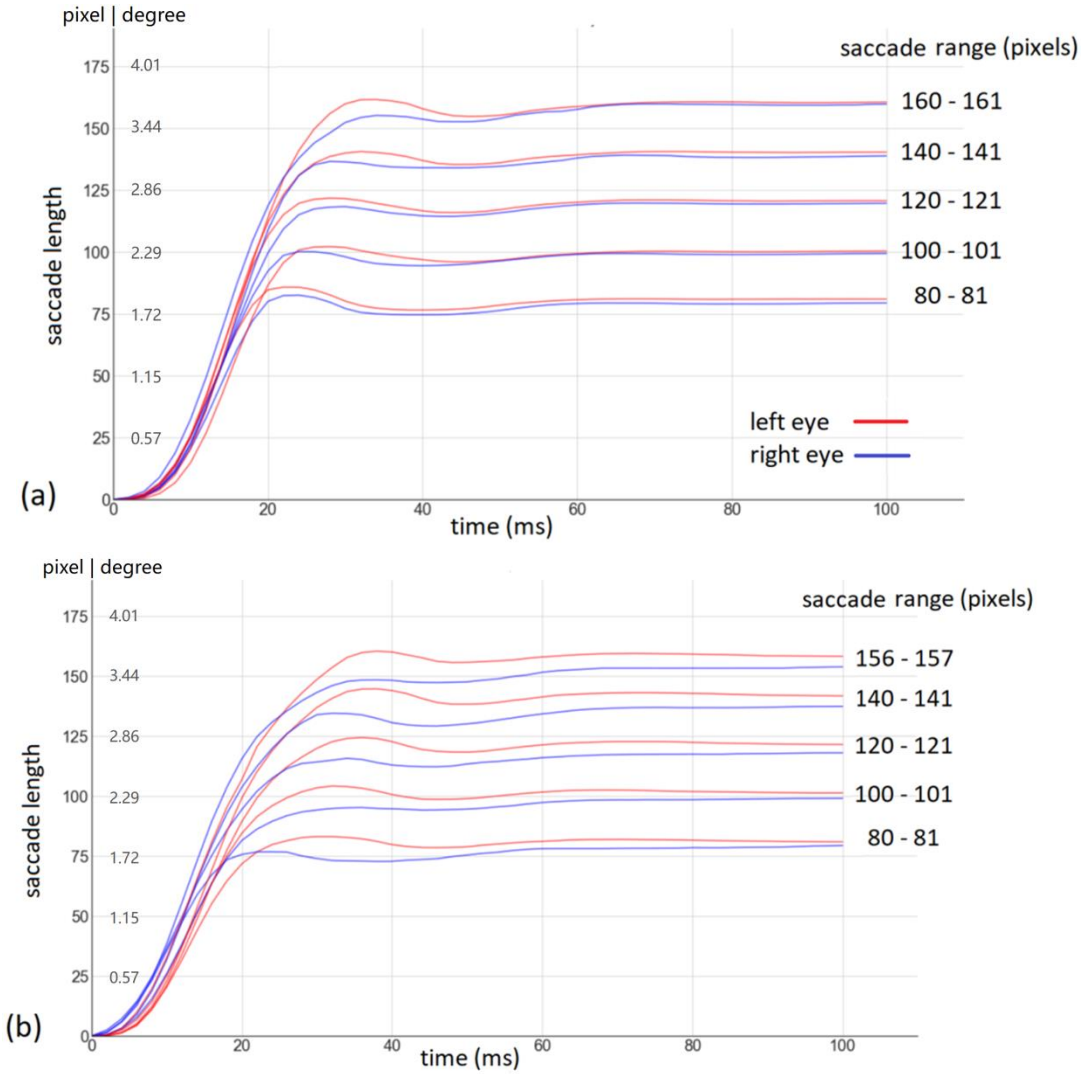

Fig. 18. Mean saccade-to-fixation trajectories for different ranges for both eyes of two subjects. (a) for subject SUB19; (b) for subject SUB20.

3.2.2.2. Maximum PSO amplitude A_0

For forward saccades in leftward reading data (dataset AH), the mean maximum PSO amplitude A_0 was 3.30 ± 2.23 pixels (0.076 ± 0.051 degrees) for the left eye PSO and 2.50 ± 1.56 pixels (0.057 ± 0.036 degrees) for the right eye PSO. For forward saccades in rightward reading data (dataset CES), A_0 was 2.21 ± 1.94 pixels (0.051 ± 0.044 degrees) for the left eye PSO and 2.41 ± 2.61 pixels (0.055 ± 0.060 degrees) for the right eye PSO. Figure 19 presents the scatter plot between A_0 and age with a regression line fitted to the points for both eyes in dataset AH and CES. Visual inspection of Fig. 19 suggests that A_0 increases with age for both dataset AH and CES. Fig. 19 also

suggests that A_0 of the left eye PSO is larger than the A_0 of the right eye PSO when saccade direction is to the left (Fig. 19a), while A_0 of right eye PSO is larger than the A_0 of left eye PSO when saccade direction is to the right (Fig 19b). This can be summarized as the PSOs of the abducting eye (moving temporally) is larger than that of the adducting eye (moving nasally).

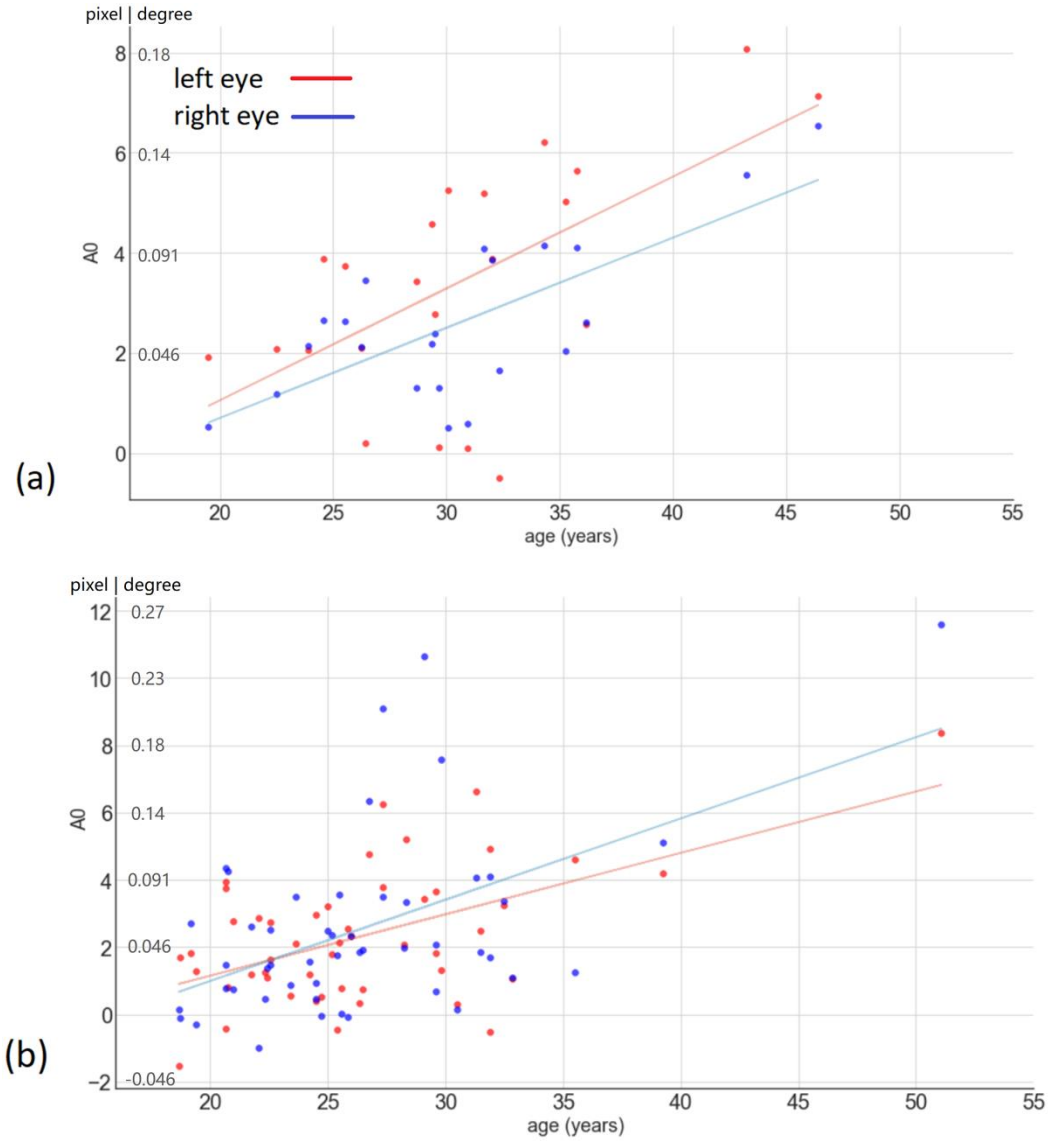

Fig. 19. (a) Relationship between maximum PSO amplitude and age of subjects for leftward saccades in Arabic and Hebrew readers. Pearson's r = 0.61 for the left eye and 0.72 for the right eye. (b) Relationship between maximum PSO amplitude and age of subjects for rightward saccades in Chinese, English, and Spanish readers. Pearson's r =.54 for the left eye and 0.52 for the right eye.

We constructed a linear mixed effects model of A_0 as a function of age (fixed effect), gender (fixed effect), and subject (random intercept). Results showed that, for Arabic and Hebrew readers, PSO amplitude of left eye PSOs is larger than that of right eye PSOs by 0.81 ± 0.04 pixels (0.019 ± 0.001 degrees; $\chi 2$ (1)=4.51, p = 0.03); for Chinese, English and Spanish readers, PSO amplitude of right eye PSOs is slightly larger than that of left eye PSOs by 0.22 ± 0.30 pixels (0.0050 ± 0.0069 degrees), but this effect was not significant ($\chi 2$ (1)=0.52, p = 0.47). Based on our eye movement model, the elevated PSO amplitude for the abducting eye can be explained by the difference in the strength of the muscles that move the eyeball: at the acceleration phase of saccade, the abducting eye is moved by the lateral rectus muscle and the adducting eye by the medial rectus muscle; because the lateral rectus muscle is stronger than the medial rectus muscle, the abducting eye may have a more abrupt acceleration that displaces the pupil more and thereby stores more elastic potential energy, which causes a stronger PSO at the end of the saccade. The simulation of this effect will be presented in Section 3.4. Also, for Arabic and Hebrew readers, PSO amplitude increased with age by 0.20 ± 0.04 pixels (0.0046 ± 0.001 degrees) per year ($\chi 2$ (1) = 15.51, p < 0.001); for Chinese, English and Spanish readers, PSO amplitude increased with age by 0.21 ± 0.04 pixel per year (0.0048 ± 0.001 degrees; $\chi 2$ (1) = 20.92, p < 0.001). This confirms the results of Mardanbegi et al. (2018) that PSO amplitude increases with age. To investigate the reason for this increase of PSO amplitude, we conducted further analysis of the relationship between other parameters in our model (k_p, b_p) and age.

3.2.2.3. Pupil elastic factor k_p and pupil viscosity b_p

For forward saccades in leftward reading data (dataset AH), the mean pupil elastic factor k_p was 0.028 (SD = 0.010) for the left eye PSO and 0.031 (SD = 0.009) for the right eye PSO. For forward saccades in rightward reading data (dataset CES), k_p was 0.033 (SD = 0.011) for the left eye PSO and 0.032 (SD = 0.012) for the right eye PSO. Figure 20 presents the scatter plot between k_p and age with a regression line fitted to the points for both eyes in dataset AH and CES. Visual inspection of Fig. 20 suggested that k_p

decreases with age for the left eye in dataset AH, but there seemed no substantial relationship between k_p and age for the right eye in dataset AH or either eye in dataset CES.

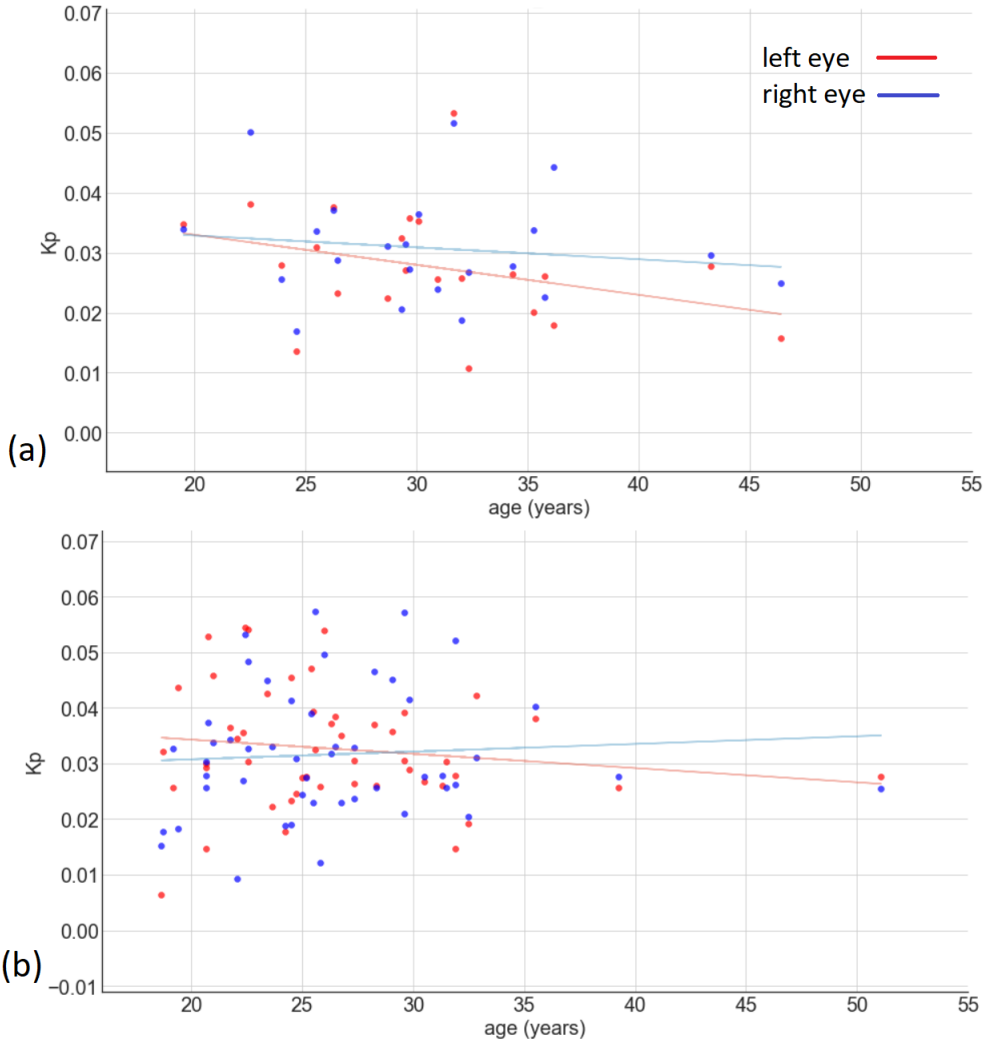

Fig. 20. (a) Relationship between pupil elastic factor and age of subjects for leftward saccades in Arabic and Hebrew readers. Pearson's r = -0.33 for the left eye and -0.13 for the right eye. (b) Relationship between pupil elastic factor and age of subjects for rightward saccades in Chinese, English, and Spanish readers. Pearson's r = -0.14 for the left eye and 0.07 for the right eye.

We constructed a linear mixed effects model of k_p as a function of age (fixed effect), gender (fixed effect), and subject (random intercept). Results showed that, the pupil

elastic factor does not change with age for Arabic and Hebrew readers ($\chi 2$ (1) = 1.65, p = 0.20), or Chinese, English and Spanish readers ($\chi 2$ (1) = 0.06, p = 0.80).

For forward saccades in leftward reading data (dataset AH), the mean pupil viscosity b_p was 0.11 (SD = 0.071) for the left eye PSO and 0.11 (SD = 0.049) for the right eye PSO. For forward saccades in rightward reading data (dataset CES), b_p was 0.10 (SD = 0.042) for the left eye PSO and 0.096 (SD = 0.057) for the right eye PSO. Figure 21 presents the scatter plot between b_p and age with a regression line fitted to the points for both eyes in dataset AH and CES. Visual inspection of Fig. 21 suggested that b_p increases with age in dataset AH, but there seemed no substantial relationship between b_p and age in dataset CES.

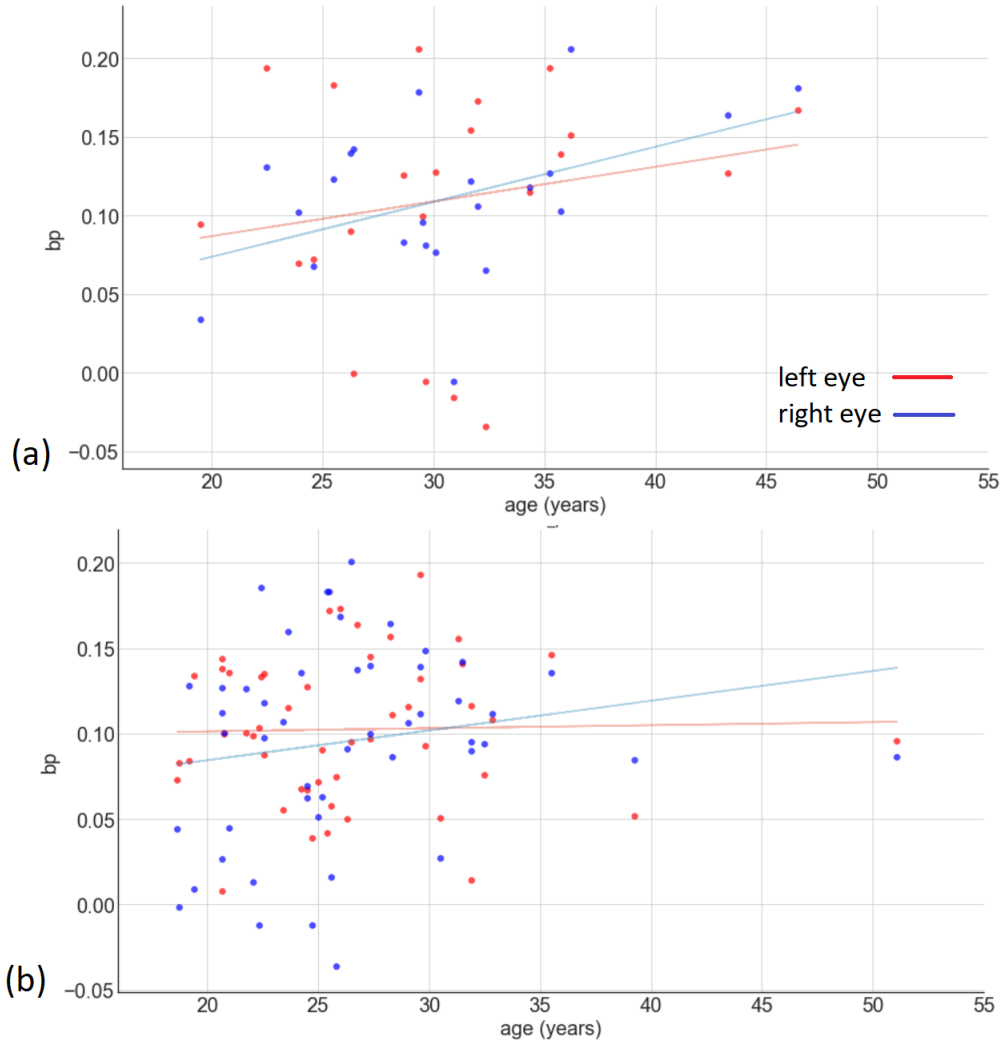

Fig. 21. (a) Relationship between pupil viscosity and age of subjects for leftward saccades in Arabic and Hebrew readers. Pearson's r = 0.20 for the left eye and 0.45 for

the right eye. (b) Relationship between pupil viscosity and age of subjects for rightward saccades in Chinese, English, and Spanish readers. Pearson's r = 0.02 for the left eye and 0.18 for the right eye.

We constructed a linear mixed effects model of b_p as a function of age (fixed effect), gender (fixed effect), and subject (random intercept). Results showed that the pupil viscosity does not change with age for Arabic and Hebrew readers ($\chi2$ (1) = 2.67, p = 0.10), or Chinese, English and Spanish readers ($\chi2$ (1) = 0.86, p = 0.35). Though it seemed that k_p had a slight negative correlation with age and b_p had a slight positive correlation with age, none of these changes were significant. In the next section, to further investigate why maximum PSO amplitude A_0 increases with age, we calculated and analysed the damping ratio $\mathfrak{o}$ of PSO ($\sigma = \frac{b_p}{2\sqrt{k_p}}$) by viewing PSO as a damped harmonic oscillation.

3.2.2.4 Damping ratio $\mathfrak{o}$ of PSO

For forward saccades in leftward reading data (dataset AH), the mean damping ratio $\mathfrak{o}$ was 0.34 (SD = 0.23) for the left eye PSO and 0.32 (SD = 0.15) for the right eye PSO. For forward saccades in rightward reading data (dataset CES), $\mathfrak{o}$ was 0.29 (SD = 0.11) for the left eye PSO and 0.27 (SD = 0.16) for the right eye PSO. Figure 22 presents the scatter plot between b_p and age with a regression line fitted to the points for both eyes in dataset AH and CES. Visual inspection of Fig. 22 suggested that $\mathfrak{o}$ increases with age in dataset AH, but that this relationship was much weaker in dataset CES.

We constructed a linear mixed effects model of $\mathfrak{o}$ as a function of age (fixed effect), gender (fixed effect), and subject (random intercept). Results showed that, for Arabic and Hebrew readers, PSO damping ratio increased with age by 0.011 ± 0.0051 per year ($\chi2$ (1) = 4.45, p = 0.03); for Chinese, English and Spanish readers, PSO amplitude increased with age by 0.0030 ± 0.0027 per year, but this effect was not significant ($\chi2$ (1) = 1.12, p = 0.29).

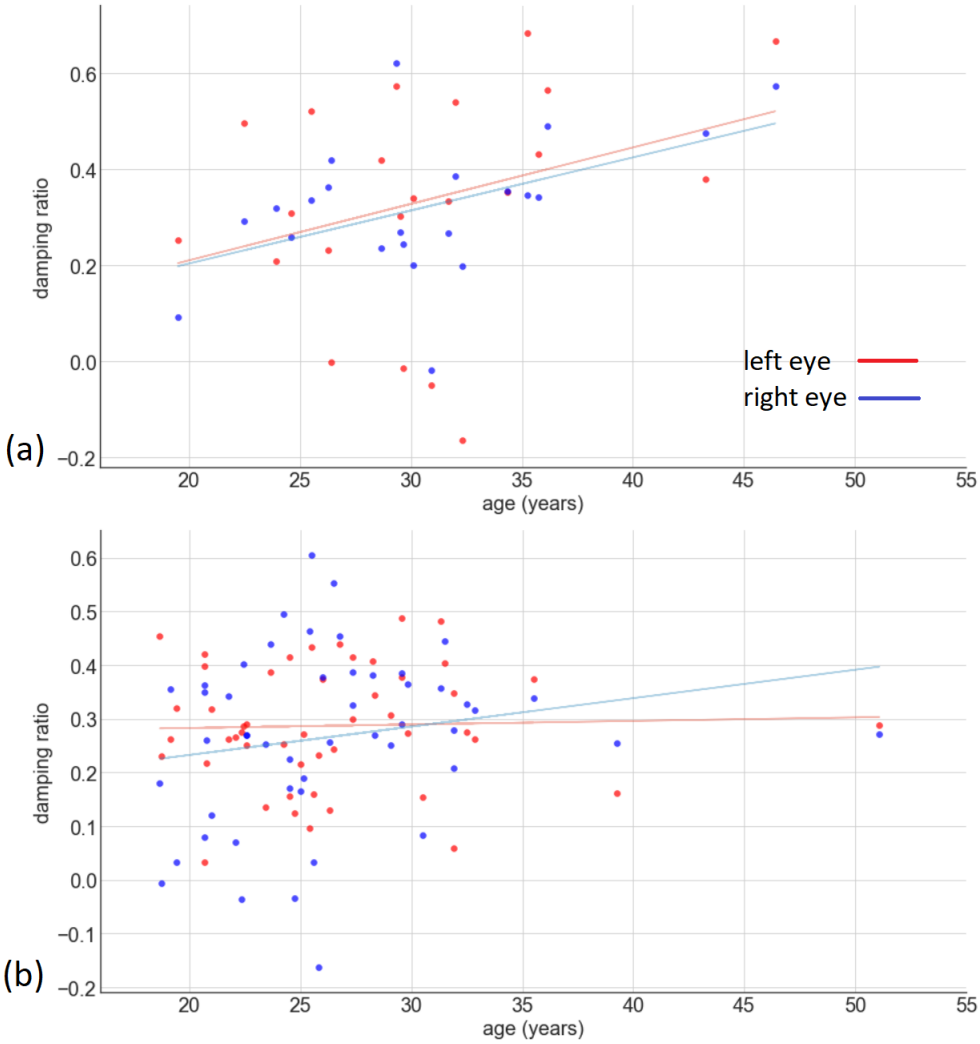

Fig. 22. (a) Relationship between PSO damping ratio and age of subjects for leftward saccades in Arabic and Hebrew readers. Pearson's r = 0.32 for the left eye and 0.48 for the right eye. (b) Relationship between PSO damping ratio and age of subjects for rightward saccades in Chinese, English, and Spanish readers. Pearson's r = 0.03 for the left eye and 0.19 for the right eye.

3.2.2.5 Possible reasons for PSO amplitude increasing with age

Since the results for the rightward reading data (dataset CES) lack significance, we focus our discussion on the leftward reading data (dataset AH). For dataset AH, with the increase of age, both the maximum PSO amplitude and damping ratio increases; also, with marginal significance, the pupil elasticity decreases and viscosity increases. In our eye movement model, with other parameters fixed, the decrease of pupil elasticity should increase the pupil displacement to the centre of eyeball during the saccade, hence

increasing the PSO amplitude at the end of saccade. However, with other parameters fixed, the increase of viscosity should reduce the speed of pupil when it is whipping towards the peak of PSO at the end of saccade, hence reducing the maximum PSO amplitude. A tentative conclusion would be that the effect of pupil elasticity decreasing with age on PSO amplitude is bigger than the effect of pupil viscosity increasing with age, so that PSO amplitude grows with age.

But the story is more complicated when we take into account the pupil movement before the biggest peak of PSO. At the end of saccade, the eye ball decelerates and the pupil centre should pass through the centre of the iris, then the pupil oscillates around the centre of the iris (the resting point) with diminishing amplitude. These parameter values we presented above were best fitted to the PSO trajectory starting from the biggest peak of PSO. Here we discuss whether these parameters can still explain the PSO trajectory starting a quarter cycle earlier when pupil centre is at the centre of the iris. If we assume a fixed speed of pupil when it first passed the resting point and the eyeball stops completely at this time point, the amplitude of the first and biggest peak of PSO will depend on the damping ratio. The bigger the damping ratio ($0 <= \zeta < 1$) is, the smaller the PSO amplitude. In dataset AH, the maximum PSO amplitude changed from approximately 1 pixel at age 20 to 7 pixels at age 45 (0.023 to 0.16 degrees), while the corresponding elasticity changed from around 0.035 to 0.025, viscosity from 0.08 to 0.15. A simulation of the damped harmonic oscillation of the pupil across different ages is presented in Figure 22. We can see that the change in damping ratio does not bring much change much to the amplitude of first peak of PSO. This follows from the fact that the increase of maximum PSO amplitude must come from the increase of initial pupil velocity at the end of the saccade. In order to increase the maximum PSO amplitude by 7 times (from 0.023 degrees at age 20 to 0.16 degrees at age 45), the initial velocity should increase by 7 times given zero viscosity, which amounts to 49 times the elastic potential energy. What changes in saccade movement could cause this drastic change of pupil dynamics at the end of saccade?

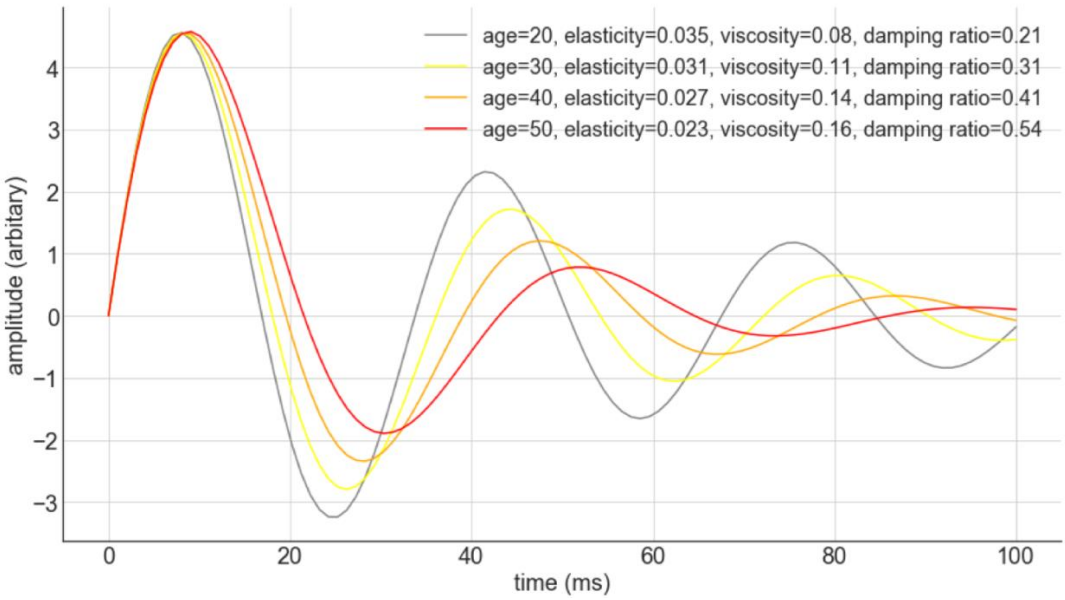

Fig. 22. The PSO trajectory across age with initial pupil velocity fixed.

There is an alternative explanation to the relationship between maximum PSO amplitude and age – the increased PSO amplitude is an artefact of pupil-CR eye tracking that increases with age. The PSO trajectory we used from pupil-CR eye tracking is a linear combination of pupil oscillation trajectory and CR oscillation trajectory (Hooge, Holmqvist, & Nyström, 2016) The combination process of pupil-CR trajectory can be expressed in formula (1):

pupil-CR trajectory = pupil trajectory – CR trajectory …. (1)

If we set α(0 <=α< 1) as the proportion of CR saccade length against eyeball saccade length and discompose pupil trajectory to pupil displacement to iris centre and eyeball movement, we have formula (2):

pupil-CR trajectory/(1 –α) = eyeball trajectory + pupil displacement trajectory/(1 –α)

This formula shows that the increased amplitude of PSO in older people can be caused by not only 1) the increased speed of the pupil as the pupil passes the resting point at the end of the saccade, but also 2) the increased proportion (α) of CR saccade

length against eyeball saccade length. With age, the cornea can become more bulgy so that α can grow (Mardanbegi et al., 2018).

In Section 3.4 we will simulate the whole saccade-to-fixation trajectory to show how the changes in muscle forces can cause the increase of PSO amplitude through 1); and show how the changes in corneal bulge can cause the increase of PSO amplitude through 2). In the next section, we use the Scaled Unscented Kalman filter (UKF; Julier, 2002) to apply our current eye model on eye tracking data.

3.3 Experiment 2: PSO detection by Kalman Filter

In the last section we estimated the value of pupil elasticity and viscosity with an eye model. In this section we use the Scaled Unscented Kalman filter (UKF; Julier, 2002) to apply our eye model to eye tracking data in order to detect boundaries and different phases of PSO. We hypothesize that pupil size at the first peak of PSO is smaller than pupil size at the following first resting point of PSO. The findings supported our hypothesis. This confirms our assumption that the pupil is deformed by force at the highest peak of PSO and that the pupil size measured at the first resting point of PSO is a more accurate pupil size measurement for the end of saccade than that measured at the highest peak of PSO.

3.3.1 Method

3.3.1.1 UKF application

A 2D UKF that incorporates eye muscle force, eyeball motion, and pupil motion was implemented by python with package filterpy (Labbe, 2018). We wrapped the UKF with a least square optimization algorithm to find the best fit of eyeball viscosity value. Our UKF was defined by the state vector **x**, the state translation matrix **F**, the measurement function **H**, the measurement noise matrix **R**, and the process noise covariance matrix **Q**. We define **x** as:

$$\mathbf{x} = [\, x_{pupil\_x},\ v_{pupil\_x},\ x_{eyeball\_x},\ v_{eyeball\_x},\ F_{muscle\_x},\ c_{muscle\_x},$$
$$x_{pupil\_y},\ v_{pupil\_y},\ x_{eyeball\_y},\ v_{eyeball\_y},\ F_{muscle\_y},\ c_{muscle\_y},]$$

where x_{pupil} and v_{pupil} is the location and velocity of the pupil; $x_{eyeball}$, $v_{eyeball}$ is the location and velocity of the eyeball, F_{muscle}, and c_{muscle} is the combined muscle force applied to the eyeball and the change of muscle force. The first six variables **x** is for the x axis and last six for y axis. Our eye movement model can be interpreted as a linear dynamic system that complies with the following Newtonian equations:

$$m_{pupil}*a_{pupil} = - k_p*(x_{pupil} - x_{eyeball}) – b_p*(v_{pupil} – v_{eyeball}) \quad \text{…. (3)}$$

$$m_{eyeball}*a_{eyeball} = F – b_e*v_{eyeball} \quad \text{…. (4)}$$

where m_{pupil} and $m_{eyeball}$ is the effective mass of pupil and eyeball, they were both set to 1 without losing generality of the model. The variable be is the viscosity of the eyeball. The variables a_{pupil} and $a_{eyeball}$ are the acceleration of pupil and eyeball, which are interpreted as the difference of v_{pupil} and $v_{eyeball}$ between the next time step and the current time step. To calculate the state transition matrix **F**, we first calculated the system matrix **A** of that summarises the Newtonian equations above:

$$A = \begin{bmatrix} 0 & 1 & 0 & 0 & 0 & 0 & 0 & 0 & 0 & 0 & 0 & 0 \\ -kp & -bp & kp & bp & 0 & 0 & 0 & 0 & 0 & 0 & 0 & 0 \\ 0 & 0 & 0 & 1 & 0 & 0 & 0 & 0 & 0 & 0 & 0 & 0 \\ 0 & 0 & 0 & -be & 1 & 0 & 0 & 0 & 0 & 0 & 0 & 0 \\ 0 & 0 & 0 & 0 & 0 & 1 & 0 & 0 & 0 & 0 & 0 & 0 \\ 0 & 0 & 0 & 0 & 0 & 0 & 0 & 0 & 0 & 0 & 0 & 0 \\ 0 & 0 & 0 & 0 & 0 & 0 & 0 & 1 & 0 & 0 & 0 & 0 \\ 0 & 0 & 0 & 0 & 0 & 0 & -kp & -bp & kp & bp & 0 & 0 \\ 0 & 0 & 0 & 0 & 0 & 0 & 0 & 0 & 0 & 1 & 0 & 0 \\ 0 & 0 & 0 & 0 & 0 & 0 & 0 & 0 & 0 & -be & 1 & 0 \\ 0 & 0 & 0 & 0 & 0 & 0 & 0 & 0 & 0 & 0 & 0 & 1 \\ 0 & 0 & 0 & 0 & 0 & 0 & 0 & 0 & 0 & 0 & 0 & 0 \end{bmatrix}$$

Because this linear dynamic system is time-invariant, we can calculate the state transition matrix by the equation $F(t, \Delta t) = e^{A*\Delta t}$. Since the input data has a frequency of 500Hz, $\Delta t = 2$(ms). Though what the eye tracker recorded is the pupil-CR change signal, here we assume the eye tracker recorded the pupil change signal, so we have the measurement function **H** defined as:

$$H = \begin{bmatrix} 1 & 0 & 0 & 0 & 0 & 0 & 0 & 0 & 0 & 0 & 0 & 0 \\ 0 & 0 & 0 & 0 & 0 & 0 & 1 & 0 & 0 & 0 & 0 & 0 \end{bmatrix}$$

The measurement noise matrix **R** is defined as:

$$R = \begin{bmatrix} 25 & 25 \\ 25 & 25 \end{bmatrix}$$

The process noise covariance matrix **Q** can be calculated by the integration of $\mathbf{FQ_cF}^T$ over Δt, where $\mathbf{Q_c}$ is set as:

$$Qc = \begin{bmatrix} 0 & 0 & 0 & 0 & 0 & 0 & 0 & 0 & 0 & 0 & 0 & 0 \\ Skp & Sbp & Skp & Sbp & 0 & 0 & 0 & 0 & 0 & 0 & 0 & 0 \\ 0 & 0 & 0 & 0 & 0 & 0 & 0 & 0 & 0 & 0 & 0 & 0 \\ 0 & 0 & 0 & 0 & 0 & 0 & 0 & 0 & 0 & 0 & 0 & 0 \\ 0 & 0 & 0 & 0 & 0 & 0 & 0 & 0 & 0 & 0 & 0 & 0 \\ 0 & 0 & 0 & 0 & 0 & Scm & 0 & 0 & 0 & 0 & 0 & Ccm \\ 0 & 0 & 0 & 0 & 0 & 0 & 0 & 0 & 0 & 0 & 0 & 0 \\ 0 & 0 & 0 & 0 & 0 & 0 & Skp & Sbp & Skp & Sbp & 0 & 0 \\ 0 & 0 & 0 & 0 & 0 & 0 & 0 & 0 & 0 & 0 & 0 & 0 \\ 0 & 0 & 0 & 0 & 0 & 0 & 0 & 0 & 0 & 0 & 0 & 0 \\ 0 & 0 & 0 & 0 & 0 & 0 & 0 & 0 & 0 & 0 & 0 & 0 \\ 0 & 0 & 0 & 0 & 0 & Ccm & 0 & 0 & 0 & 0 & 0 & Scm \end{bmatrix}$$

S_{kp}, S_{bp}, S_{cm} represent the standard deviation in k_p, b_p, and c_{muscle} and are assigned the values 0.1, 0.1, 0.25; C_{cm} is the covariance between c_{muscle} on x and y axis with the value of 0.1.

The UKF was applied to the raw trajectory data ((x, y) locations) with a time resolution of 2ms. From the five languages, we selected the English data only. Raw trajectory data were available for 30 English readers out of which 70% (21 subjects) were used in UKF filtering and analysis, leaving the remaining 30% as a dataset for possible validation and test in future research. During the filtering, if the filter encounters discontinuity in trajectory the filter will stop and initiate with new initial state vector and covariance matrix. The filter discomposes raw trajectory data into pupil displacement trajectory and eyeball trajectory. The eyeball trajectory was smoothed by forward-backward filtering (Gustafsson, 1996) implemented by the scipy.signal.filtfilt method with singal.butter set to 3, 0, and 3 (Jones et al, 2001).

3.3.1.2 Event detection

Three critical time points during PSO were identified: 1) the first PSO peak point when pupil displacement is the biggest and in the same direction as the saccade; 2) the first PSO resting point when pupil displacement first restores to zero after the first PSO peak point; 3) the second PSO resting point when pupil displacement restores to zero for the second time after the first PSO peak point. The first PSO peak point is the conventional division point between saccade end and fixation start (cf. Andersson,

Larsson, Holmqvist, Stridh & Nyström (2017). For the division between fixation end and saccade onset we applied the adaptive event detection algorithm by Nyström and Holmqvist, (2010) to filtered eyeball trajectories with pupil displacement constraint. If the pupil displacement within 10ms before detected saccade onset is bigger than 5 pixels (0.11 degrees), we did not ignore this saccade onset. The raw trajectories were sliced into saccade and fixation by saccade onset points and first PSO peak points. The time points of the first and second PSO resting point were marked during each fixation.

3.3.1.3 Analysis

The pupil sizes at these three time points were the targets of analysis in this experiment. We used the lme4 package (Bates, Maechler & Bolker, 2012) with R to conduct a mixed effects analysis to compare the pupil sizes at different phases of PSO. Note that without adding additional independent variables, the mixed effects analysis is equivalent to a one-way repeated measures ANOVA. We chose a mixed effects analysis because it allows the addition of other independent variables of interest (e.g., saccade length, age, which eye, saccade direction) while maintaining the same analysis of target variables. For fixed effects, we added PSO phase, age, saccade length, and eye (left or right) into the model; for random effects, we added intercepts for subjects. We used residual plots and Q-Q plots to check the linearity, homoscedasticity, and normality and found no obvious violation to these assumptions. Likelihood ratio tests were conducted between full model with the target effect and null model without the target effect to calculate p-values.

3.3.2 Results and Discussion

3.3.2.1 Event detection results

An example of the application of UKF to raw eye tracking data during saccade and fixation is shown in Figure 23a. We can easily identify the first PSO peak point, the first PSO resting point and second PSO resting point. We can see that the saccade onset defined by the filtered eyeball trajectory is 2–4 ms earlier than the saccade onset defined

by raw measurement data, but this small offset at the beginning of saccade does not affect our analysis in the PSO period.

As shown in Figure 23b, our UKF event detection algorithm is free of glissades. The proportion of small saccades (below 50ms) detected with our method is much smaller than that detected with the Eyelink II's default algorithm. While big PSOs may be

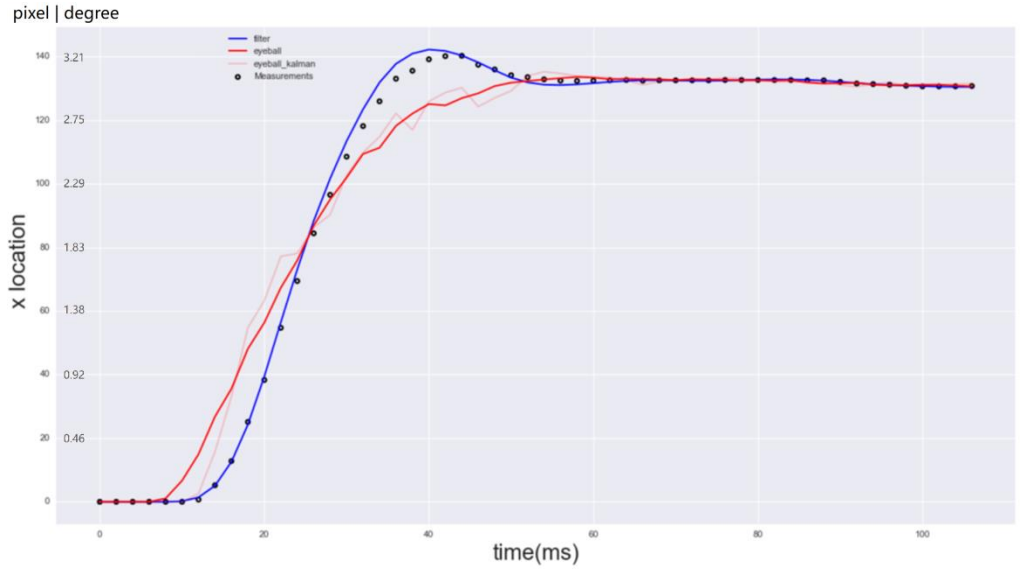

(a)

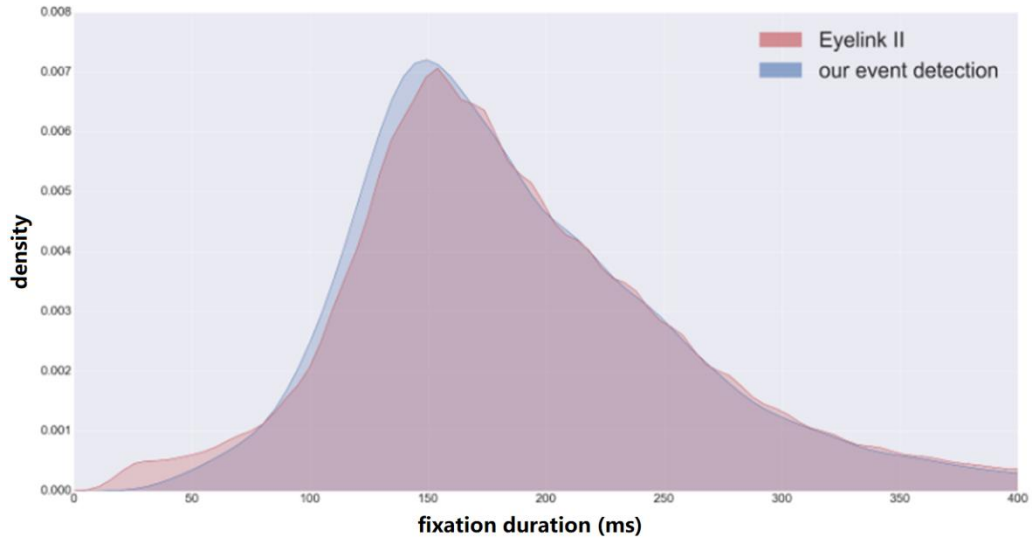

(b)

Fig. 23. (a) The application results of UKF to eye tracker output. Measurement is the raw gaze position; the filter outputs expected pupil trajectory and eyeball trajectory; the eyeball trajectory was then smoothed by forward-backward filtering. (b) Fixation duration distribution of Eyelink II event detection output and our UKF event detection output.

identified as small saccades (glissades) by the Eyelink II default algorithm, these PSOs were not marked as saccades by our method because of the big pupil displacement during PSOs. As a result of mistaking PSO for glissades, a saccade-to-fixation trajectory will be severed into two pairs of saccade and fixation: the former pair has a normal saccade and exceedingly small fixation duration; the latter pair has a small saccade (with a size of twice the amplitude of the PSO at the opposite direction to the true saccade) and normal fixation duration.

3.3.2.2 Pupil size change during PSO

The PSOs under analysis were split into two groups according to the direction and size of preceding saccades: rightward PSOs follow rightward saccades with saccade size 1 – 6 degrees; leftward PSOs follow leftward saccades with saccade size 1 – 6 degrees. Mean pupil sizes at different phases of PSO and pupil size changes between different phases of PSO are shown in Table 1. We can see that the pupil size change from the first PSO peak to first PSO resting point is bigger in absolute value and less variable than that from the first to the second PSO resting point. The former accounts for one quarter of the oscillation cycle while the latter accounts for half of the oscillation cycle. The direction for pupil size change differs between the two eyes and mirrors that between leftward and rightward saccade.

We constructed a linear mixed effects model of pupil size as a function of PSO phase (fixed effect) and saccade ID (random intercept) for left eye of leftward saccade (LL), right eye of leftward saccade (LR), left eye of rightward saccade (RL), and right eye of rightward saccade (RR), respectively. Results showed that there were significant differences of pupil size among different phases of PSO for LL ($F(2, 13224) = 50.1$, $p < 0.001$), LR ($F(2, 13224) = 246.3$, $p < 0.001$), RL($F(2, 61668) = 1174.1$, $p < 0.001$), and RR ($F(2, 61668) = 171.1$, $p < 0.001$). Analysis showed that all pupil size changes during the period when pupil moves from the first peak of PSO back to the first resting point were significant ($p < 0.001$). There was a contrast of the sign of pupil size change between the abducting and adducting eye when pupil was restored from the first peak of

PSO to the first resting point: for the abducting eye, pupil size decreases by -0.84 in LL and -0.55 in RR; for the adducting eye, pupil size increases by 1.79 in LR and 1.63 in RL.

Table 1. Mean pupil size measured by pupil area at different phases of PSO and mean pupil size changes during PSO

	Leftward saccade		**Rightward saccade**	
Pupil sizes (area)	Left eye	Right eye	Left eye	Right eye
1) First PSO peak point	1152.0 ± 326.4	1127.1 ± 315.8	1183.9 ± 314.5	1179.6 ± 319.7
2) First PSO resting point	1151.1 ± 326.4	1129.0 ± 316.2	1185.5 ± 314.7	1179.1 ± 320.3
3) Second PSO resting point	1151.5 ± 326.9	1128.6 ± 314.9	1185.0 ± 313.7	1178.9 ± 320.3
2) – 1)	-0.84 ± 4.27	1.79 ± 4.62	1.63 ± 4.09	-0.55 ± 4.32
3) – 2)	0.35 ± 6.38	-0.32 ± 7.09	-0.54 ± 5.99	-0.17 ± 7.17

The reasons for this contrast can be complicated. First, if we assume the shape of the pupil without forces applying to it is a circle, the pupil at the first PSO peak receives the biggest elastic force so it can be deformed and elliptical, hence reduced in pupil size as measured by pupil area. This pupil deformation and restoration affects pupil size with the same sign for both the abducting and adducting eye. On average, when the pupil was restored from the first PSO peak to the first resting point, pupil size increased by 0.47 for leftward saccades and 0.54 for rightward saccades. Second, the pupil projects to the camera through the cornea and hence receives distortion from its original shape and size. In the experiment that produced our data, the camera for the left eye is normally set at the left front of the eye, while the camera for the right eye is normally set at the right front of the eye. The distortion in pupil size caused by cornea refraction in our camera settings is in different direction for the abducting and adducting eyes. For example, if the saccade is rightward, for the left eye, pupil displaces to the right in iris and hence away from the

part of cornea through which it projects to the camera on the left. This deviation from cornea will reduce the size of its virtual image perceived by the camera, so pupil size projected to the camera will be reduced at the first peak of PSO and restored at the first PSO resting point. For the right eye, the pupil displaces to the right in the iris and hence is closer to the part of the cornea through which it projects to the camera on the right. This movement towards the cornea will enlarge the size of the virtual image of the pupil perceived by the camera, so the pupil size projected in the camera will be enlarged at the first peak of PSO and restored at the first PSO resting point. By removing the pupil deformation effect for both eyes, we have the pupil-cornea-camera refractory effect when the pupil is restored from the first PSO peak to the first resting point: for the abducting eye, pupil size changes by -1.32 in LL and -1.09 in RR; for the adducting eye, pupil size changes by 1.32 in LR and 1.09 in RL. Third, the eyeball movement can differ between the abducting and adducting eye at the end of saccade when the pupil-CR trajectory reaches its first PSO peak. For pupil-CR gaze trajectories, the movement of the eyeball changes the timing of PSO phases, the relative angle between pupil centre axis and the camera, the part of the cornea through which light from the pupil projects to the camera, etc. These all may affect the change of pupil size between the first PSO peak and the first PSO resting point.

In this study we demonstrated that, in our camera settings, pupil size decreases from the first PSO peak to the first PSO resting point for the abducting eye, while it increases for the adducting eye. While the causes for these changes are complicated, for the purpose of the current dissertation, we just need to make sure the timing of the first PSO resting point is reliable, so that we can remove the pupil size change and get a reliable measure of pupil size at the end of the saccade. In the next chapter, we will use the pupil size at saccade end to make a big improvement to pupil size correction across the screen. In the next section, we express our eye movement model in mathematical form and use a simulation to check how the timing of the first PSO resting point can be compromised by various variables.

3.4 Model based simulation for saccade and PSO

In this section we calculate the analytical solution to the eye model in Section 3.1 (as shown in Fig.14). In addition to the eye model, we added a tracking process to produce pupil-CR signal of the eye model. Then we demonstrated that the pupil-CR eye model can offer simple explanations to various effects regarding PSO amplitudes. Lastly, we showed that the pupil-CR trajectories and pupil trajectories do not differ at the timing of first PSO resting point. The results of the simulation suggest that the timing of the first PSO resting point obtained by UKF event detection in Section 3.3 is reliable for estimating the uncontaminated pupil size at saccade end.

3.4.1 Simulation for pupil-CR eye movement

The eye model in Section 3.1 can be summarised by equations (3) and (4) in Section 3.3:

$$m_{pupil}*a_{pupil} = - k_p*(x_{pupil} - x_{eyeball}) – b_p*(v_{pupil} – v_{eyeball}) \quad \text{…. (3)}$$

$$m_{eyeball}*a_{eyeball} = F – b_e*v_{eyeball} \quad \text{…. (4)}$$

To set the eye model into motion, we defined F as a piecewise function of time with six time intervals. The time intervals were based on the contraction and relaxation of the lateral rectus and medial rectus muscles. F(t) is defined as follows for a rightward saccade:

$$F(t) = \begin{cases} (t - t_{move})c_{move} & t_{start} \le t < t_{start} + tc_{move} \\ (-t + t_{start} + 2tc_{move})c_{move} & t_{start} + tc_{move} \le t < t_{start} + 2tc_{move} \\ 0 & t_{start} + 2tc_{move} \le t < t_{brake} \\ -(t - t_{brake})c_{brake} & t_{brake} \le t < t_{brake} + tc_{brake} \\ -(t - t_{brake} + 2tc_{brake})c_{brake} & t_{brake} + tc_{brake} \le t < t_{brake} + 2tc_{brake} \\ 0 & t_{brake} + 2tc_{brake} \le t \end{cases}$$

Figure 24 shows the definition of time intervals for a rightward saccade: in Phase I, the forwarding muscle starts to contract at t_{start} and the force of the forwarding muscle builds up at a constant rate c_{move} until the contraction period tc_{move} is finished; in Phase II the forwarding muscle starts to relax and the force decreases at a constant rate c_{move}

until it reaches zero; in Phase III no force is applied to the eyeball; in Phase IV, the braking muscle starts to contract at t_{break}, the force

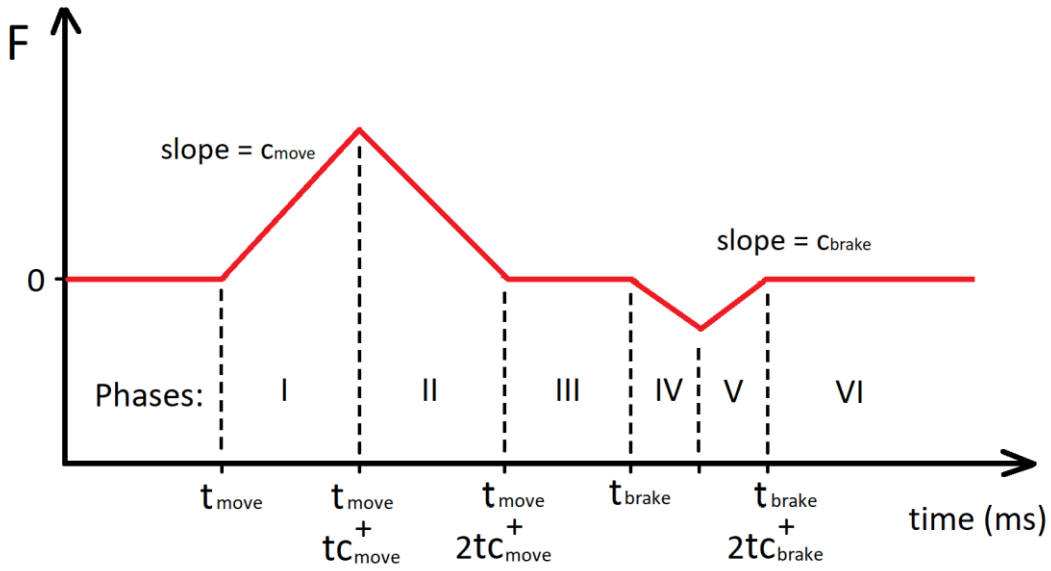

Fig. 24. F as a piecewise function of time divided into different phase of muscle activities.

of the braking muscle increases at a constant rate c_{brake} until the contraction period tc_{brake} is finished; then in Phase V the braking muscle starts to relax and the force decreases at a constant rate c_{break} until it reaches zero; in Phase VI no force is applied to the eyeball and the system evolves to the end of simulation.

The function for eyeball positions at each phase of eye movement is calculated by solving second order differential equations. The full function of the eyeball velocity and position is as follows:

$$Phase\ \ I \begin{cases} T = t - t_{start} \\ v_I(T) = -\frac{c_{move}}{b^2} + \frac{c_{move}}{b}T + \frac{c_{move}}{b^2}e^{-bT} \\ x_I(T) = -\frac{c_{move}}{b^2}T + \frac{c_{move}}{2b}T^2 - \frac{c_{move}}{b^3}e^{-bT} + \frac{c_{move}}{b^3} \end{cases}$$

$$Phase\ \ II \begin{cases} T = t - t_{start} - \ tc_{move} \\ v_{II}(T) = -\ \frac{c_{move}}{b}T\ + \left(-\frac{2c_{move}}{b^2} + \ \frac{c_{move}}{b^2}e^{-b\cdot tc_{move}}\right)e^{-bT} + \ \frac{c_{move}}{b}\left(\frac{1}{b} + \ tc_{move}\ \right) \\ x_{II}(T) = \ \frac{c_{move}}{b}\left(\frac{1}{b} + \ tc_{move}\ \right)T - \ \frac{c_{move}}{2b}T^2\ - \ \frac{1}{b}\left(-\frac{2c_{move}}{b^2} + \ \frac{c_{move}}{b^2}e^{-b\cdot tc_{move}}\right)e^{-bT} \\ \qquad + \ \frac{c_{move}}{b}\left(-\frac{1}{b^2} - \ \frac{1}{b}tc_{move} + \frac{1}{2}{tc_{move}}^2\right) \end{cases}$$

$$Phase\ \ III \begin{cases} T = t - t_{start} - \ tc_{move} \\ v_{III}(T) = \frac{c_{move}}{b^2}(e^{-b\cdot tc_{move}} - \ 1)^2 e^{-bT} \\ x_{III}(T) = \ \frac{c_{move}}{b}\left[-\frac{1}{b^2}(e^{-b\cdot tc_{move}} - \ 1)^2 \cdot e^{-bT} + \ {tc_{move}}^2\right] \end{cases}$$

$$Phase\ \ IV \begin{cases} v_{III}^{end} = \ v_{III}(t_{brake}\ - t_{start} - \ 2tc_{move}) \\ x_{III}^{end} = \ x_{III}(t_{brake}\ - t_{start} - \ 2tc_{move}) \\ T = t - t_{brake} \\ v_{IV}(T) = \frac{c_{brake}}{b}T\ + \left(\frac{c_{brake}}{b^2} + \ v_{III}^{end}\right)e^{-bT}\ - \ \frac{c_{brake}}{b^2} \\ x_{IV}(T) = -\frac{c_{brake}}{b^2}T + \ \frac{c_{brake}}{2b}T^2\ - \ \frac{1}{b}\left(\frac{c_{brake}}{b^2} + \ v_{III}^{end}\right)e^{-bT} \\ \qquad + \ \left(\frac{c_{brake}}{b^3} + \ \frac{v_{III}^{end}}{b} + \ x_{III}^{end}\right) \end{cases}$$

$$Phase\ V \begin{cases} T = t - t_{brake} - \ tc_{brake} \\ v_V(T) = \ -\frac{c_{brake}}{b}T + \left[-\frac{2c_{brake}}{b^2} + \ \left(\frac{c_{brake}}{b^2} + \ v_{III}^{end}\right)e^{-b\cdot tc_{brake}}\right]e^{-bT} + \frac{c_{brake}}{b}\left(\frac{1}{b} + \ tc_{brake}\right) \\ x_V(T) = \frac{c_{brake}}{b}\left(\frac{1}{b} + \ tc_{brake}\right)T\ + \frac{c_{brake}}{2b}T^2 - \frac{1}{b}\left[-\frac{2c_{brake}}{b^2} + \ \left(\frac{c_{brake}}{b^2} + \ v_{III}^{end}\right)e^{-b\cdot tc_{brake}}\right]e^{-bT} \\ \qquad + \ \frac{c_{brake}}{b}\left[-\frac{1}{b^2} - \frac{1}{b}tc_{brake} + \frac{1}{2}{tc_{brake}}^2\right] + \frac{1}{b}v_{III}^{end} + \ x_{III}^{end} \end{cases}$$

$$Phase\ \ VI \begin{cases} T = t - t_{start} - \ 2tc_{move} \\ v_{VI}(T) = \left[\frac{c_{brake}}{b^2}(e^{-b\cdot tc_{brake}} - \ 1)^2 + \ v_{III}^{end} \cdot e^{-2b\cdot tc_{brake}}\right]e^{-bT} \\ x_{VI}(T) = \ \frac{c_{brake}}{b}\left[-\frac{1}{b^2}(e^{-b\cdot tc_{brake}} - \ 1)^2 \cdot e^{-bT} + \ {tc_{brake}}^2\right] - \ \frac{1}{b}v_{III}^{end} \cdot e^{-2b\cdot tc_{brake}} \cdot e^{-bT} \\ \qquad + \ \frac{1}{b}v_{III}^{end} + \ x_{III}^{end} \end{cases}$$

where b stands for the eyeball viscosity b_e. Having obtained the analytical solutions for eyeball movement, we use step by step update (with a time resolution of 0.1ms) to apply

equation (2) in order to obtain the trajectory for the pupil. Then we use a variant of equation (2) in Section 3.2 to calculate pupil-CR trajectory:

pupil-CR trajectory = pupil trajectory –α* eyeball trajectory …. (5)

whereα(0 <=α< 1) as the proportion of CR saccade length against eyeball saccade length.

3.4.2. Model Parameters evaluation

Based on the parameters fitted to a left eye rightward saccade with saccade length 130 - 131 pixels (2.98 – 3.00 degrees) in Section 3.1, we set the values of current model parameters to be: t_{start} = 0, tc_{move} = 11, c_{move} = 0.05, b_e = 0.04, t_{brake} = 25, tc_{brake} = 3, c_{brake}=0.35, b_p = 0.14, k_p = 0.028, and α= 0.5. The simulated eyeball trajectory is shown in Fig.25a with six movement phases marked.

3.4.2.1 The necessity of pupil bracing at saccade onset

Since the frequency of PSO is estimated to be around 15 ~ 35 Hz (Tabernero & Artal, 2014; Punta et al., 2019), the corresponding pupil elasticity k_p should be around 0.009 ~ 0.048. In DPI or pupil-CR eye tracking data, there are small backshoots at saccade onset (Deubel & Bridgeman, 1995; Hooge et al., 2015; Hooge, Holmqvist, & Nyström, 2016). At saccade onset, P_4 reflection (reflection from the back of the lens for the DPI eye tracker) or pupil movement, due to their elasticity lags behind CR reflection (corneal reflection, moving with eyeball movement). As a result, both the P_4-CR signal (P_4 subtracted by CR) and pupil-CR signal (pupil subtracted by CR) shows a small movement opposite to the direction of saccade. The amplitude of pupil-CR backshoots is around 1 pixel (0.023 degrees; Hooge, Holmqvist, & Nyström, 2016). However, in our simulation, the backshoots are too big for k_p between 0.009 ~ 0.048 (as shown in Fig.25c). As k_p changes from 0.01 to 0.04, the backshoot amplitude ranges from 30 to 10 pixels (0.69 to 0.23 degrees). These backshoots cannot be reduced by increasing pupil viscosity b_p (as shown in Fig.25d). As k_p = 0.028 and b_p changes from 0.014 to 0.3, the backshoot amplitude reduces by half but is still too big. Also, as b_p changes from 0.1 to 0.3, the

backshoot amplitude does not decrease any further. The PSO is also unrealistically big as the pupil viscosity b_p reaches 0.1 or 0.3. These backshoots can be reduced by reducing the force of the forwarding muscle through the decrease of the contraction rate c_{move} (as shown in

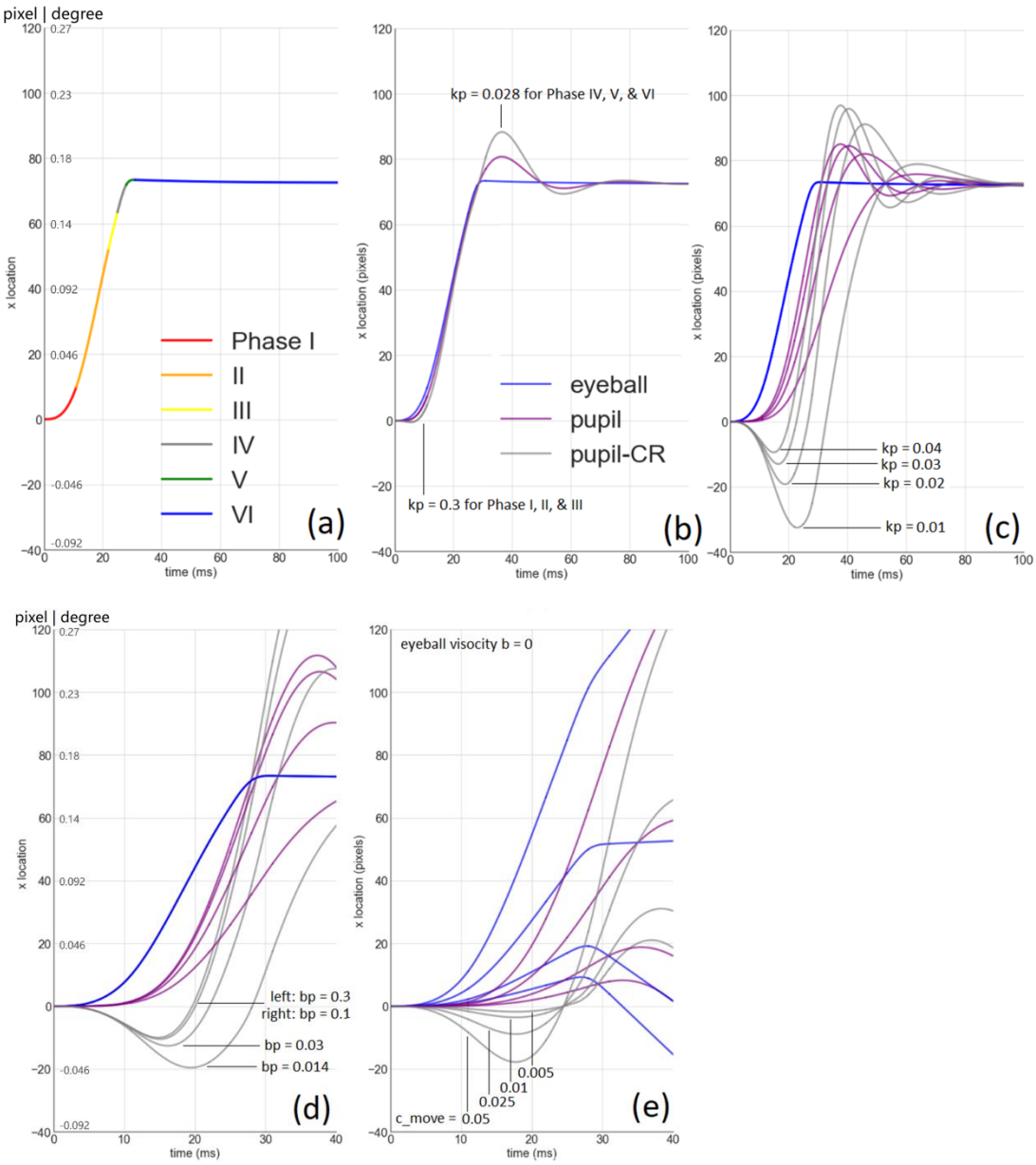

Fig. 25. The simulated trajectories of the eyeball, pupil, and pupil-CR. (a) The eyeball trajectory with six movement phases marked. (b) Eyeball, pupil, and pupil-CR and trajectories after pupil bracing is implemented at saccade onset. (c) The changes of backshoot amplitude as an effect of pupil elasticity. (d) The changes of backshoot amplitude caused as an effect of pupil viscosity. (e) The changes of backshoot amplitude caused as an effect of forwarding muscle force.

Fig.25e). But as c_{move} reduces from 0.05 to 0.005, the eyeball refuses to move much even when eyeball viscosity is set to zero. To solve the backshoot problem, we propose that the iris practices bracing at saccade onset by contracting the iris sphincter muscle and dilator muscle. As a result of bracing, the pupil elasticity at saccade onset is increased greatly so that the displacement of pupil from iris induced by eyeball acceleration is greatly reduced, hence the backshoot amplitude is reduced to that shown in experimental results (Tabernero & Artal, 2014, Hooge et al., 2015; Hooge, Holmqvist, & Nyström, 2016). The pupil bracing is implemented by increasing pupil viscosity to 0.3 at the beginning of the saccade (Phase I, II, & III). The eyeball, pupil, and pupil-CR trajectory with pupil bracing is shown in Fig.25b.

3.4.2.2 The amendment of pupil viscosity

In previous simulation studies, the pupil viscosity is estimated to be around 0.015 (Specht et al., 2017; Bouzat et al., 2018; Punta et al., 2019). This figure was fitted to data recorded by a pupil-CR eye tracker (Eyelink 1000 eye tracker) (Specht et al., 2017). As shown in Fig.25b, the pupil-CR signal produces PSO amplitude twice as large as the actual pupil displacement with an CR-to-eyeball ratio α of 0.5. Since the pupil-CR PSO has a similar oscillation cycle to pupil PSO (as shown below by simulation in Section 3.4.4), the pupil elasticity is relatively the same for pupil-CR signal and pupil signal. When we fit the eye model to the actual pupil displacement, as the pupil elasticity is relatively fixed by oscillation cycle, we should expect a different value in pupil viscosity to account for the reduced PSO amplitude. As we can see from Figure 26, PSO amplitude decreases as pupil viscosity increases for both pupil-CR and pupil signals. With pupil elasticity k_p set to 0.028, we can have a pupil PSO amplitude of 10 pixels (0.23 degrees) with pupil viscosity set to 0.1, while the pupil viscosity should be set to 0.2 to get a pupil-CR amplitude of 10 pixels (0.23 degrees). The PSO simulated in Fig.26 is larger than those in previous works (Bouzat et al., 2018; Punta et al., 2019), because the

braking of the eyeball at the end of the saccade is more abrupt than in the models in previous studies. In the next section we simulate how this abruptness of braking can explain the increase of PSO amplitude for older people and the difference in PSO amplitude between the two eyes.

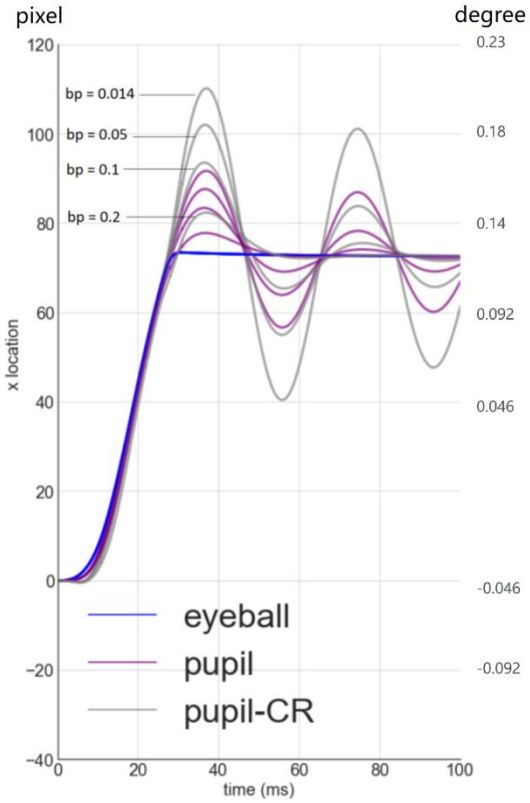

Fig.26. Pupil-CR PSO amplitude and pupil PSO amplitude as an effect of pupil viscosity b_p.

3.4.2.2 The role of braking

At the end of a saccade, the eyeball brakes and the pupil shoots forward and oscillates. We simulated the abruptness of the brake by reducing the braking time or braking muscle strength while keep other variables the same. Fig.27 shows that saccade length increases as we weaken the braking. We found that reducing the abruptness of braking causes the displacement of the pupil during PSO to change from 8 pixels (0.18 degrees; c_{brake} = -0.35, tc_{brake} = 3.0) to nearly 0 pixels (c_{brake} = -0.20, tc_{brake} = 3.0), while the corresponding pupil-CR PSO amplitude changes from 16 pixels (0.37 degrees) to nearly zero.

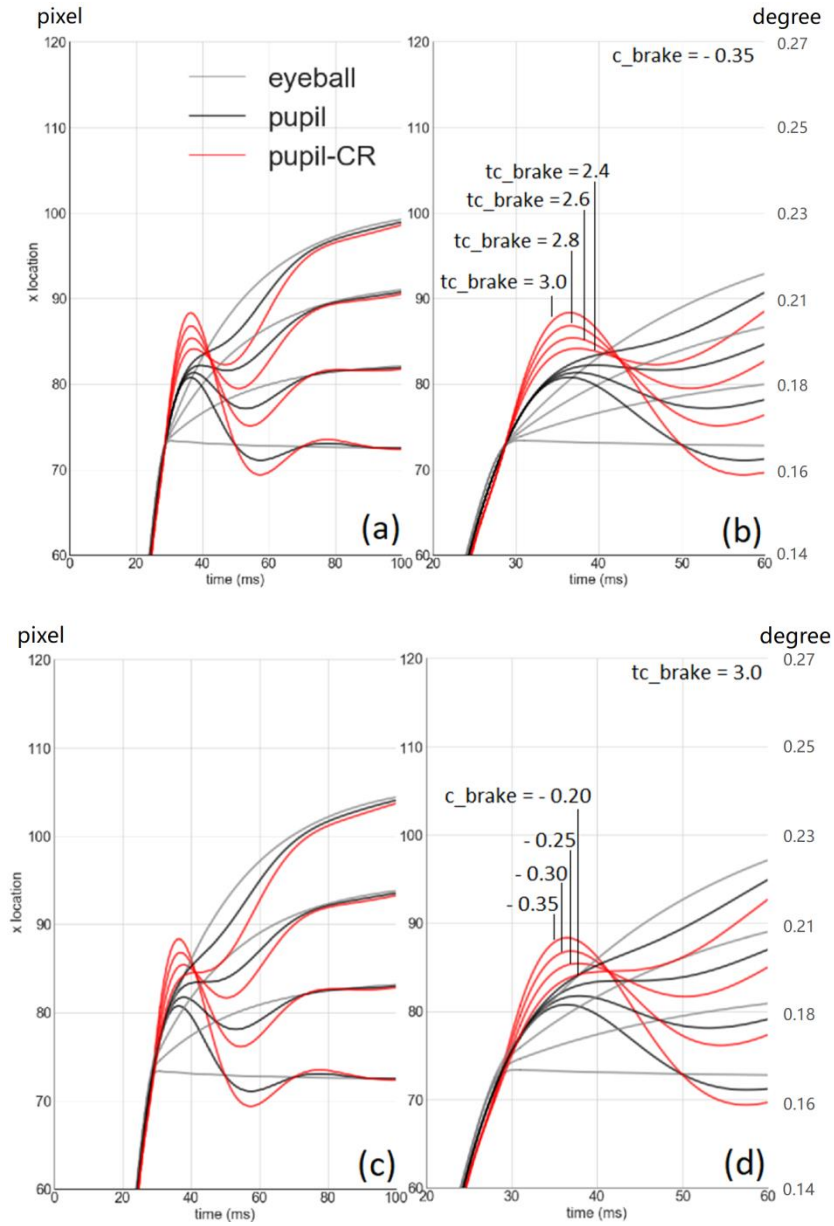

Fig.27. Eyeball, pupil, and pupil-CR trajectories during PSO for different abruptness of braking. (a) different abruptness simulated by reducing the duration of braking; (b) a zoom in for (a); (c) different abruptness simulated by reducing the strength of braking muscle force; (d) a zoom in for (c).

The abruptness of braking at the end may mediate various effects of PSO amplitude. First, in Section 3.2 we found that the adducting eye has a larger PSO amplitude than the adducting eye. This can be explained by the stronger lateral rectus muscle creating a more abrupt braking, hence a bigger PSO amplitude. Second, in Section 3.2 we found that older people have a larger PSO amplitude than younger people. The older people

may have less control of the braking muscle so that the braking may be more abrupt, hence creating larger PSO amplitude. Meanwhile, this increased PSO amplitude can also be explained by an increased CR-to-eyeball ratio α, as simulated in Section 3.4.3. Third, research showed that the PSO amplitude decreases as saccade length increases for large saccades (Hooge et al., 2015). This effect can be explained by a prolonged and less abrupt braking for larger saccades, dubbed the gentle braking hypothesis (Hooge et al., 2015).

3.4.3. Pupil and pupil-CR PSOs

As Formula (2) in Section 3.2 indicates, the pupil displacement will be magnified by a factor of 1/(1 –α):

pupil-CR trajectory/(1 –α) = eyeball trajectory + pupil displacement trajectory/(1 –α)

……..... (2)

We simulated the eyeball, pupil, and pupil-CR trajectory with the CR-to-pupil ratio α ranging from 0.5 to 0.8. As shown in Fig.28a, if the eyeball brakes abruptly and the pupil displacement at saccade end happens when the eyeball is relatively still, the pupil-CR PSO will oscillate at the same pace as the pupil PSO except with larger amplitude. If the eyeball movement has a softer brake and the pupil displacement at saccade end happens when the eyeball is still moving towards the target location, the shape of pupil-CR PSO becomes less predictable. As Fig.28b shows, when the pupil displacement is small and the eyeball is moving, the pupil trajectory and the pupil-CR trajectory with α = 0.5 shows only a dip in eyeball movement trajectory, while the pupil-CR trajectory α = 0.8 shows a salient PSO with decreasing frequency. If only the pupil-CR trajectory α = 0.8 were available to us, we would guess the eyeball trajectory is somewhere below the actual eyeball trajectory and the pupil oscillates around that trajectory with sizable amplitude; we would also overestimate the timing of the first PSO resting point from just below 40ms to above 40ms.

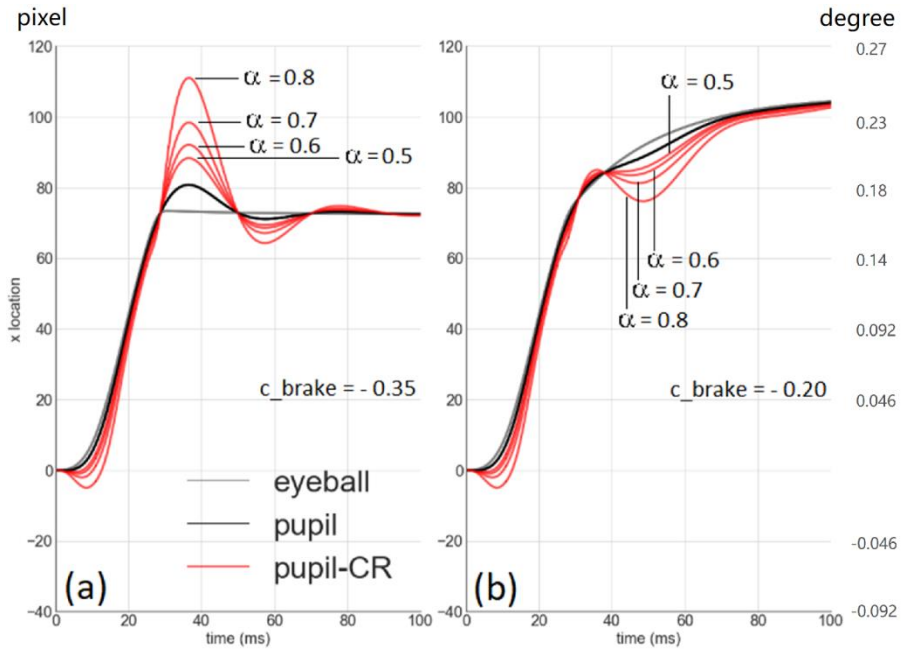

Fig. 28. Eyeball, pupil, and pupil-CR trajectories during PSO as an effect of CR-to-eyeball ratio. (a) with initial parameters when eyeball braking is abrupt; (b) with reduced braking force so that the eyeball braking is soft.

These simulation results suggest that, if the CR-to-eyeball ratio increase due to corneal bulge in older people, the older people will have bigger PSO amplitudes in pupil-CR trajectory, though the perceived pupil-CR PSO may not resemble the actual pupil PSO in shape.

Another finding is that, when the eyeball brakes less abruptly and the CR-to-eyeball ratio is big, the estimated timing of the first resting point pupil-CR PSO is later than the actual resting point of the pupil. In the next chapter, we will use the pupil size measured at the first resting point of pupil-CR PSO as a reliable pupil size measurement at saccade end. If the first resting point of the pupil-CR PSO does not coincide with the resting point of the actual pupil, then the pupil size we measured will be deformed by elastic force and corneal refraction due to pupil displacement. The error in resting time estimation here will not undermine the reliability of our pupil size measurement because 1) the size of resting time error is very small (about 5ms) even when pupil-to-CR ratio is very high (α= 0.8), so the resulting pupil measurement error should be negligible; 2) the resting error only happens when the eyeball braking is soft and the pupil displacement during soft braking

is very small in the first place, so the distortion in pupil size should be small when the time point we pick is not pupil resting point. We proceed to the next chapter with the knowledge that the pupil size measured at the first resting point of pupil-CR PSO is a reliable pupil size measurement at saccade end.

Chapter 4. Model based error correction for pupil size and fixation disparity

The main aim of this chapter is to investigate and correct the systematic errors in eye tracking. Three model-based studies were carried out to analyse the error in pupil

size measurement and fixation disparity. In Section 4.1 we improve the performance of pupil size correction across the page by a large margin. In Section 4.2, we use a geometric model of the head and the tracking procedure to offer an explanation for the long-standing fixation disparity problem. In Section 4.3, we use a ray tracing model and an empirical analysis to differentiate a new type of pupil artefact, the refraction pupil artefact, from the anatomical artefact.

4.1 Correction of pupil size across page

In this study, we estimated and corrected the pupil size error caused by the pupil foreshortening error (PFE) with a geometric model. We made a distinction between non-PFE pupil size error and PFE, hence we include both saccadic and fixational non-PFE pupil size error in our model. Our main hypothesis is that our model performs better than the first order linear model. Our secondary hypothesis is that the model with fixational non-PFE measured with pupil size at the first PSO resting point at fixation start performs better than the model with pupil size measured at the first PSO peak and the second PSO resting point.

4.1.1.1 Data

The outputs of UKF event detection in Section 4.3 were used for pupil size correction across each page of text. For each page, the fixations that start within the beginning 1500ms were removed. The pupil size at the beginning of the page often starts with a large pupil size and decreases quickly maybe due to the pupil reaction to the luminance change brought by the page change on the screen. In order to reduce the variance in the data that is unrelated to PFE, we removed the fixations that start within the beginning 1500ms of each page (84.5% of the data remained). For each fixation (starting from the first PSO peak to the onset of the next saccade), mean pupil size was calculated by averaging over all sample points within the fixation. Also, the pupil size at the first PSO peak, the first PSO resting point, and the second PSO resting point were recorded.

4.1.1.2 The Geometric Model

Following Hayes and Petrov (2014), we built a geometric model based on our experiment settings with the Eyelink II eye tracker. The PFEs were calculated by formula (5) modified from previous work (Mathur, Gehrmann, & Atchison, 2013):

$$PFE = \frac{Pupil\ size\ recorded\ at\ oblique\ angle\ \boldsymbol{\theta}}{Pupil\ size\ recorded\ at\ oblique\ angle\ 90^\circ} = 0.992 \times \cos((\boldsymbol{\theta} + 5.3)/1.121) \quad \ldots. \quad (5)$$

The correction for the difference between optical axis and pupil centre axis were removed from the formula by Mathur, Gehrmann and Atchison (2013) (PFE = 0.992 x cos((**θ** + 5.3)/1.121)), because we modelled pupil centre axis and the oblique angle already accounted for the difference between the optical axis and the pupil centre axis. The difference between the optical axis and the pupil centre axis were set to be -5.3°horizontally and -2.5°vertically for the left eye, 5.3°and -2.5°for the right eye (Mathur, Gehrmann, & Atchison, 2013; Aguirre, 2019).

As shown in Fig. 29, the model is described as a 3D Cartesian coordinate system with its origin located at the middle point between the centre of the two eyeballs. The distance between the two eyes (pupillary distance) was set to 64mm (Dodgson, 2004) and the radius of the eyeball was set to 12mm. The screen (1024 x 768 pixels) is 750mm away from the eyeball and the centre of the screen was set on the y axis. The experiment used a 22" Iiyama VisionMaster Pro 514 display where each pixel on the screen has a width of 0.24mm. For each fixation, firstly the pixel location on the screen was converted to (x, y, z) location in the Cartesian coordinates so that the direction of the optical axis is obtained; secondly, the pupil position was calculated based on the movement of the pupil centre axis; thirdly, the oblique angle is calculated between the pupil centre axis and the vector from the pupil centre to the camera; lastly the PFE is calculated by formula (5).

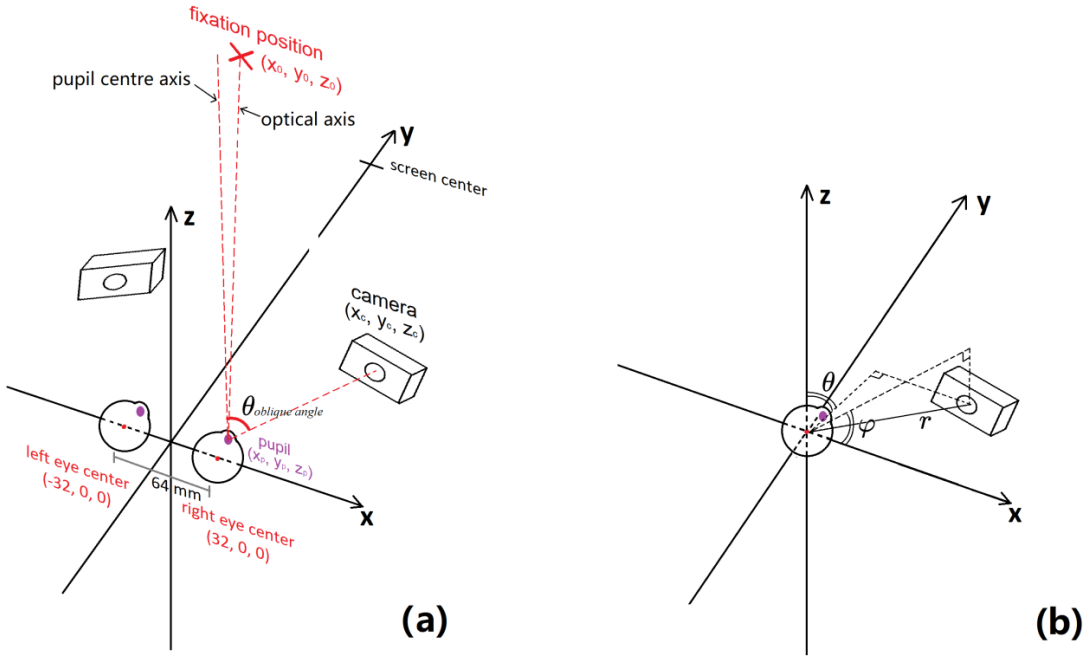

Fig. 29 (a) The geometric model of our experiment settings with the oblique angle illustrated for the right eye; (b) The conversion between the spherical coordinates and Cartesian coordinates for the relative position between eyeball and camera.

There are four critical differences between our model and the model by Hayes and Petrov (2001). 1) Our model is binocular so that common parameters that shared by both eyes can be evaluated once for both eyes, which reduces the number of total parameters if fixations from the two eyes are fitted separately. 2) Our model includes the pupil movement brought about by eyeball movements. Since in Eyelink II experiment settings, the distance between pupil and camera is quite small (around 60mm), the radius of the eyeball cannot be ignored during saccadic movements. 3) We used the PFE formula that can account for corneal refraction (Mathur, Gehrmann, & Atchison, 2013) as suggested by (Hayes & Petrov, 2014), because we are modelling the pupil size distortion of the human eye rather than an artificial eye. 4) Our pupil size measurement is in proportion to pupil area rather than pupil diameter. The PFEs calculated in our model can be used directly to correct pupil size data, while in the work of Hayes and Petrov (2014) the PFEs needed to be square rooted before their application to pupil size data.

4.1.1.4 Non-PFE changes in pupil size

Apart from PFE, the pupil size changes constantly due to luminance change, accommodation, cognitive load, etc.. The advantage of correcting pupil size in saccadic data in reading as opposed to in smooth pursuit data (Brisson et al., 2013) is that we can identify the pupil size changes that are not caused by PFE. During a saccade, the gaze position changes quickly and so PFE should explain the change of pupil size between saccade onset and offset; during fixations, the gaze position is relatively stable and the pupil size change during fixations are not caused PFE.

In the current model we included both the non-PFE change in saccade and fixation:

Pupil size error = PFE + fixational non-PFE error + saccadic non-PFEerror ….(6)

Fixational non-PFE error is all the pupil size change during fixation since we assume there is no PFE during fixations. The pupil size change during fixation is represented by the difference between pupil size at the start and end of fixation. We compared the performance of the model with three measurements of pupil size at fixation start: pupil size at the first PSO peak, the first PSO resting point, and the second PSO resting point. For saccadic non-PFE error we assume the non-PFE pupil size change within the saccade is a function of time with a constant rate of change.

4.1.1.3 Model fitting

There are 5 unknown parameters in our model, needing to be fitted to the data for pupil size correction: $a_{\text{pupil change rate}}$, $\theta_{\text{left camera}}$, $\varphi_{\text{left camera}}$, $\theta_{\text{right camera}}$, $\varphi_{\text{right camera}}$. The parameter $a_{\text{pupil change rate}}$ is the rate of pupil size change by accumulated saccadic time for each page. In our model, we assume the distance from the camera to the surface of the eyeball is fixed to 60mm, so the parameter $\theta_{\text{left camera}}$, $\varphi_{\text{left camera}}$ describes the left camera position for the left eye and the parameter $\theta_{\text{right camera}}$ and $\varphi_{\text{right camera}}$ for the right eye (as shown in Fig.29b).

The model parameters were fitted for each group of trials that shares the same calibration, because the experiment settings were subject to changes when participants were calibrated. The pupil size error for each calibration is defined by the average pupil size error of the pages after that calibration and before the next calibration. The pupil size

error of one page is defined as the sum of pupil size error for the left and right eye. The pupil size error of one page of one eye was defined by sum of variance of pupil sizes scaled by the average of pupil size across that page for that eye. The model fitting process used least squares optimization to find the model parameters that minimized pupil size error for each calibration.

In order to produce a set of parameters that avoids improbable experiment settings, we added a regulation term to the cost function for model fitting:

Cost = Pupil size error + λ x (- Experiment setting probability)

Where λ(0 <=λ<= 1) represents the strength of regulation; the experiment setting probability is calculated by a multivariate normal distribution of $\theta_{\text{left camera}}$, $\varphi_{\text{left camera}}$, $\theta_{\text{right camera}}$, and $\varphi_{\text{right camera}}$. The mean and covariance of this distribution is defined as:

$$Mean = \begin{bmatrix} 125° & 125° & 100° & 80° \end{bmatrix}$$

$$Cov = \begin{bmatrix} s^2 & 0.2s^2 & 0 & 0 \\ 0.2s^2 & s^2 & 0 & 0 \\ 0 & 0 & s^2 & 0.2s^2 \\ 0 & 0 & 0.2s^2 & s^2 \end{bmatrix}$$

The mean of $\theta_{\text{left camera}}$, $\varphi_{\text{left camera}}$, $\theta_{\text{right camera}}$, and $\varphi_{\text{right camera}}$ were set to 125, 125, 100, 80 degrees to mimic the Eyelink II experiment setting where the left camera is placed at the left-front-bottom of the eyeball and right camera at the right-front-bottom. As shown in the covariance matrix, the standard deviation of $\theta_{\text{left camera}}$, $\varphi_{\text{left camera}}$, $\theta_{\text{right camera}}$, and $\varphi_{\text{right camera}}$ were set to s (s = 10 degrees). We added correlations between $\theta_{\text{left camera}}$ and $\theta_{\text{right camera}}$ and between $\varphi_{\text{left camera}}$ and $\varphi_{\text{right camera}}$ to represent the observation that the relative position between the two Eyelink II cameras is relatively fixed.

4.1.1.4 Pupil size correction baselines

The performance of our model-based pupil correction was compared with several other methods. First, we conducted pupil size correction on our data by a first order linear model of (x, y) locations on the screen (Brisson et al., 2013):

Pupil size error = $b_0 + b_1X + b_2Y$ …. (M1)

Second, we conducted pupil size correction by second order model:

Pupil size error = $b_0 + b_1X + b_2Y + b_3X^2 + b_4Y^2$ …. (M2)

Third, we conducted pupil size correction by the geometric model only ($\theta_{\text{left camera}}$, $\varphi_{\text{left camera}}$, $\theta_{\text{right camera}}$, and $\varphi_{\text{right camera}}$), without fixational non-PFE error and saccadic non-PFE error:

Pupil size error = PFE …. (M3)

Fourth, we conducted pupil size correction with the geometric model and saccadic non-PFE error by fitting $\theta_{\text{left camera}}$, $\varphi_{\text{left camera}}$, $\theta_{\text{right camera}}$, $\varphi_{\text{right camera}}$, and $a_{\text{pupil change rate}}$:

Pupil size error = PFE + saccadic non-PFE error …. (M4)

Fifth, we conducted pupil size correction by adding parameter regularisation to method M4 with λ set to 0.02, 0.05, and 0.08:

Pupil size error = PFE + saccadic non-PFE error

+ λ x (- Experimentsetting probability) ….(M5)

Lastly, we added fixational non-PFE error into all the methods above. Since the fixational non-PFE error has three variants defined by the three different measurements of pupil size at fixation start (pupil size at the first PSO peak, the first PSO resting point, and the second PSO resting point), we added the three variants of fixational non-PFE error to all correction methods above separately.

4.1.2 Results and discussion

The results of pupil size correction are shown in Table 2. The first order linear model (M1) explained 0.350 of the total variance as a baseline. This is higher than the performance of M1 reported by Brisson et al. (2013) (0.132 for Tobii T120 eye tracker, 0.202 for Tobii X120, and 0.099 for EyeLink 1000). The increase of pupil size error explained by M1 may be due to the saccadic movements in reading data that increase the proportion of PFE as opposed to non-PEF pupil size error. While PFE can be captured by M1, non-PFE cannot.

Table. 2 The performance of pupil size correction methods measured by adjusted R^2.

Fixational Non-PFE types	Methods (adjusted R^2)						
	M1	M2	M3	M4	M5(λ =0.02)	M5(λ =0.05)	M5(λ =0.08)
Without fixational Non-PFE	0.350	0.423	0.307	0.366	0.390	0.385	0.378
First PSO peak	0.660	0.712	0.657	0.697	0.691	0.683	0.675
First PSO resting	0.674	0.724	0.678	0.704	0.699	0.691	0.680
Second PSO resting	0.670	0.715	0.672	0.692	0.687	0.683	0.672

We can see that our model (the geometric model with saccadic non-PFE and fixational non-PFE measured at the first PSO resting point) explained 0.704 of the overall variance in pupil size error after adjustment (AIC = -4798.9). This is twice as much as the baseline first order linear model (adjusted R^2 = 0.350, AIC = -4789.1). Our model is $1.79x10^4$ times as probable as the baseline model to minimize the information loss, which confirms our main hypothesis. The majority of the performance improvement was brought by incorporating the fixational non-PFE error. Among the variants of fixational non-PFE error, the one with fixation start pupil size measured at the first PSO resting point had the best performance. The performance of M4 with first PSO resting (adjusted R^2 = 0.704, AIC = 5096.1) is 9129.1 and $7.31x10^7$ times as probable as the model M4 with first PSO peak (adjusted R^2 = 0.697, AIC = 5087.0) and second PSO resting (adjusted R^2 = 0.692, AIC = 5078.0) to minimize the information loss. This confirms our secondary hypothesis.

Although the second order model (M2) that incorporates fixational non-PFE performed better than our method (M4), the performance improvement came at the cost of an increased number of parameters. For the pupil correction of binocular fixations, our model used 5 parameters as opposed to the 8 parameters in M2. Also, since our model is based on the geometric setting, the fitted parameters are meaningful values that describe

the experimental setting, while the parameters in M2 only describes the relationship between pupil size error and fixation location without explaining its causes. As result, we can use the fitted parameters in M4 for further investigation into the geometric errors in eye tracking data. For example, in Section 4.2 we studied how head movement is responsible for crossed fixation disparity for certain experiment settings; also, in Section 4.3 we show how camera position affects pupil artefact.

For the parameter regulation in M5, we see that as the regulation strength goes up, the performance of pupil error correction drops. Meanwhile, the distribution of parameters varies less as the regulation strength goes up as shown in Fig. 30. We took the pupil correction results of M5 with $\lambda = 0.05$ for later studies in Section 4.2 and 4.3 because it delivered pupil correction results and relatively realistic geometric settings for the experiment.

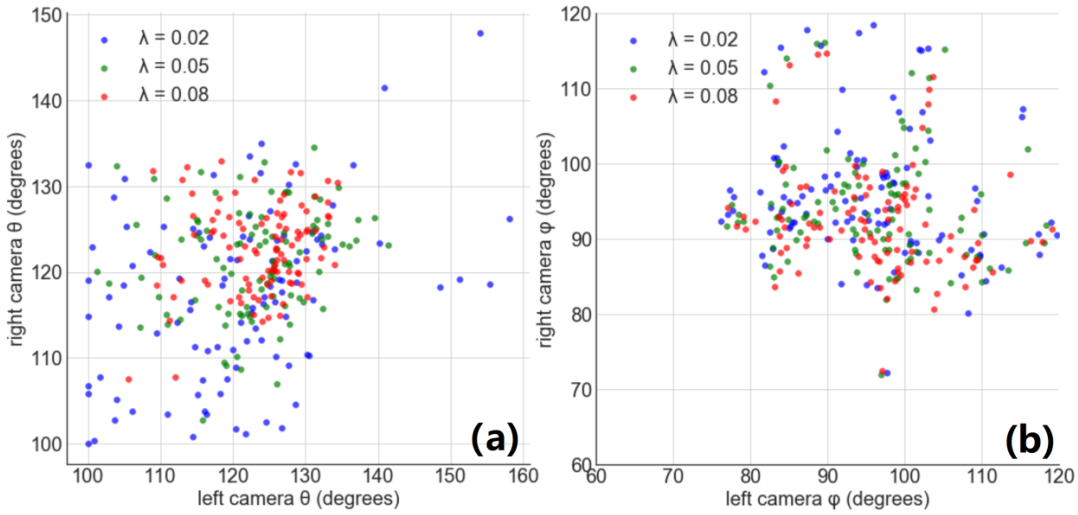

Figure. 30 The distribution of estimated camera position for each calibration. (a) The scatter plot of the relationship between estimated $\theta_{\text{left camera}}$ and $\theta_{\text{right camera}}$ for M5 with different parameter regulation strength. (b) The scatter plot of the relationship between estimated $\varphi_{\text{left camera}}$ and $\varphi_{\text{right camera}}$ for M5 with different parameter regulation strength.

In this study, we corrected the pupil size error caused by PFE with a geometric model. We took advantage of the saccade and fixation separation in reading data to parse out non-PFE pupil size error from PFE, and hence improved the performance of

the model. The corrected pupil size will be used below for estimating the refraction pupil artefact. The estimated camera positions will be used in Section 4.2 for fixation disparity correction, and also in Section 4.3.

4.2 Explaining the fixation disparity problem by head movement

The fixation disparity is mainly crossed for research groups using pupil-based eye trackers (Jainta, Hoormann, Kloke, & Jaschinski, 2010; Nuthmann & Kliegl, 2009; Shillcock, Roberts, Kreiner, & Obregon, 2010; Vernet & Kapoula, 2009). A pupil artefact explanation for this is that all these research groups somehow calibrated participants with low luminance and bigger pupil size and then let participants read with high luminance and smaller pupil size. This decrease of pupil size results in a pupil-size dependent artefact that generates crossed fixation disparities, while the real fixation positions remain aligned between the two eyes. In this study we propose a head movement explanation for the fixation disparity direction. We hypothesize that the head movement between the left and right eye calibrations causes the crossed fixation disparity.

4.2.1 Motivation

In an effort to align fixations to lines of text, we used a linear model ($y' = b_0 + b_1x + y$) to minimize the sum of squared vertical deviations of fixations to its nearest text line. The results produced the slope of horizontal deviation of fixations against horizontal location x for the left and right eye fixations, respectively. It turns out that, when scanning the text from left to right, the recorded left eye fixations often tilted downwards and the right eye fixations upwards. A typical trial is shown in Fig.31a with binocular fixations before and after linear model correction plotted on the text. We wondered whether this tilting (probably caused by head movement) had an effect on the recorded fixation disparity. The relationship between the fixation disparity and the slope difference between the two eyes for each calibration is shown in Fig. 31b (we excluded one third of the data that had large residuals during linear model correction).

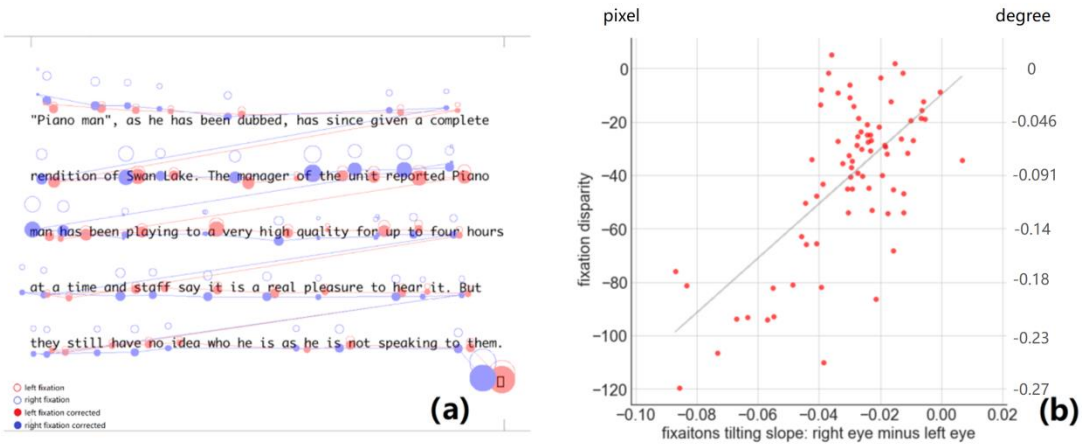

Figure 31. (a) The left and right fixations before and after correction plotted on the text. (b) The relationship between the fixation disparity and the slope difference between the two eyes for each calibration. Pearson's r = 0.66.

The strong correlation ($r = 0.66$, $p < 0.001$) between fixation disparity and the binocular difference of tilting confirmed our hypothesis that the head movement has an effect on fixation disparity. Moreover, as shown in Fig. 31b, the regression line of slope difference and fixation disparity nearly passed through the origin point (0, 0). This indicates that binocular difference in tilting may be fully responsible for the crossed fixation disparity; this means if there is no tilting difference, the fixation disparity should average at zero. We construct a geometric model to investigate and correct fixation disparity by reversing the effect of head movement during eye tracking.

4.2.2 Method

4.2.2.1 The geometric model

We constructed a geometric model to calculate the error in eye tracking brought about by the movement of the head. The model has three parts: a head model, an experiment setting model and a tracking model.

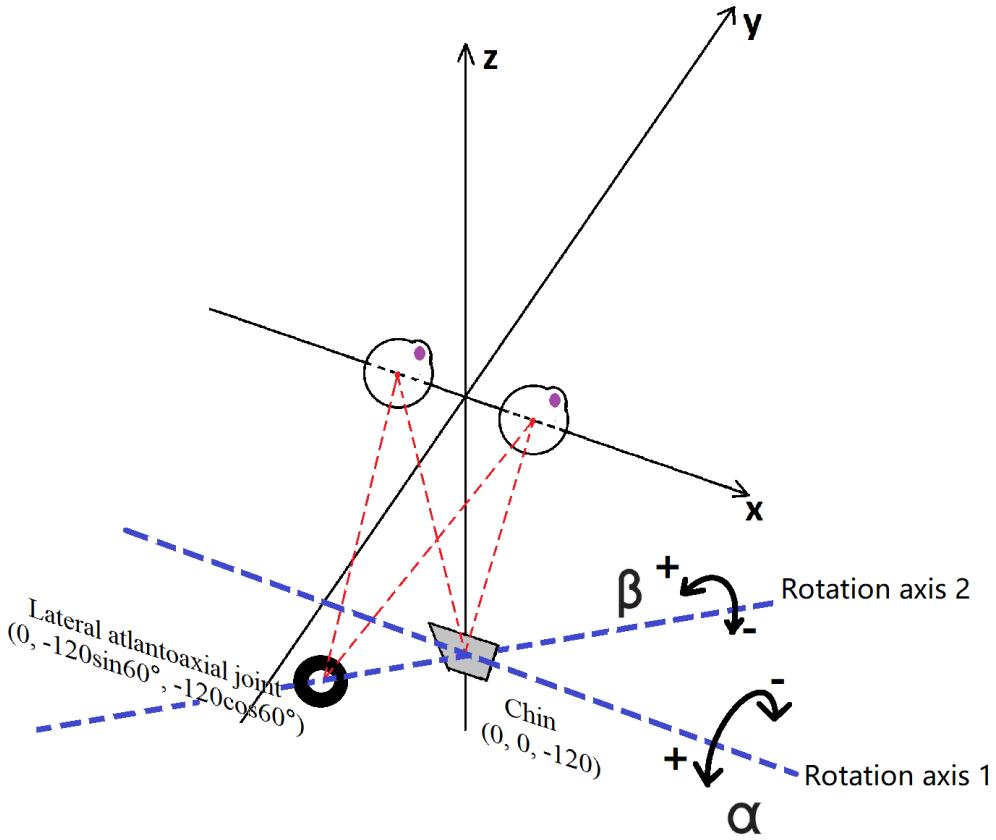

Fig. 32. The head model with the eyeballs, the chin, and lateral atlantoaxial joint. The wo rotation axes of the head model is shown in blue dotted lines.

As shown in Fig. 32, the head model consisted of the position of two eyes, the chin, and the lateral atlantoaxial joint. We set the distance between every two among the lateral atlantoaxial joint, the chin, and the middle point between the two eyeballs to be 120mm. As shown in Fig. 32b, the head model is allowed to move along two rotation axes: 1) the rotation axis that passes through the chin and parallel to the y axis, allowing the head to tilt forward and backward; 2) the rotation axis that passes through the lateral atlantoaxial joint and the chin, allowing the head to move left and right with the chin leaning on the chin rest. The angle of rotation around the chin axis is denoted as α and the angle of rotation around the chin-lateral atlantoaxial joint axis is denoted as β.
The experiment setting model is borrowed from the model in Chapter 4 that corrects pupil size error. The parameters of the left and right camera positions for each calibration were also estimated through the correction of PFE.

The tracking model represents a simplified version of the tracking process. First, the position of the pupil is projected to the film plane of the camera. The film plane of the camera is parallel to the y axis and the normal vector of the film plane points towards the eye. Second, a calibration algorithm is introduced to match the fixation position on screen to the pupil projection position on the film of the camera. For the calibration algorithm we chose the following formula:

Fixation position on screen = $a_0 + a_1X_{pf} + a_2Y_{pf} + a_3X_{pf}Y_{pf}$ …. (6)

The variables X_{pf}, Y_{pf} are the horizontal and vertical positions of pupil projection on the film of the camera. We chose this calibration formula because this formula is the one used with the Eyelink II eye tracker in gathering the data. During calibration, the parameters of Formula 6 are estimated. In the later tracking process, the pupil projection on the film will be interpreted into fixation position on screen through Formula 6. If the head does not move after calibration, the recorded fixation position will reflect the actual fixation position of the eye. If the head moves by changing α or β, the pupil projection position will change while the eye fixates at the same target on screen, also recorded fixation position will change.

4.2.2.2 Model fitting

We assume the deviation of the fixations from the text lines during reading is caused by head movement after calibration. The head movement parameterised by α and β was estimated by minimizing the tracking error in data for each eye. The tracking error was defined by the sum of squares of the Euclidian distance from each fixation to its nearest text line. The fixation positions were then corrected by reversing the error caused by head movement. The data we used are the same as in Section 4.1.1.1.

4.2.3 Results and discussion

The estimated value of α, rotation of the head around the chin axis, is averaged at -0.34 (SD = 0.61) for the left eye and -0.30 (SD = 0.51) for the right eye. The estimated value of β, rotation of the head around the chin-lateral atlantoaxial joint axis, is averaged at -0.94 (SD = 0.90) for the left eye and 0.71 (SD = 0.96) for the right eye.

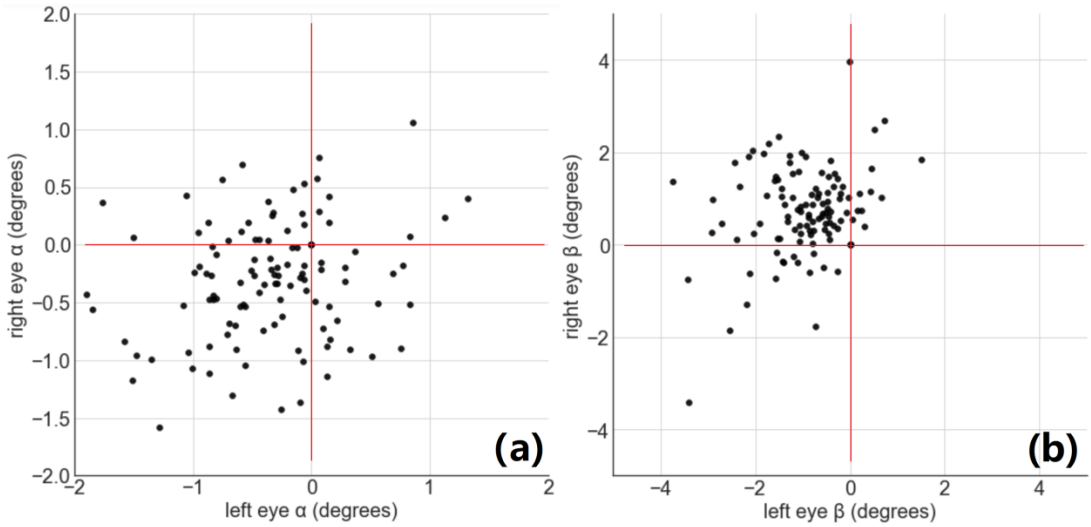

Fig. 33. The distribution of estimated head movement across calibrations along the two rotation axes for the left and right eye. (a) Rotation around the chin axis. (b) Rotation around the chin-lateral atlantoaxial joint axis.

The distributions of α and β across calibrations are shown in Fig. 33. We can see that, around the chin-lateral atlantoaxial joint axis, the left eye tends to rotate to the right after calibration and the right eye to rotate to the left. This difference in head movement between the two eyes creates crossed horizontal fixation disparity. The correction of these head movement produces fixations with near zero fixation disparity as shown in Fig. 34b. The average vertical fixation disparity is -1.70 (SD = 42.5) before correction and -1.69 (SD = 25.8) after correction; the average horizontal fixation disparity is -39.9 (SD = 30.1) before correction and 3.01 (SD = 19.7) after correction.

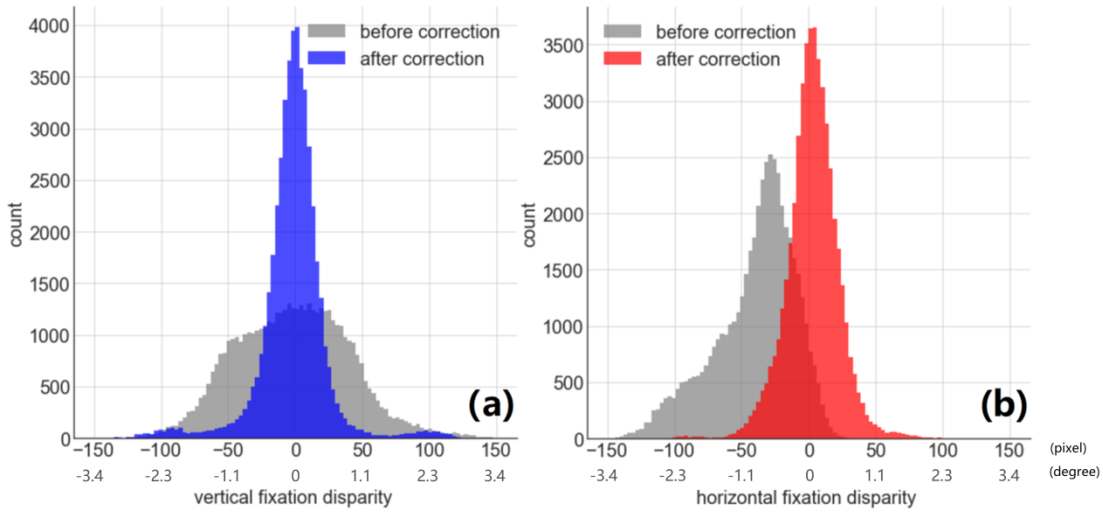

Fig. 34. The distribution of vertical and horizontal fixation disparities for fixation pairs before and after head movement correction.

Note that since we fitted the head model by minimizing the distance from fixations to text, it is natural that the corrected fixation of both eyes will come close to the lines of text and both the vertical and horizontal fixation disparity will reduce. This does not mean the reduction of horizontal fixation disparity by our model is trivial, because the fitting process would not succeed if our model were to predict uncrossed fixation disparity based on the tilting direction in our data. Our model shows how to link the tilting of fixation scanning path across the screen and horizontal fixation disparity as plotted in Fig. 31; the model explains the relationship by showing that a third variable, the head movement, causes both the tilting of fixation across the screen and fixation disparity. This explanation views the crossed fixation disparity as an artefact caused by head movement after calibration, as opposed to the pupil artefact explanation (Köpsel & Huckauf, 2017; Huckauf, 2018).

What causes the binocular difference in the head rotation around the chin-lateral atlantoaxial joint axis? Our proposal is that the procedure of monocular calibration causes this difference. During monocular calibration, firstly, the participants wear an eye patch to occlude the left (right) eye and calibrate the right (left) eye; secondly, the participants took off the eye patch from the left (right) eye and put it on the right (left) eye;

lastly, the participants calibrate the left (right) eye, then took off the eye patch from the right (left) eye. In the second step of putting on the eye patch to the right (left) eye, when the participant uses his/her hands to bring the eye patch closer to the right (left) eye from the front, the participant may rotate his/her head to the left (right) to bring the left eye closer to the hand. Then the participant may stay in that position and calibrate the left (right) eye. The rotation of the head after the calibration of one eye and before the calibration of the other eye results in the binocular difference in the head rotation, hence causing the deviation of average fixation disparity from zero. No matter which eye is first calibrated, the second step of monocular calibration described above will produce mainly crossed fixation disparities according to our model. In contrast, no head rotation is possible in the DPI eye-tracker, with its bite-bar.

4.3 Refraction pupil artefact

The pupil artefact is believed originate from the anatomy of the eye (Choe, Blake, & Lee, 2014; Drewes et al., 2014; Jaschinski, 2016; Hooge, Hessels, & Nyström, 2019). When the pupil dilates or contracts, the horizontal shift of pupil centre is reported to be about 0.05mm for every 1mm pupil size change (Yang, Thompson, & Burns, 2002; Drewes et al., 2014)(0.239°/mm to temporal direction when pupil enlarges, with an average eyeball radius of 12mm). When the pupil is at its maximum diameter, it is closest to the centre of the iris; when the pupil contracts, the centre of the pupil will move in the nasal and upward direction (Yang, Thompson, & Burns, 2002). The error in fixation position caused by the shift of pupil centre during pupil size change is referred as the pupil artefact in eye tracking.

However, in the study by Choe, Blake, and Lee (2014), while the left eye has a normal direction for the pupil artefact of -0.58°/mm, the pupil artefact for the right eye is in the opposite direction (-0.27°/mm) to what the anatomy of the pupil would predict. Since the camera in their study was placed about 15° to the left, we should consider whether the centre of the pupil image projected to the camera shifts with pupil size change.

In this study we show that this pupil artefact is a compound of anatomical pupil artefact and refraction pupil artefact. The light of pupil is refracted by the front and back of cornea before it projects to the tracking camera. The refraction pupil artefact refers to the shift of the pupil image centre in camera caused by corneal refraction when pupil size changes. The current study of refraction pupil artefact consists of two parts: a simulation study powered by a ray traced eye model; an empirical study supported by the pupil and fixation disparity correction in the previous sections.

4.3.1 Eye model simulation

To simulate the refraction pupil artefact, we used the ray traced eye model by Aguirre (2019) that provides the ellipse parameters of the pupil image as viewed by a camera at an arbitrary location. We set the camera to be angled -30°, -15°, 0°, 15°, 30° to the sagittal plane, with negative angle means to the left of the eye. The output images of the simulation is shown in Fig. 34a for pupil diameter ranges from 2 to 8 mm and camera angle at -30°, -15°, 0° (the images with camera angle -30°, -15° mirror those of -30°, -15°). The shifting of pupil centre of at different camera angle for pupil diameters ranging from 2 to 8 mm is shown in Fig. 34b. We can see that, when the

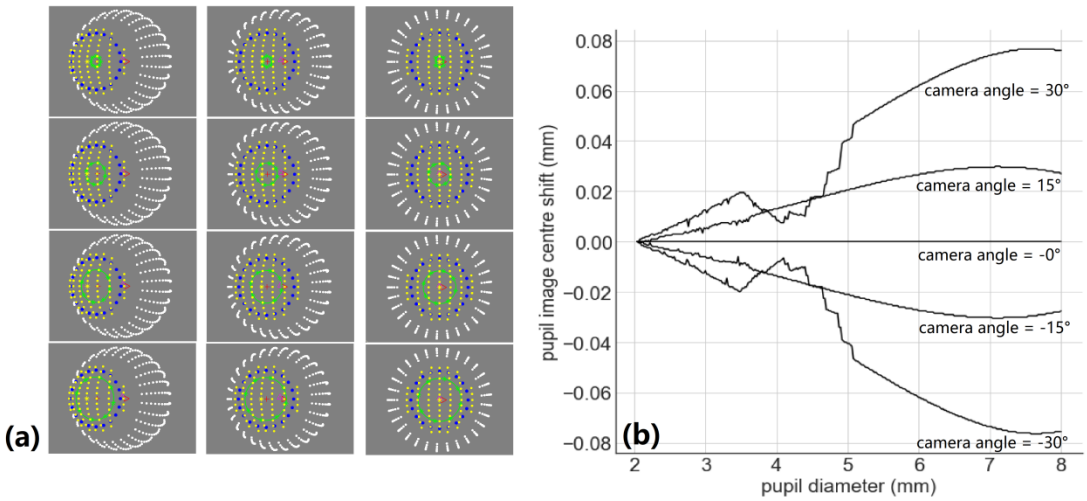

Fig. 34. (a) The output images of the ray traced simulation for pupil diameter ranges from 2 to 8mm and camera angle at -30°, -15°, 0°. The green ellipse is the pupil image projected to camera through corneal refraction. (b) The shifting of pupil image centre of at different camera angle for pupil diameters ranging from 2 to 8 mm with an interval of 0.01 mm (in practice the pupil diameter starts from 2.02 mm). The shifting of pupil image centre is compared to the 2.02 mm pupil.

camera is 15° to the left, the pupil image centre shifts to the right for about 0.007 mm (0.033°) per mm of pupil diameter change. This figure is 0.016 mm (0.076°)/mm when the camera is 30° to the left. The simulated pupil artefact is in the opposite direction with the pupil artefact reported by Choe, Blake, and Lee (2014), and much smaller. It seems that the refraction pupil artefact cannot explain why the right eye pupil artefact in their study is of the opposite direction of the anatomical pupil artefact.

4.3.2 Empirical evidence

To test the refraction pupil artefact in our reading data, we took three steps. First, the pupil size error for each page was corrected following the procedure in Section 4.1; second, the fixation position for each calibration was corrected following the procedure in Section 4.2; Third, we tested the relationship between fixation disparity and pupil size at different viewing angle of the camera. The viewing angle was estimated by the geometrical model in Section 4.1. In our experiment settings, the distance between the two eyes is 64 mm and subtends to 4.9° at the reading distance of 750mm. Along with the difference between pupil centre axis and optical axis for each eye (5.3°), the difference of camera view angle for the two eyes is about 15° if the two eyes are photographed by one camera. This difference in oblique angle with camera creates a difference in refraction pupil artefact in our two camera setting. According to the simulation in Section 4.3.1, if one camera is to the left of the left eye and the other to the right of the right eye, the left pupil image centre shifts to the right and the right pupil image centre shifts to the left (as pupil size increases); this decreases the value of fixation disparity when fixation disparity is defined as the right fixation position minus the left. We hypothesize that the increase magnitude of fixation disparity as pupil size increase (the positive correlation between fixation disparity and pupil size) will increase as cameras go from abduction side to adduction side). As we have two cameras in our experiment setting, we define the average abduction angle of camera as the average of the left eye viewing angle and the supplementary angle of the right eye view angle. If the average abduction angle is above 90°, the average position of the cameras are at the

abduction side of the eyes; if below 90°， the average position of the cameras are at the adduction side of the eyes.

The data was separated by the abduction viewing angle of (0°, 77.5°, 82.5°, 87.5°, 92.5°， 97.5°, 102.5°, 180°) and grouped in to seven bins. The relationship between fixation disparity and pupil size for each bin is shown in Fig. 35. The magnitude of pupil artefact is indicated by the regression line slope between fixation disparity and pupil size. The relationship between the magnitude of pupil artefact and camera view angle is shown in Fig. 36.

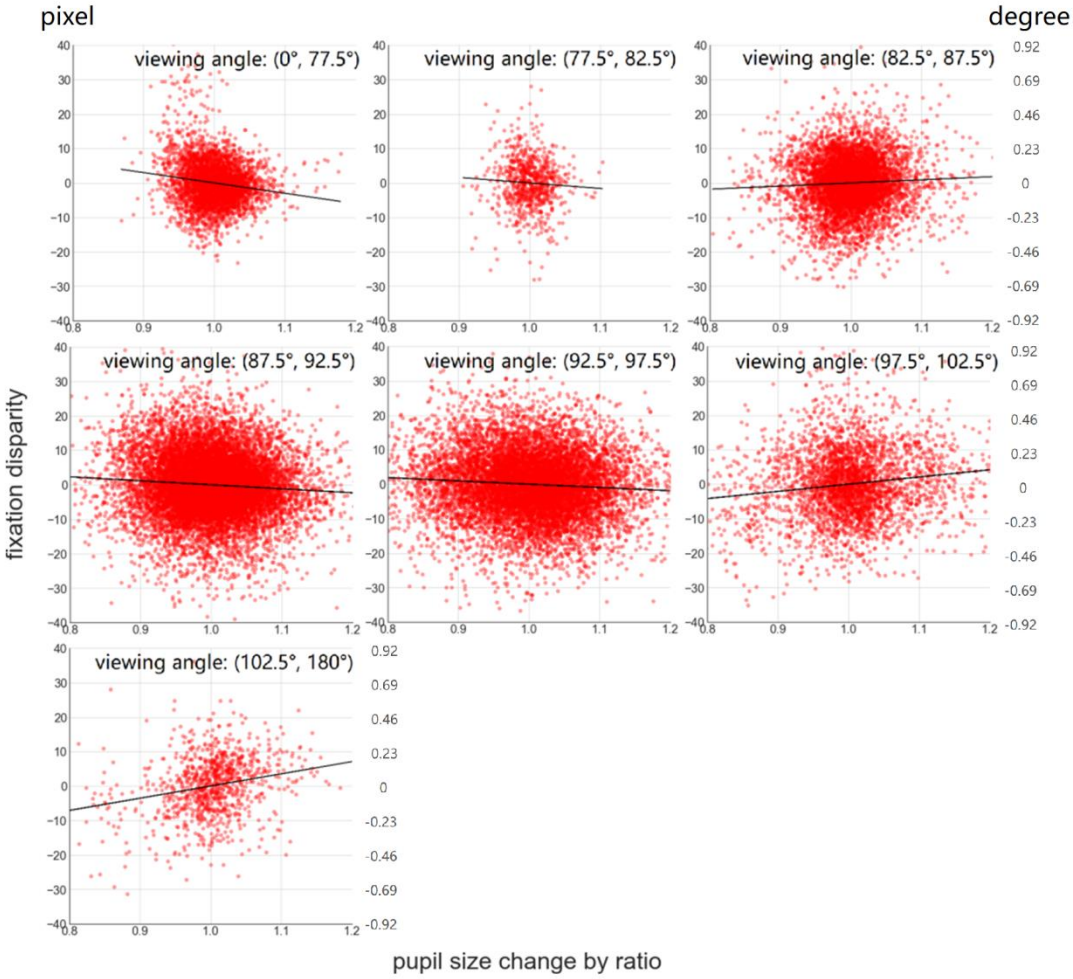

Fig. 35. The relationship between fixation disparity and pupil size for each bin of camera viewing angle.

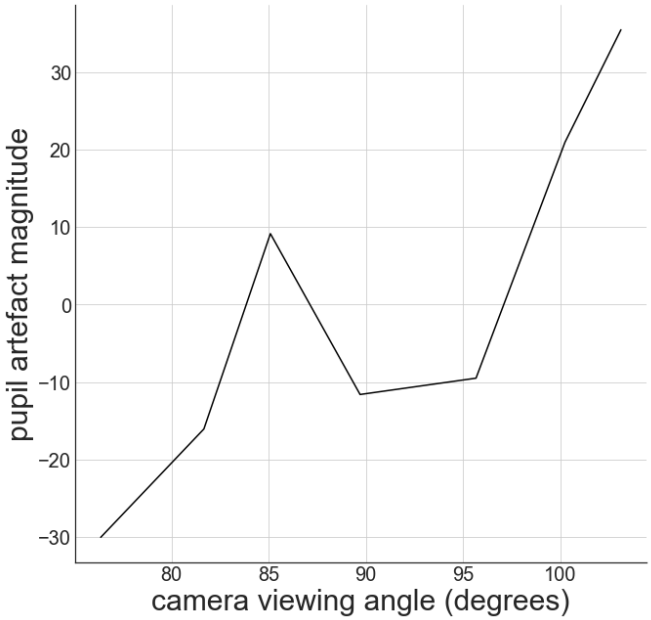

Figure 36. The relationship between the magnitude of pupil artefact and camera view angle.

As the camera moves from the adduction to abduction side of the eye, the slope of the regression line between fixation disparity and pupil size changes from -30.03 ($r = -0.15$, $p < 0.001$), to -16.06 ($r = -0.06$, $p = 0.10$), 9.14 ($r = 0.05$, $p < 0.001$), -11.61 ($r = -0.08$, $p < 0.001$), -9.50 ($r = -0.08$, $p < 0.001$), 20 ($r = 0.15$, $p < 0.001$), 35.44 ($r = 0.24$, $p < 0.001$). This rejects our hypothesis that the fixation disparity decreases with the increase of pupil size when the camera is to the abduction side of the eyes and increase when the camera is to the adduction side of the eyes. The results are quite to the contrary of our hypothesis. This casts doubts to the validity of the estimation of camera position in Section 4.1. Also, the correction of pupil size and fixation disparity by geometric models may introduce artefact effects between the estimated geometric parameters and pupil artefact on fixation disparity. Future work should be done to address this contradictory between simulation and empirical results.

The magnitude of the pupil artefact in our empirical data can be interpreted this way. First, we assume the average pupil diameter during reading is 3 mm; then the a pupil artefact slope of -30 can be translated into -10 pixels per mm change of pupil size; lastly, -10 pixels/mm at a reading distance of 750mm is equivalent to 0.23° /mm in optical

angle and -0.046mm/mm in pupil centre shifting. This means that, when the changes from 14° to the adduction side to 13° to the abduction side, the pupil artefact on fixation disparity changes from around -0.05 to 0.05 mm/mm.

5. Conclusions

In this thesis we explored and corrected the spatial and temporal errors in the process of eye tracking, by means of various geometric models. The main focus is on how the properties of the pupil mediate the generation and correction of errors. This thesis makes six main contributions.

First, we constructed a geometric model of the eyeball and deduced an analytic description of the eyeball, pupil, and pupil-CR trajectory during saccades and fixations; we used the model to explain the relationship between the properties of the PSO and other variables such as age, binocularity, saccade direction, pupil size deformation, and corneal bulge. We are the first to incorporate the forces of the muscles into the analytic solution of the eyeball trajectory, which allows us to have more control over the movement of the eyeball in simulations. We are also the first to incorporate pupil-CR processing into the eye-tracking model, which changes the estimated properties of pupil and eyeball dramatically. With the model, we estimate the pupil elastic factor, pupil viscosity, and the maximum PSO amplitude for both eyes of individuals. Our results match the findings of Mardanbegi et al. (2018) that oscillation amplitude increases with age, for which we hypothesise that the maximum PSO amplitude is higher in older people for both left and right eyes. We found that the pupil viscosity has a much higher value, around 0.2, when we take into consideration the pupil-CR process, as opposed to the pupil viscosity previously estimated to be around 0.015 (Bouzat et al., 2018; Punta et al., 2019; Specht et al., 2017). We proposed the mechanism of pupil bracing at saccade onset by contracting the iris sphincter muscle and dilator muscle to solve the problem of backshooting in pupil-CR eye tracking. As a result of bracing, the displacement of the pupil from the iris induced by eyeball acceleration is greatly reduced, hence the backshoot amplitude is reduced to that reported in experimental results (Hooge et al., 2015; Hooge, Holmqvist, & Nyström, 2016; Tabernero & Artal, 2014). By simulation we found that the abruptness of braking at the end of the saccade may mediate various effects of PSO amplitude. Firstly, the effect that the adducting eye has a larger PSO

amplitude than the adducting eye can be explained by the stronger lateral rectus muscle creating a more abrupt braking, hence a bigger PSO amplitude. Secondly, the effect that older people have a larger PSO amplitude than younger people can be explained by the less controlled and more abrupt saccade braking in older people. Meanwhile, simulations showed that this increase of PSO amplitude in older people can also be explained by an increased CR-to-eyeball ratio α. Lastly, the effect that the PSO amplitude decreases as saccade length increases for large saccades (Hooge et al., 2015) can also be explained by a prolonged and less abrupt braking for larger saccades.

Second, we constructed a novel event detection algorithm by incorporating our eye model into the Scaled Unscented Kalman filter. The algorithm is the first event detection algorithm to be able to detect boundaries and different phases of PSO. The algorithm is also able to make an informed correction to the glissade artefact created by the default Eyelink event detection algorithm. We found that pupil size at the first peak of PSO is smaller than pupil size at the following first resting point of PSO.

Third, we used a geometric model and the differentiation among PFE, saccadic non-PFE, and fixational non-PFE to improve the performance of pupil size correction across the page by a large margin. The process of pupil size correction confirmed that the pupil size measured at the first resting point of PSO is a more accurate pupil size measurement for the end of saccade than that measured at the highest peak of PSO. The process of pupil size correction also produced estimations of the camera positions during eye tracking.

Fourth, we offered a solution to the fixation disparity problem by analysing the effect of head movement during monocular calibration on the direction of fixation disparity, as opposed to the pupil artefact solution. We constructed a geometric model to calculate the error in eye tracking brought about by the movement of the head. By estimating head movement, we also aligned fixations to the text automatically, which counts as a model-based solution to the problem of automatic registration of fixations to their targets on the screen.

Fifth, we used a ray traced simulation to differentiate between anatomical pupil artefact and refraction pupil artefact. The simulation results show that the size of the refraction pupil artefact is about one-third the size of the anatomical pupil artefact at a camera viewing angle of 30°.

Sixth, the studies we carried out were based on reading data instead of data resulting from careful experimental control of the respective variables in question. We used geometric models to estimate the independent variable in question, such as camera position, PSO phases, and head movement. The advantage of this procedure is the generality of our method: the experimental procedure in this thesis can be applied to most eye tracking data with minimal modification. This essentially allows us to test our results on an unbounded data set. The disadvantage of this procedure is that the estimation of the parameters may be biased. If the estimated parameters are not carefully evaluated and tested, the biases may introduce artefacts that can be mistaken for real effects.

Further work should address the contradiction between the direction of the refraction pupil artefact found in ray traced simulation and in our empirical data. We need to examine the geometric models for pupil size and fixation disparity correction before we can trust the refraction pupil artefact in our data.

The current thesis explains the binocular difference in the shape of pupil-CR PSO by the abruptness of the braking at saccade offset. The right eye has less pupil oscillation than the left eye for rightward saccades because of the more abrupt braking brought about by the lateral rectus muscle. Due to the close temporal and spatial vicinity between the PSO of the pupil and the lens, we postulate that the lens also oscillates less for the right eye during rightward saccade offset, which gives the right eye an advantage in the stability of the image on the retina. In future work, we will test, when the saccade is rightward, whether the processing of the input to the right eye at the end of saccade (also the beginning of fixation) has an ocular prevalence type of advantage over that of the left eye.

References

Aguirre, G. K. (2019). A model of the entrance pupil of the human eye. *Scientific Reports*, *9*(1), 9360.

Andersson, R., Larsson, L., Holmqvist, K., Stridh, M., & Nyström, M. (2017). One algorithm to rule them all? An evaluation and discussion of ten eye movement event-detection algorithms. *Behavior Research Methods*, *49*(2), 616-637.

Atchison, D. A. (2006). Optical models for human myopic eyes. *Vision Research*, *46*(14), 2236-2250.

Barsingerhorn, A. D., Boonstra, F. N., & Goossens, H. H. L. M. (2017). Optics of the human cornea influence the accuracy of stereo eye-tracking methods: a simulation study. *Biomedical Optics Express*, *8*(2), 712-725.

Blythe, H. I., Liversedge, S. P., Joseph, H. S., White, S. J., Findlay, J. M., & Rayner, K. (2006). The binocular coordination of eye movements during reading in children and adults. *Vision Research*, *46*, 3898–3908.

Bouzat, S., Freije, M. L., Frapiccini, A. L., & Gasaneo, G. (2018). Inertial Movements of the Iris as the Origin of Postsaccadic Oscillations. *Physical Review Letters*, *120*(17), 178101.

Brisson, J., Mainville, M., Mailloux, D., Beaulieu, C., Serres, J., & Sirois, S. (2013). Pupil diameter measurement errors as a function of gaze direction in corneal reflection eyetrackers. *Behavior Research Methods*, *45*(4), 1322-1331.

Burr, D. C., Morrone, M. C., & Ross, J. (1994). Selective suppression of the magnocellular visual pathway during saccadic eye movements. *Nature*, *371*(6497), 511-513.

Camp, M. C., Wong, W. W., Filip, Z., Carter, C. S., & Gupta, S. C. (2011). A quantitative analysis of periorbital aging with three-dimensional surface imaging. *Journal of Plastic, Reconstructive & Aesthetic Surgery*, *64*(2), 148-154.

Chen, T., Chen, Y. F., Lin, C. H., & Tsai, T. T. (1998). Quantification analysis for saccadic eye movements. *Annals of Biomedical Engineering, 26(6)*, 1065-1071.

Choe, K. W., Blake, R., & Lee, S. H. (2016). Pupil size dynamics during fixation impact the accuracy and precision of video-based gaze estimation. *Vision Research*, *118*, 48-59, doi: 10.1016/j.visres.2014.12.018.

Clark, A. (1991). *Microcognition: Philosophy, cognitive science, and parallel distributed processing*. MIT Press.

Cohen, A. L. (2013). Software for the automatic correction of recorded eye fixation locations in reading experiments. *Behavior Research Methods*, *45*(3), 679-683.

Del Punta, J. A., Rodriguez, K. V., Gasaneo, G., & Bouzat, S. (2019). Models for saccadic motion and postsaccadic oscillations. *Physical Review E*, *99*(3), 032422.

Dennett, D. (1995). Artificial life as philosophy. *Artificial Life: an Overview*, 291-292.

Deubel, H., & Bridgeman, B. (1995). Perceptual consequences of ocular lens overshoot during saccadic eye movements. *Vision Research*, *35*(20), 2897-2902.

Diamond, M. R., Ross, J., & Morrone, M. C. (2000). Extraretinal control of saccadic suppression. *The Journal of Neuroscience*, *20*(9), 3449-3455.

Dodgson, N. A. (2004, May). Variation and extrema of human interpupillary distance. In *Stereoscopic Displays and Virtual Reality Systems XI* (Vol. 5291, pp. 36-46). International Society for Optics and Photonics.

Drewes, J., Zhu, W., Hu, Y., & Hu, X. (2014). Smaller is better: Drift in gaze measurements due to pupil dynamics. *PloS one*, *9*(10), e111197.

Elman, J. L., Bates, E. A., & Johnson, M. H. (1998). *Rethinking innateness: A connectionist perspective on development* (Vol. 10). MIT press.

Fedtke, C., Manns, F., & Ho, A. (2010). The entrance pupil of the human eye: a three-dimensional model as a function of viewing angle. *Optics Express*, *18*(21), 22364-22376

Fuhl, W., Santini, T., Kuebler, T., Castner, N., Rosenstiel, W., & Kasneci, E. (2018). Eye movement simulation and detector creation to reduce laborious parameter adjustments. *arXiv preprint arXiv:1804.00970*.

Gagl, B., Hawelka, S., & Hutzler, F. (2011). Systematic influence of gaze position on pupil size measurement: analysis and correction. *Behavior Research Methods*, *43*(4), 1171-1181.

Gajewski, D. A., and Henderson, J. M. (2005). The role of saccade targeting in the transsaccadic integration of object types and tokens. J. Exp. Psychol. 31, 820–830.

Gustafsson, F. (1996). Determining the initial states in forward-backward filtering. *IEEE Transactions on Signal Processing*, *44*(4), 988-992.

Hayes, T. R., & Petrov, A. A. (2016). Mapping and correcting the influence of gaze position on pupil size measurements. *Behavior Research Methods*, *48*(2), 510-527.

Henderson, J. M., and Hayes, T. R. (2017). Meaning-based guidance of attention in scenes as revealed by meaning maps. Nat. Hum. Behav. 1, 743–747.

Hendriks, A. W. (1996). Vergence eye movements during fixations in reading. *Acta Psychologica*, *92*, 131–151.

Holmqvist, K., Nyström, M., Andersson, R., Dewhurst, R., Jarodzka, H., & Van de Weijer, J. (2011). *Eye tracking: A comprehensive guide to methods and measures*. OUP Oxford.

Hooge, I. T., Hessels, R. S., & Nyström, M. (2019). Do pupil-based binocular video eye trackers reliably measure vergence?. *Vision Research*, *156*, 1-9.

Hooge, I., Holmqvist, K., & Nyström, M. (2016). The pupil is faster than the corneal reflection (CR): Are video based pupil-CR eye trackers suitable for studying detailed dynamics of eye movements?. *Vision Research*, *128*, 6-18.

Hooge, I. T., Niehorster, D. C., Nyström, M., Andersson, R., & Hessels, R. S. (2018). Is human classification by experienced untrained observers a gold standard in fixation detection?. *Behavior Research Methods*, *50*(5), 1864-1881.

Hooge, I., Nyström, M., Cornelissen, T., & Holmqvist, K. (2015). The art of braking: Post saccadic oscillations in the eye tracker signal decrease with increasing saccade size. *Vision Research*, *112*, 55-67.

Hsiao, Y. T., Shillcock, R., Obregón, M., Kreiner, H., Roberts, M. A., & McDonald, S. (2018). Differential vergence movements in reading Chinese and English: Greater fixation-initial binocular disparity is advantageous in reading the denser orthography. *The Quarterly Journal of Experimental Psychology*, *71*, 1: 324-332.

Huckauf, A. (2018). Systematic shifts of fixation disparity accompanying brightness changes. *Proceedings of the 2018 ACM Symposium on Eye Tracking Research & Applications (ETRA)* (pp. 1–5). vol. 37.

Ibbotson, M., & Krekelberg, B. (2011). Visual perception and saccadic eye movements. *Current Opinion in Neurobiology*, *21*(4), 553-558.

Jainta, S., Hoormann, J., Kloke, W. B., & Jaschinski, W. (2010). Binocularity during reading fixations: Properties of the minimum fixation disparity. *Vision Research*, *50*(18), 1775–1785.

Jainta, S., Vernet, M., Yang, Q., & Kapoula, Z. (2011). The pupil reflects motor preparation for saccades-even before the eye starts to move. *Frontiers in Human Neuroscience*, *5*, 97.

Jaschinski, W. (2016). Pupil size affects measures of eye position in video eye tracking: implications for recording vergence accuracy. *Journal of Eye Movement Research*, *9*(4).

Jones E, Oliphant E, Peterson P, *et al.* SciPy: Open Source Scientific Tools for Python, 2001-, http://www.scipy.org/ [Online; accessed 2019-10-22].

Julier, S. J. (2002, May). The scaled unscented transformation. In *Proceedings of the 2002 American Control Conference (IEEE Cat. No. CH37301)* (Vol. 6, pp. 4555-4559). IEEE.

Juhasz, B. J., Liversedge, S. P., White, S. J., & Rayner, K. (2006). Binocular coordination of the eyes during reading: Word frequency and case alternation affect fixation duration but not fixation disparity. *Quarterly Journal of Experimental Psychology*, *59*, 1614–1625.

Kimmel, D. L., Mammo, D., & Newsome, W. T. (2012). Tracking the eye non-invasively: simultaneous comparison of the scleral search coil and optical tracking techniques in the macaque monkey. *Frontiers in Behavioral Neuroscience*, *6*, 49.

Kirkby, J. A., Blythe, H. I., Drieghe, D., Benson, V., & Liversedge, S. P. (2013). Investigating eye movement acquisition and analysis technologies as a causal factor in differential prevalence of crossed and uncrossed fixation disparity during reading and dot scanning. *Behavior Research Methods*, *45,* 664–678.

Komogortsev, O. V., & Khan, J. I. (2008, March). Eye movement prediction by julieran filter with integrated linear horizontal oculomotor plant mechanical model.

In *Proceedings of the 2008 symposium on Eye tracking research & applications* (pp. 229-236). ACM.

Köpsel, A., & Huckauf, A. (2017). Binocular coordination in reading when changing background brightness. *Proceedings of the Latvian Academy of Sciences*. *Section B*, *71*(5), 359–365.

Krueger, L. E. (1989). Reconciling Fechner and Stevens: Toward a unified psychophysical law. *Behavioral and Brain Sciences*, *12*(2), 251-267.

Labbe, R. R. (2018). FilterPy Documentation.

Larsson, L., Nyström, M., & Stridh, M. (2013). Detection of saccades and postsaccadic oscillations in the presence of smooth pursuit. *IEEE Transactions on Biomedical Engineering*, *60*(9), 2484-2493.

Lee, J., & Lee, C. (2008). Changes in orientation discrimination at the time of saccadic eye movements. *Vision Research*, *48*(21), 2213-2223.

Lee, J. G., Han, J., & Li, X. (2008, April). Trajectory outlier detection: A partition-and-detect framework. In *2008 IEEE 24th International Conference on Data Engineering* (pp. 140-149). IEEE.

Liversedge, S. P., White, S. J., Findlay, J. M., & Rayner, K. (2006). Binocular coordination of eye movements during reading. *Vision Research*, *46*, 2363–2374.

Mathur, A., Gehrmann, J., & Atchison, D. A. (2013). Pupil shape as viewed along the horizontal visual field. *Journal of Vision*, *13*(6), 3-3.

McClelland, J. L. (2009). The place of modeling in cognitive science. *Topics in Cognitive Science*, *1*(1), 11-38.

Olivia E. Linden, Jun Kit He, Clinton S. Morrison, Stephen R. Sullivan, Helena O. B. Taylor. The Relationship between Age and Facial Asymmetry. *Plastic and Reconstructive Surgery*, 2018; 142 (5): 1145

Mackensen, G. (1958). Die Geschwindigkeit horizontaler Blickbewegungen. *Graefe.s Arch. fur Ophthal*. *160*, 47-64.

Mardanbegi, D., Killick, R., Xia, B., Wilcockson, T., Gellersen, H., Sawyer, P., & Crawford, T. J. (2018). Effect of aging on post-saccadic oscillations. *Vision Research*, *143*, 1-8.

Mathur, A., Gehrmann, J., & Atchison, D. A. (2013). Pupil shape as viewed along the horizontal visual field. *Journal of Vision*, *13*(6), 3-3.

Maybeck, P. S. (1982). *Stochastic models, estimation, and control* (Vol. 3). Academic press.

Navarro, R. (2014). Adaptive model of the aging emmetropic eye and its changes with accommodation. *Journal of Vision*, *14*(13), 21-21.

Nuthmann, A., & Kliegl, R. (2009). An examination of binocular reading fixations based on sentence corpus data. *Journal of Vision*, *9*, 1–28.

Nyström, M., & Holmqvist, K. (2010). An adaptive algorithm for fixation, saccade, and glissade detection in eyetracking data. *Behavior Research Methods*, *42*(1), 188-204.

Nyström, M., Andersson, R., Magnusson, M., Pansell, T., & Hooge, I. (2015). The influence of crystalline lens accommodation on post-saccadic oscillations in pupil-based eye trackers. *Vision Research*, *107*, 1-14.

Nyström, M., Hooge, I., & Holmqvist, K. (2013). Post-saccadic oscillations in eye movement data recorded with pupil-based eye trackers reflect motion of the pupil inside the iris. *Vision Research*, *92*, 59-66.

Ostry, D. J., & Feldman, A. G. (2003). A critical evaluation of the force control hypothesis in motor control. *Experimental Brain Research*, *153*(3), 275-288.

Penke, L., Bates, T. C., Gow, A. J., Pattie, A., Starr, J. M., Jones, B. C., ... & Deary, I. J. (2009). Symmetric faces are a sign of successful cognitive aging. *Evolution and Human Behavior*, *30*(6), 429-437.

Del Punta, J. A., Rodriguez, K. V., Gasaneo, G., & Bouzat, S. (2019). Models for saccadic motion and postsaccadic oscillations. *Physical Review E*, *99*(3), 032422.

Robinson, D. A. (1964). The mechanics of human saccadic eye movement.*The Journal of Physiology*, *174*(2), 245.

Robinson, D. A., O'meara, D. M., Scott, A. B., & Collins, C. C. (1969). Mechanical components of human eye movements. *Journal of Applied Physiology*, *26*(5), 548-553.

Rosengren, W., Nyström, M., Hammar, B., & Stridh, M. (2019). A robust method for calibration of eye tracking data recorded during nystagmus. *Behavior research methods*, 1-15.

Ryle, J. P., Vohnsen, B., & Sheridan, J. T. (2015). Simultaneous drift, microsaccades, and ocular microtremor measurement from a single noncontact far-field optical sensor. *Journal of Biomedical Optics*, *20*(2), 027004.

Salthouse, T. A. (2009). When does age-related cognitive decline begin? *Neurobiology of Aging*, *30*(4), 507-514.

Schütz, A. C., Braun, D. I., & Gegenfurtner, K. R. (2009). Object recognition during foveating eye movements. *Vision Research*, *49*(18), 2241-2253.

Shillcock, R. (*in press*). A modern materialist approach to abstraction, concreteness and explanation in cognition. Commentary on Gilead, Trope & Liberman. *Behavioral and Brain Sciences*.

Shillcock, R., Roberts, M., Kreiner, H., & Obregon, M. (2010). Binocular foveation in reading. *Attention, Perception, & Psychophysics*, *72*, 2184–2203.

Specht, J. I., Dimieri, L., Urdapilleta, E., & Gasaneo, G. (2017). Minimal dynamical description of eye movements. *The European Physical Journal B*, *90*(2), 25.

Stampe, D. M. (1993). Heuristic filtering and reliable calibration methods for video-based pupil-tracking systems. *Behavior Research Methods, Instruments, & Computers*, *25*(2), 137-142.

Suzuki, M., Shiller, D. M., Gribble, P. L., & Ostry, D. J. (2001). Relationship between cocontraction, movement kinematics and phasic muscle activity in single-joint arm movement. *Experimental Brain Research*, *140*(2), 171-181.

Švede, A., Treija, E., Jaschinski, W., & Krūmiņa, G. (2015). Monocular versus binocular calibrations in evaluating fixation disparity with a video-based eye-tracker. *Perception*, *44*(8-9), 1110-1128.

Sveikata, K., Balciuniene, I., & Tutkuviene, J. (2011). Factors influencing face aging. Literature review. *Stomatologija*, *13*(4), 113-116.

Tabernero, J., & Artal, P. (2014). Lens oscillations in the human eye. Implications for post-saccadic suppression of vision. *PloS one*, *9*(4), e95764.

Teichert, T., Klingenhoefer, S., Wachtler, T., & Bremmer, F. (2008). Depth perception during saccades. *Journal of Vision*, *8*(14), 27-27.

Valverde, G., & Terzija, V. (2011). Unscented Kalman filter for power system dynamic state estimation. *IET generation, transmission & distribution*, *5*(1), 29-37.

Vernet, M., & Kapoula, Z. (2009). Binocular motor coordination during saccades and fixations while reading: A magnitude and time analysis. *Journal of Vision*, *9*(7), 1–13.

Võ, M. H., and Wolfe, J. M. (2013). The interplay of episodic and semantic memory in guiding repeated search in scenes. Cognition 126, 198–212.

Wan, E. A., & Van Der Merwe, R. (2000, October). The unscented Kalman filter for nonlinear estimation. In *Proceedings of the IEEE 2000 Adaptive Systems for Signal Processing, Communications, and Control Symposium (Cat. No. 00EX373)* (pp. 153-158). IEEE.

Westheimer, G. (1954). Mechanism of saccadic eye movements. *AMA Archives of Ophthalmology*, *52*(5), 710-724.

Wilson, M. A., Campbell, M. C., & Simonet, P. I. E. R. R. E. (1992). The Julius F. Neumueller Award in Optics, 1989: change of pupil centration with change of illumination and pupil size. *Optometry and vision science: official publication of the American Academy of Optometry*, *69*(2), 129-136.

Wolpert, D & Ghahramani, Z. (2000). Computational principles of movement neuroscience. *Nature Neuroscience*. **3**: 1212–7.

Wyatt, H. J. (1995). The form of the human pupil. *Vision Research*, *35*(14), 2021-2036.

Yang, Y., Thompson, K., & Burns, S. A. (2002). Pupil location under mesopic, photopic, and pharmacologically dilated conditions. *Investigative Ophthalmology & Visual Science*, *43*(7), 2508-2512.

Yarbus, A. L. (1956). The motion of the eye in the process of changing points of fixation. *Biofizika*,1,7678.